NOVA SCHOOL OF SCIENCE & TECHNOLOGY

DEPARTMENT OF PHYSICS

JOÃO DIOGO FERNANDES ANTUNES FERNANDES

Bachelor Degree in Sciences of Physics Engineering

MULTICHANNEL DENOISING STRATEGIES FOR ULTRAFAST MAGNETIC RESONANCE IMAGING

PHYSICS ENGINEERING

NOVA University Lisbon
November, 2021

NOVA SCHOOL OF SCIENCE & TECHNOLOGY

DEPARTMENT OF PHYSICS

MULTICHANNEL DENOISING STRATEGIES FOR ULTRAFAST MAGNETIC RESONANCE IMAGING

JOÃO DIOGO FERNANDES ANTUNES FERNANDES

Bachelor Degree in Sciences of Physics Engineering

Adviser: Noam Shemesh
Principal Investigator, Champalimaud Center for the Unknown

Co-adviser: Pedro Vieira
Auxiliar Professor, NOVA University Lisbon

Examination Committee:

Chair: André Wemans
Auxiliar Professor, NOVA University Lisbon

Rapporteur: Mário Secca
Associate Professor, NOVA University Lisbon

Adviser: Noam Shemesh
Principal Investigator, Champalimaud Center for the Unknown

PHYSICS ENGINEERING

NOVA University Lisbon
November, 2021

Multichannel Denoising Strategies for Ultrafast Magnetic Resonance Imaging

Acknowledgements

Throughout this work, many are to thank, without whom I wouldn't be able to keep thriving and finalize this work.

First and foremost, I would like to show my gratitude to my adviser Noam Shemesh who, although the global COVID-19 pandemic and limiting restrictions, still gave me the exciting opportunity to work with the Champalimaud Foundation for the Unknown, to learn and excel as a person for the last year while guiding and keeping me motivated in my work and research.

Also a word of appreciation for Professor Pedro Vieira for accepting the challenge to mentor me, while attaining my doubts, concerns and all the support amid last year.

I must likewise thank Professor Isabel Catarino for the help over the past 5 years, guiding me with wisdom, knowledge and advising me whenever it was required.

I would like to thank as well the institution, NOVA School of Science and Technology | FCT NOVA, for providing the necessary means for my education, allowing the environment and socialization to meet so many fantastic people, and to all professors that somehow managed to impact me positively, while to those that have a genuine joy when teaching, please keep going.

I could also not go by without thanking all the amazing people I met over the years, and that without whom I couldn't have finished this degree and wouldn't be standing where I am today. If I were to mention all, this section would be twice as long however, I will point out particularly my class for the past 5 years, "Os 4 Mosqueteiros", Nuno, Moura and Marcelo, Adame, Capela, Special, Audrey, Catarina, as well as to all that particularly in the last month with their goofiness and conversations allowed me to not fall to the dark side.

Finally, I would like to thank all my friends and family for their everlasting support in this journey. Thanks to both my parents and brother for providing me with the care and love needed to get up to this stage and prepare for what the next step of my life will be. To my Mother, the general Dissertation Aesthetics Councilor responsible for both visual and graphic reviewing as well as editing. To my Father, my faithful Editor who, nonetheless his basic knowledge in Med school only allowed him to understand a part

of my thesis, was always present to listen even though he only understood half of what I was saying most of the time, as well as for being my *rubber duck*. To my Brother, for the goofiness, dumbness and relaxing moments and for the comprehension that not all days are the best when writing a 120 pages-long work.

"There will be obstacles.
There will be doubters.
There will be mistakes.
But with hard work, there are no limits."
(Michael Phelps)

Abstract

Magnetic Resonance Imaging (MRI) is becoming an increasingly popular medical imaging method due to its potential for acquiring images from soft tissues noninvasively and with multiple contrast mechanisms. Although it is 50 years old, researchers continue to develop this technology towards better tissue characterization and image quality enhancement. In particular, signal-to-noise (SNR) enhancements have been a focus of research due to the inherently limited SNR in biological systems. Several noise removal methods have been developed, in which the Marchenko-Pastur PCA (MP-PCA) has been gaining increased attention for its effectiveness in noise attenuation in MRI data with at least one redundant dimension (repetitions for functional imaging, diffusion, etc.)

In this study, an Image Reconstruction Technique harnessing the MP-PCA distribution was developed for single and multichannel image denoising. Our results show that, although dependent on the image and dataset conditions, in all performed experiments SNR was successfully increased, suggesting an overall quality boost revealing more details on the acquired images. Additionally, the simple data transformation to other domains, namely k-space, may significantly improve the denoising performance when regridding is required. Finally, we investigated how algorithm parameters, such as denoising window sizes, could show additionally quality increase. Our study thus bodes well for further denoising strategy developments in MRI.

Keywords: MRI, Marchenko-Pastur PCA, Denoising, SNR

Resumo

A Ressonância de Imagem Médica (MRI, do inglês *Magnetic Resonance Imaging*) é cada vez mais um método de imagem médica utilizado na atualidade devido ao seu potencial na aquisição de imagens de tecidos de forma não invasiva e com múltiplos mecanismos de contraste. Apesar de ter sido inventado há 50 anos, os cientistas continuam a desenvolver esta ferramenta de modo a obter melhores resultados na caracterização de diferentes tecidos, bem como na qualidade das suas imagens. As melhorias na relação sinal-ruído (SNR, do inglês *Signal-to-Noise Ratio*), em particular, têm sido alvo de grande interesse devido à sua presença inerente e limitante em sistemas biológicos. Vários métodos de remoção de ruído têm sido desenvolvidos, com particular destaque na distribuição de Marchenko-Pastur PCA (MP-PCA) devido à sua eficácia na atenuação de ruído em dados provenientes de MRI, com pelo menos uma dimensão de redundância (repetições em imagem funcional, difusão, etc.).

No âmbito desta dissertação foi desenvolvida uma Técnica de Reconstrução de Imagem utilizando a Distribuição de MP-PCA para remoção de ruído com aquisição de dados, tanto através de uma como de múltiplas bobinas. Os nossos resultados demonstraram que em todas as experiências, apesar da dependência das condições de aquisição da imagem e do respetivo conjunto de dados, de uma maneira ou de outra, o SNR aumentou, sugerindo um incremento geral da qualidade da imagem, revelando mais detalhes. Adicionalmente, a simples transformação para outros domínios, nomeadamente, do domínio da imagem para o *k-space*, pode melhorar ainda mais o resultado quando *regridding* é necessário. Por fim, investigámos de que forma o tamanho da janela de remoção de ruído influencia o algoritmo, permitindo aumentar a qualidade do sinal. Este estudo permite boas indicações para futuros desenvolvimentos de estratégias de redução de ruído em MRI.

Palavras-chave: MRI, Marchenko-Pastur PCA, Remoção de Ruído, SNR

Contents

List of Figures **xvii**

List of Tables **xxi**

Glossary **xxiii**

Acronyms and Initialisms **xxv**

Symbols **xxvii**

1 Introduction **1**
1.1 History and Motivation 1
1.2 Publications deriving from this work 4

2 Theoretical Concepts **5**
2.1 Introduction 5
2.1.1 Main Magnetic Field 5
2.1.2 Radiofrequency Coils 9
2.1.3 MR Image Formation 11

3 Pulse Sequences **19**
3.1 Types of Sequence 21
3.1.1 Echo Planar Imaging (EPI) 24
3.1.2 Other Pulse Sequences 26

4 Denoising Strategies **27**
4.1 SNR Measurement 27
4.2 Denoising Strategies 29
4.2.1 Principal Component Analysis (PCA) 30
4.2.2 Marchenko-Pastur (MP) Distribution 30

5 Experimental Method **33**

5.1 MRI Protocol 33
5.2 Pipeline 33
5.2.1 K-Space Correction 34
5.2.2 Ghost Correction 34
5.2.3 Coil Combination 35
5.2.4 Marchenko-Pastur (MP) denoising 37
5.2.5 Regridding 38
5.2.6 Phase Unwrapping 41
5.3 MRI Pulse Sequences: Imaging Parameters 42

6 Results **45**
6.1 Experimental Data - Single Channel 45
6.1.1 Comparison between the vendor image and the denoised image 46
6.1.2 Denoising k-space vs image-space 51
6.1.3 Denoising window 56
6.2 Experimental Data - Multichannel 57
6.2.1 Comparison between the vendor image and the denoised image 58
6.2.2 Denoising k-space vs image-space 64
6.2.3 Denoising window 69

7 Discussion **71**
7.1 Single Channel Reconstruction 71
7.1.1 Comparison between the vendor image and the denoised image 71
7.1.2 Denoising k-space vs image-space 72
7.1.3 Denoising window 72
7.2 Multichannel Reconstruction 73
7.2.1 Comparison between the vendor image and the denoised image 73
7.2.2 Denoising k-space vs image-space 73
7.2.3 Denoising window 74
7.3 Limitations 74

8 Conclusion **75**

Bibliography **77**

Annexes

I Abstract Submission **87**

List of Figures

1.1 Illustration about the Medical Image quality variables. 2

2.1 Representation of the protons spin and the Magnetization vector, along with a gyroscope analogy. 6
2.2 Schematics of Parallel state and Anti-Parallel state. 7
2.3 Net Magnetization M of a system. 8
2.4 The Zeeman Effect. 9
2.5 Illustration of the excitation pulses. 10
2.6 Illustration overview of T_2^* and T_2 decay. 11
2.7 Illustration overview of T_1 decay. 12
2.8 Process of Slice Selection. 13
2.9 Different contrast levels obtained from different Pulse Sequences. 14
2.10 Construction of a complex signal and image from their frequencies. 15
2.11 Schematics of how k-space works. 16
2.12 Different Waveforms with the same integral have the same Final Image. . . 17
2.13 Relationship between k-space location and spatial frequency and resulting images. 17

3.1 Schematic representation of TR and TE. 20
3.2 EPI k-space trajectory and corresponding diagram representation. 20
3.3 GRE Sequence and corresponding Signal decay. 21
3.4 SE Sequence and corresponding signal decay. 22
3.5 SE analogy. 22
3.6 Main Difference between EPI and other Pulse Sequences. 24
3.7 Diagram Examples of SE-EPI and GRE-EPI. 25

4.1 Noise distribution in an MRI. 28
4.2 Object noise distribution along k-space, image-space and magnitude. . . . 29
4.3 Covariance matrix eigenvalue spectrum with MP Distribution superimposed. 31

5.1 Pipeline Schematics. 34

5.2 K-space and image before and after ghost correction. 35
5.3 Image before and after coil combination. 36
5.4 Image before and after denoising. 37
5.5 2-D Regridding schematics. 39
5.6 Regridding step (2) close-up - sampling distribution to Cartesian Grid. . . 40
5.7 Image before and after regridding. 40
5.8 Real and phase image before and after unwrapping. 42

6.1 Single Channel (SC): Comparison between Bruker and the Pipeline Reconstruction (PR) image with respective histograms. 46
6.2 SC: Comparison between Bruker and the denoised PR image with respective histograms. 47
6.3 SC: PR image residuals and respective histogram of real, imaginary and magnitude components. 48
6.4 SC: Comparison between Bruker and the regridded PR image with respective histograms. 49
6.5 SC: Real component of the unwrapped and regridded PR image with respective histograms 50
6.6 SC: Image-space denoising with residuals and respective histograms. . . . 51
6.7 SC: Image-space and k-space denoising with respective histograms. 52
6.8 SC: Data before denoising, after Image-space denoising and after k-space denoising with residuals and histograms. 53
6.9 SC: SNR quantitative maps for 3 cases: Original, after Image-space denoising and after k-space denoising. 54
6.10 SC: SNR histogram comparison between 3 cases: Original, after Image-space denoising and after k-space denoising 55
6.11 SC: Plot of the SNR vs denoising Window Size in both parameters SNR_{Map} and SNR_{SV} at 3 different pipeline stages. 56
6.12 Multichannel (MC): SNR vs Denoising Window Size plot at 3 different Denoising scenarios in both parameters SNR_{Map} and SNR_{SV}. 57
6.13 MC: Comparison between Bruker and the PR image with respective histograms. 58
6.14 MC: Comparison between Bruker and the PR image after denoising with respective histograms. 59
6.15 MC: PR image residuals and the respective histogram of magnitude component. 60
6.16 MC: Comparison between Bruker and the real component of the unwrapped PR image with respective histograms. 61
6.17 MC: Bruker and unwrapped PR image with respective histograms with b = 1200 s/mm^2 62
6.18 MC: Image-space denoising with Residuals and respective histograms. . . . 64
6.19 MC: Image-space and k-space denoising with respective histograms. 65

6.20 MC: Data before denoising, after Image-space denoising and after k-space denoising with residuals and histograms. 66
6.21 MC: SNR quantitative maps for the three cases: Original, after Image-space denoising and after k-space denoising. 67
6.22 MC: SNR Histogram comparison between the 3 cases: Original, after Image-space denoising and after k-space denoising. 68
6.23 MC: Plot of the SNR vs denoising Window Size in both parameters SNR_{Map} and SNR_{SV} at 2 different Pipeline stages 69

I.1 Data and residuals. 90
I.2 Quantitative signal to noise calculation for every voxel. 90
I.3 Signal to noise histograms clearly reveal the improvement in k-space denoising over the conventional image based denoising. 91

List of Tables

6.1 SC: Summary Table of the SNR throughout the pipeline. 50
6.2 SC: Summary Table of the Image-space vs k-space Comparison. 55
6.3 MC: Summary Table of the SNR throughout the pipeline for different b values. 63
6.4 MC: Summary Table of the Image-space vs k-space Comparison. 68

Glossary

T_1	Time constant that describes the recovery of the Magnetization longitudinal component M_{xy} back to the same state it was before the excitation 11, 12, 23
T_2	Time constant that describes the decay of the Magnetization transverse component M_z due to accumulated spin phase differences 10, 11, 12, 23, 24, 26
T_2^*	Time constant that describes the decay of the Magnetization transverse component M_z due to accumulated spin phase differences and spatial magnetic field inhomogeneities 11, 23, 24, 25
k-space	Describes MRI data acquisition, as each k-space point contains spatial frequency and phase information about all pixels in the final image 14, 20
Larmor Frequency	The resonant frequency of a spin within a magnetic field 7
Precession	Rotation of an object around its vertical axis 7
Reception	Process of receiving the energy differential ΔE arising from the excess high energy state spins returning to the lower energy state 10
Shimmming	Term originated from Shimming Coils which are EM coils that compensate for inhomegeneities in B_0 21
Spin Isochromats	Collection of nuclear spins processing at the same frequency 10
Voxel	Three dimensional volume element and basic sampling unit of an MRI 23

Acronyms and Initialisms

BOLD Blood-Oxygen-Level-Dependent 2, 3, 23, 25

CSF Cerebrospinal Fluid 23
CT Computed Tomography 1, 3, 38

dMRI diffusion MRI 37

EM Electromagnetic xxiii, 1, 5, 9, 21
EPI Echo Planar Imaging 4, 24, 25, 26, 33, 34, 38, 41, 42, 43, 53, 58, 72

FFT Fast Fourier Transform 13, 15, 38
FID Free Induction Decay 10, 24, 25
fMRI functional Magnetic Resonance Imaging 2, 3, 23, 25, 42, 75

GRE Gradient-Echo 21, 23, 26
GRE-EPI Gradient-Echo EPI 25

MP Marchenko-Pastur 3, 31, 51, 71, 72, 73, 74, 75
MP-PCA Marchenko Pastur-PCA 4, 31, 51, 71, 72, 75, 76
MR Magnetic Resonance 1, 3, 8, 9, 10, 11, 12, 13, 14, 15, 16, 19, 21, 23, 24, 25, 29, 37
MRI Magnetic Resonance Imaging 1, 2, 3, 4, 5, 6, 7, 9, 11, 12, 15, 16, 19, 24, 25, 26, 29, 30, 31, 41

PCA Principal Component Analysis 3, 29, 30, 31, 71
PET Positron Emission Tomography 1, 3
PR Proposed Reconstruction 46, 47, 48, 50, 58, 59, 62, 71, 73

RF Radiofrequency 3, 5, 9, 10, 13, 14, 19, 20, 21, 23, 24, 26
RMT Random Matrix Theory 30, 31, 72
RO Readout 14, 24, 34
ROI Region Of Interest 27, 28, 58, 61

SE Spin-Echo 21, 22, 23, 26
SE-EPI Spin-Echo EPI 25
SNR Signal-to-Noise Ratio 3, 16, 27, 28, 30, 33, 36, 41, 43, 45, 46, 47, 51, 53, 54, 55, 56, 57, 59, 60, 64, 65, 67, 68, 69, 71, 73, 74, 75
SVD Singular Value Decomposition 30, 31, 34

TE Echo Time 19, 21, 26, 42
TR Repetition Time 19, 21, 42

Symbols

B	Magnetic Field 21, 22
B_0	Static Magnetic Field xxiii, 7, 8, 11, 21, 25
$CG_{\mathrm{W}\times\mathrm{W}}$	Cartesian Grid with Size $W \times W$ 38, 40
K_{KB}	Kaiser-Bessel Window 38, 40
M	Net Magnetization 7, 8, 9, 10
M_{xy}	Longitudinal Magnetization xxiii, 10, 19
M_z	Transverse Magnetization xxiii, 10, 11, 21
ϕ	Signal Phase 41
$\lvert Z \rvert$	Signal Magnitude 27, 41

1

Introduction

1.1 History and Motivation

For many years, the human brain has been the most intriguing and unexplored part of the human body. In the eighteen hundreds, scientists could not systematically study how impactful brain damage was or how brain stimulation could work, as invasive procedures were required. This part of the human body had a lot of misconceptions, inconsistencies and inexplicable mysteries, some of which only began to be unravelled when a non-invasive technique was invented in 1973: the Magnetic Resonance Imaging (MRI). It was finally possible to observe and record images of the active brain in both clinical and research environments, becoming an extremely important technique in cognitive neuroscience with several advantages: no usage of Computed Tomography (CT) X-rays and its deleterious effects, no radioactive injections used in Positron Emission Tomography (PET), faster acquisition rates and because of its non-invasiveness, no harm is done to the patient, among others [1–3].

As the name suggests, MRI uses strong magnetic fields to create biological tissue images, using Pulse Sequences - a series of changes in magnetic gradients and oscillating Electromagnetic (EM) fields. Due to the abundance of water molecules in living beings, MRI scanners have their EM fields tuned to the resonance frequency of hydrogen nuclei, meaning they will be excited in the process and the energy subsequently released can give information about the density and types of molecules present, measuring the Magnetic Resonance (MR) signal [2]. Information about the distribution of molecules can then be acquired, allowing a correct mapping of the human body's internal anatomy or the analysed subject, where high signal areas mean a larger specific molecule concentration. Determined by the type of pulse sequence used, different tissue properties and types can be detected, like differentiating torn from intact ligaments and distinguishing grey and

white matter, respectively. This way, one may see the benefit of using this technique, however it can have limitations as it can't reveal immediate short-term physiological changes correlated with which active functioning part of the brain, yet they were mitigated by the emergence of functional Magnetic Resonance Imaging (fMRI) - fast and precise measurements of blood flow changes in result of brain activity [4] - which allowed Blood-Oxygen-Level-Dependent (BOLD) imaging, conceding knowledge on the brain's organization in the process [2, 3].

As a result, and after several decades of development, MRI has become a crucial medical imaging device that contributed to revolutionize our understanding of the brain. Neuroscientists were focusing on studying individual neurons, having difficulties in studying the relationships between population-level neural activity and behaviors, so MRI allowed observation of not only the contours and structure of the brain but also how real-time connection between thought and behavior worked. Initial efforts focused on brain function localization and how different areas linked together, and grounds were found that mental operations occurred over networks of related neuron groups [5].

According to Sprawls [6], when talking about image processing techniques, the quality of medical images can be determined by the imaging parameters selected by their operator, the characteristics of the equipment, the method itself and can be dependent on a combination of factors such as contrast, noise, blur, distortion and artefacts - Fig. 1.1. Image contrast can be defined as the intensity difference between distinct signal intensities being measured by an imaging system [3, p. 10]. If the technique used is sensitive to small changes, the resulting image will have good contrast, allowing distinction between objects with slight differences.

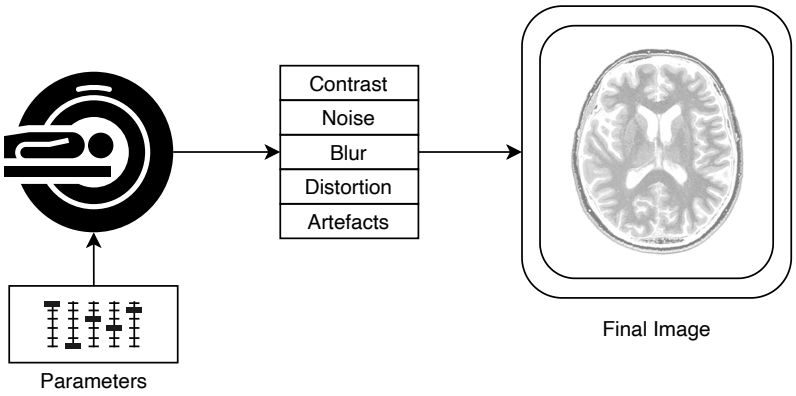

Figure 1.1: Illustration about the Medical Image quality variables. Adapted from [6, 7].

Furthermore, being an imaging method it won't be perfect: image noise will always endure. In other words, several sources from data acquisition and transmission like variation in the measured signal consequence of patient movement, small variations of magnetic field susceptibilities, stochastic variation [3], etc., up to mathematical computation, can easily corrupt images, making them blurred and unsharpened, reducing overall

quality [8].

This way, it becomes vital to minimize noise at every source: from possible hardware malfunctions and variations, up to data processing and efficiently applying Denoising methods to acquired data, enhancing the quality of the final image [8].

One important parameter to determine how good an image can be is the Signal-to-Noise Ratio (SNR), which can be defined as the relative strength of a signal compared with other sources of variability in the data [3, p. 245]. This way, depending on the type of pulse sequence used, grey and white matter or fluid and different tissue will provide distinct contrast levels, thus different signal levels as their MRI will report different proton densities through weighted relaxation parameters. Improvements on SNR can be achieved by increasing the signal's amplitude or decreasing associated noise, and can be pretty significant when dealing with signals of small variation when compared with the total intensity of MR signal like those obtained in BOLD measurements [3]. Like mentioned before, there can be several types of Image Noise like blur, distortion and artefacts, and their primary sources are electronic interferences in receiver circuits, Radiofrequency (RF) emissions due to patient's thermal motion and measurements in the MRI scanners functioning like coils, electronic circuits, etc. [8].

Thus, diverse denoising strategies have been described in recent literature which involve several techniques with varying results.

Besides cutting-edge technological advances leading to improvements, fMRI is still affected by many motion artefacts, so Burgess et al. [9] used several denoising strategies: fMRI of the brain independent component analysis-based X-noiseifier, motion regression and censoring high motion time points, which induced some pros and cons in MRI noise removal, yet for more satisfactory results extra investigation is necessary.

Ananad and Sahambi [10] developed a wavelet-based bilateral filtering scheme for different noise coefficient reduction, which effectively preserves the border-image details. The method has been specifically adapted for Rician noise and has been used as a promising feature preserving method.

Kaur et al. [11] used Machine learning strategies to apply image denoising on several medical applications including MRI. Machine learning approaches with the best accuracy for medical diagnosis were identified, which included using several filtering techniques. In most applications, the machine learning performance is better than the conventional image denoising techniques, although it may need to be enhanced via different algorithms and more complete datasets.

The possibility of branching to other medical imaging techniques such as X-ray, CT, PET, Ultrasound, etc. makes denoising an extremely interesting subject to other fields of science, so there are endless articles and possibilities in how to effectively remove noise, and reach the target as no method is perfect.

This dissertation aims at developing an Image Reconstruction Technique with denoising strategies via Principal Component Analysis (PCA) algorithms, more specifically, the Marchenko-Pastur (MP) Distribution. Therefore, the dissertation objectives will be

to gain expertise in MRI, understanding how Champalimaud's MRI scanner works and processes data typically acquired in preclinical settings, to develop denoising strategies and finding how efficient and reliable the MP-PCA denoising implementation method is. Finally, Echo Planar Imaging (EPI) Single and Multichannel Reconstruction will be accomplished as well as how corresponding denoising may be addressed.

1.2 Publications deriving from this work

The work developed in this dissertation allowed an Abstract submission - which was rejected - for the annual meeting of the International Society for Magnetic Resonance in Medicine (ISMRM) titled "Marchenko-Pastur PCA denoising performance is enhanced in the k-space domain" and authored by Joao Diogo Fernandes, Andrada Ianus, Jonas L. Olesen, Rafael Neto Henriques, Sune N. Jespersen, Noam Shemesh.

The abstract that was submitted can be seen in Annex I with the respective documentation.

2

Theoretical Concepts

2.1 Introduction

Present-day MRI scanners can be separated in 3 main components: the **strong magnetic field** generated by a series of EM coils to which the patient is exposed, the resonance frequency energy delivered by **RF coils** to the targeted atomic nuclei, and in the end an **image is created** due to the magnetic field's strength alterations over space by magnetic gradient coil switching [12]. There are more components than those mentioned, however as they have an indirect impact on the system's overall performance and in correcting inconsistencies, will not be described here.

2.1.1 Main Magnetic Field

In 1820, Danish physicist Hans Ørsted demonstrated that a wire carrying current could create a magnetic field and that its strength is proportional to the current's intensity, meaning it could easily be wielded, a discovery that was the MRI basic principle many decades later [3]. In the early days, scanners mainly used ferromagnetic shield structures as the magnetic source [13], which added a lot of unnecessary weight and size to the system and generated weak magnetic fields restricted by their composition. Also, because it was extremely difficult to ensure the homogeneity of the main magnetic field over space, scientists had to further develop magnet technology to make the MRI less bulky and more practical machines [12].

In order to obtain a suitable **magnetic field** for MRI usage, two criteria can be defined: field homogeneity and field strength [3]. Concerning the former, generating a uniform and constant magnetic field allows images from the scanner to depend neither on the characteristics of the machine in use nor how the subject is placed in the field - if not homogeneous, the measured signals of the same tissue type can change [14]. The second criteria, because very high magnetic fields are required and electromagnets have a huge electrical power expense, superconducting magnets cooled to temperatures near absolute zero (~4K) are used in MRI scanners, whose properties in this situation allow very high magnetic fields with very little energy expenditure, as electric resistance ceases to exist.

This way, an intense, stable and lasting electric current can be obtained with no electrical consumption, with the only cost being cryogenic temperature maintenance [3].

The fundamental MRI property that allows it to work is the **spin**, inherent to sub-atomic particles like protons, electrons and neutrons. Only atoms with an odd number of neutrons or protons will have a net nuclear spin that can be studied under magnetic resonance, as with an even amount of spins will cancel each other, as they are in opposite directions [3, 15].

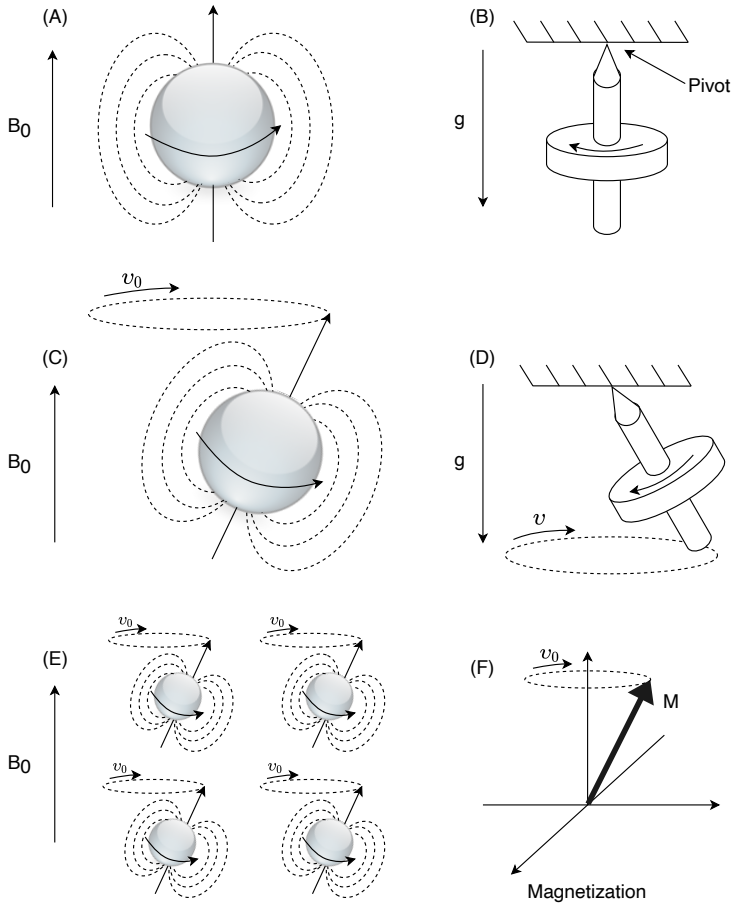

Figure 2.1: Representation of the spin and charge of a proton in (A), causes it to have a magnetic moment that precesses at a frequency v_0 and have a tendency to align with an external B_0 in (C). If in a group - (E) - they will all precess in sync and their net sum forms the Magnetization M vector - (F). Similarly, an analogy can be made with a hanging gyroscope from a vertical pivot - (B) - where the magnetic field is the earth's gravitational field and if tipped off equilibrium will precess around it - (D). Adapted from [16].

Considering a more *classical perspective*, one may consider a proton as a spinning sphere with both charge and mass. The associated spin can be seen as a rotation of the nucleus around a random axis. In combination with its charge, the proton can be seen as a small bar magnet - magnetic moment - with an associated angular momentum - defined by Britannica [17] as rotating objects that will continue their rotation unless disturbed. If

placed in a magnetic field B_0, it will tend to align with that field, as can be seen in Fig. 2.1 (A). An analogy can be scoped with a hanging gyroscope - Fig. 2.1 (B), if left untouched, it would naturally align with Earth's gravitational field. After being disturbed - Fig. 2.1 (D) - the gyroscope will start a phenomenon called precession - rotation of an object around its vertical axis [18] with a precession frequency of v [16].

Likewise, if the proton's spin was shifted from its point of equilibrium, it would start to precess around the direction of the applied magnetic field B_0 - as displayed by Fig. 2.1 (C) - with a precession rate v_0 that can also be called Larmor Frequency, a value which is equal among the same type of nuclei and is proportional to the applied magnetic field [3]. If several protons are placed together - Fig. 2.1 (E) - the sum of all magnetic moments from spins of different orientations can be seen as the net Magnetization vector M - Fig. 2.1 (F) - which in the absence of magnetic field will be infinitesimally small [16].

Thinking analogously in the context of MRI, the hydrogen atoms of the subject will precess around random directions, and after applying an external magnetic field B_0, they will all reach the minimal energy state: the same gyroscopic motion around a parallel axis [16] - Fig. 2.1 (C).

There are two equilibrium states for precessing protons: one **parallel** to the magnetic field, with a lower energy level, and another **antiparallel** state, with higher energy - Fig. 2.2.

Because the first state is slightly more stable, it will be slightly more populated in the equilibrium sate, with the exact relationship dependent on the temperature and magnetic field strength. If for example, one of those parameters increases, some protons will gain energy and jump to the antiparallel state, decreasing its population, but never overturning the small difference and vice-versa [3].

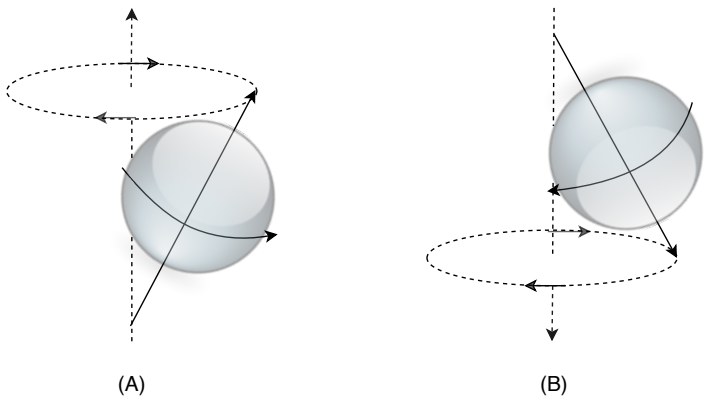

Figure 2.2: Schematics of the Parallel state in (A) and Anti-Parallel state in (B). Adapted from [3].

For an easier interpretation, as stated before, the M vector can be defined as the net sum of all magnetic moments of each hydrogen in the sample, as can be seen in Fig.

2.1 (F), which will precess around B_0, as MR techniques measure M and not individual atomic magnetization. The net magnetization M can be seen as a vector with two components: a **longitudinal component** that may be parallel or antiparallel, and a **transverse component** that is perpendicular to the magnetic field B_0 [19] - Fig. 2.3. Normally, the transverse components will tend to cancel each other, leaving no net magnetization perpendicular to the main magnetic field, suggesting the real contributor to M is the longitudinal component, whose magnitude is proportional to the difference between parallel and antiparallel states [3].

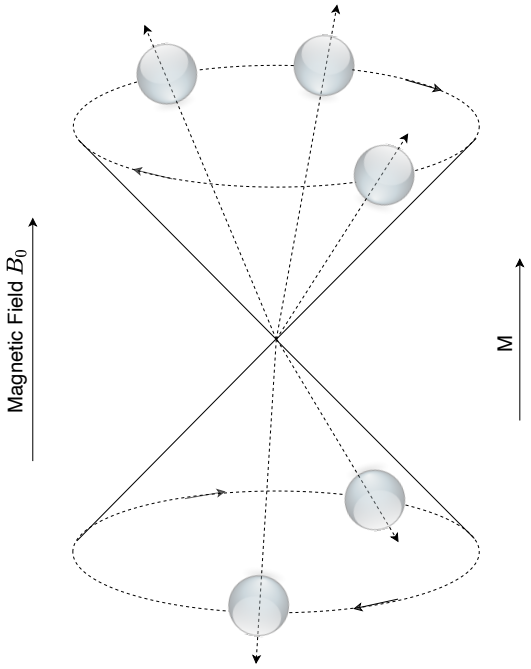

Figure 2.3: Net Magnetization M of a system. Adapted from [3].

Theoretically, there are two ways to increase magnetization M: lowering the system temperature or increasing the magnetic field's strength. The first not only is unattainable with live biological samples but also a significant increase in M would need a drop in temperature of many orders of magnitude. That is why the easier and most attainable is the second, as according to the Zeeman Effect, placing a system in a magnetic field will induce splitting to two or more components with different frequencies [20]. The separation will be proportional to the magnetic field's strength - Fig. 2.4 - resulting in an increased M and energy variation ΔE [3].

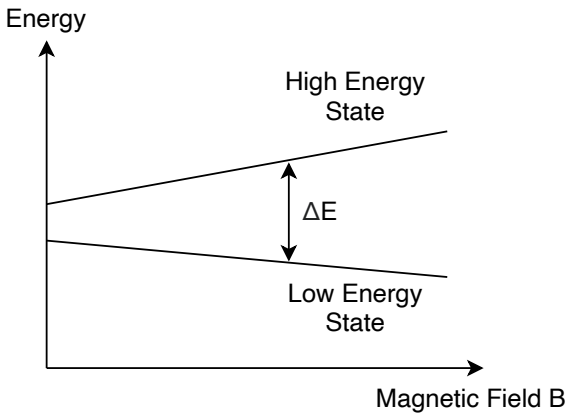

Figure 2.4: The Zeeman Effect. The increase in magnetic strength will make the energy difference (ΔE) bigger. Adapted from [3].

2.1.2 Radiofrequency Coils

The net magnetization M of spins is an important factor in MRI functioning, however its measurement has a peculiarity. The same way you can only know the weight of an object by perturbing its equilibrium state, you can not directly measure the magnetization M unless an environmental disturbance is induced [3].

This disturbance can be generated and detected by **RF coils** that emit EM fields at the resonant frequencies ω of the atomic nuclei within the static magnetic field, originating the MR signal.

The resonant frequency ω is given by $\omega = \gamma \times B_0$ where γ is known as the gyromagnetic ratio, dependent on the charge and mass of the proton. Considering its invariability, the scaling factor γ will thus be constant for the same type of nucleus and independent of the magnetic field strength or any other varying factor [3].

Although the coils are only typically turned on for a small fraction of time, they will also have the same criteria as the static field: space uniformity and sensitivity - the relative strength of the emitted/detected signal [3, 8]. After applying the magnetic field, the atomic nuclei magnetic moments become aligned, and the RF coil will generate an EM impulse with the resonant Larmor Frequency, resulting in the excitation process where spins change from low to high energy states [21].

At this point, two excitation pulses can be distinguished:

- **90°/ $\frac{\pi}{2}$ excitation pulse** - the longer the RF coil is turned on, the more spins will jump from low to high energy state, eventually reaching a point of equal number of spins in either state, which means the net magnetization M, originally only with a longitudinal component, will all be shifted to the transverse plane - Fig. 2.5 (A).

- **180°/ π excitation pulse** - if EM waves emission continues past the aforementioned point, spins will keep accumulating in the high energy state and eventually the

proportion will be the exact opposite it started with, i.e. the magnetization will be symmetric to the starting point, and may be used to increase contrast in some MR image types - Fig. 2.5 (B).

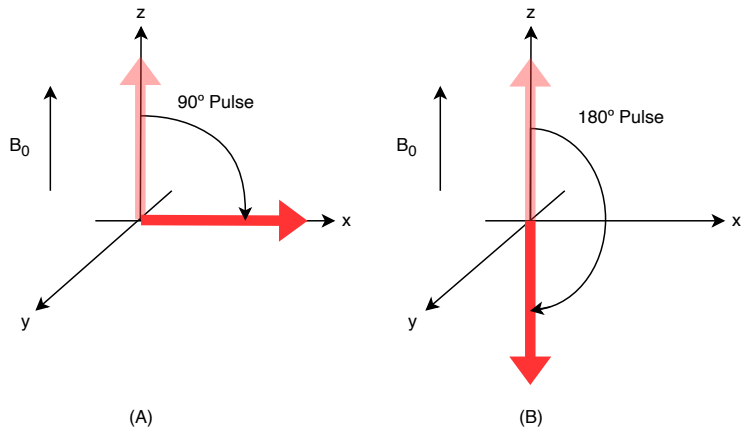

Figure 2.5: Illustration of the excitation pulses. (A) 90° Pulse. (B) 180° Pulse. Adapted from [22].

After the RF coil is turned off, the excitation process stops and equilibrium has to be replenished: the excess high energy state spins will return to the lower energy state, emitting the energy differential ΔE corresponding to the Larmor Frequency, arising a process known as Reception [3]. The changing transverse magnetization M_z causes magnetic flux density variations that can be detected by another RF coil tuned to the same Larmor Frequency and, by Faraday's Law, an oscillating electric current is originated, which reciprocally corresponds to the MR signal. The latter is proportional to both magnetic moment and flux variation speed, meaning that only time-varying transversal magnetization can be detected [16, 22].

All of the above physical principles, and thus the MR phenomena, can be described by the Bloch Equation - [3, eq. (3.47)] - a single equation named after physicist Felix Bloch that describes how the net magnetization M of a spin system behaves in the presence of a magnetic field that varies over time.

Respectively, during signal reception, M_{xy} and M_z have to go through two processes to return to the original position: Transverse and Longitudinal Relaxation. Both are added to create the net Magntization vector M [22].

In **Transverse Relaxation** - Fig. 2.6 - the net magnetization M expresses the sum of the individual spins while its amplitude is highly dependent on their coherence. After M being tipped over, all spins, referenced as *Spin Isochromats*[1] start with the same frequency and phase. However over time, these will start to lose coherence, implicating spins will precess at different rates, leading to an exponential decay of the MR signal characterized by time constant T_2, also known as Free Induction Decay (FID) [16, 20, 22].

[1] defined by Cohen [23] as a collection of nuclear spins processing at the same frequency

Furthermore, spin-spin interactions[2] and spatial magnetic inhomogeneities, which can be induced by variations like tissue magnetic susceptibility among others, translate to spins experiencing different magnetic fields over time, causing some to precess more rapidly and, combined with the T_2 constant, can cause the signal to decay in the X-Y plane with T_2^* [3, 20].

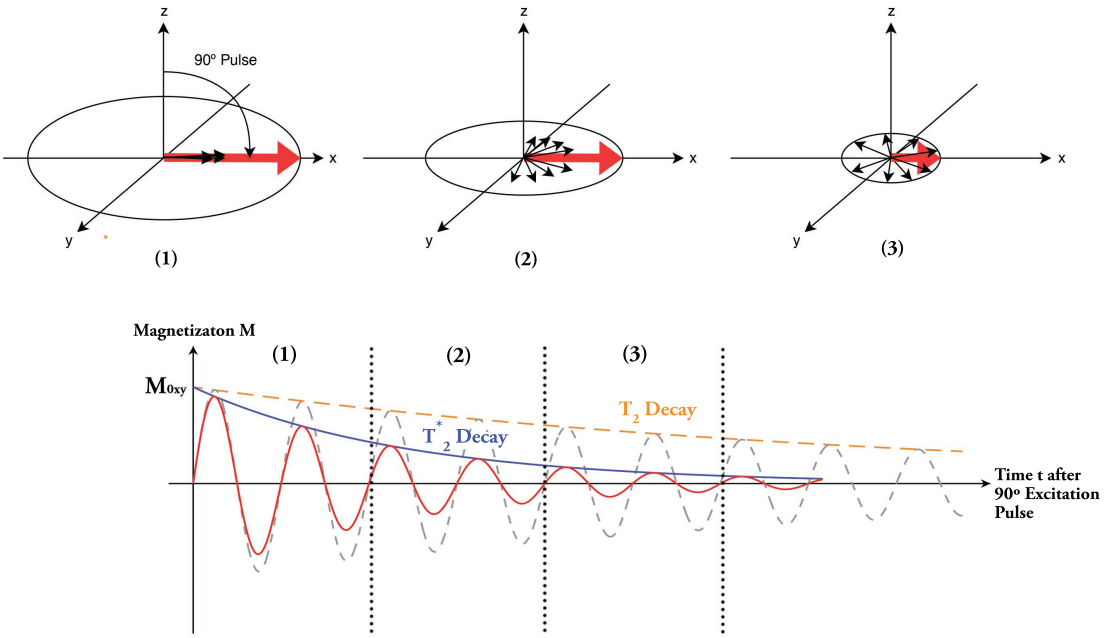

Figure 2.6: Illustration overview of T_2^* and T_2 decay and the corresponding states along time. Full red and dotted gray lines correspond to how the signal decays overtime in T_2^* and T_2, respectively. Full blue and dotted orange lines correspond to how overall T_2^* and T_2 signal relaxation decays overtime, respectively. Adapted from [3, 24].

In **Longitudinal Relaxation** or Spin-Spin Relaxation - Fig. 2.7 - the spin system loses energy, and longitudinal component of Magnetization, M_z, slowly recovers back to the same state it was before the excitation and is characterized by a time constant T_1 [16, 22].

All of these constants heavily depend on B_0 strength and homogeneity, as well as the material type and while all are measured in milliseconds, T_1 is larger than T_2, and T_2 is greater than T_2^*, nonetheless all are important in how the MR signal amplitude and the intensity of the image are recovered. Each constant can therefore provide both different information and contrast, that can vary according to the different tissues' response [3, 16].

2.1.3 MR Image Formation

After obtaining the MR signal there is still loads of data to be analysed in order to obtain an **image**. Like every digital medical imaging method, the challenge of MRI is to recover

[2] interaction between two spin states which will lead to a change and consequent energy variation [3]

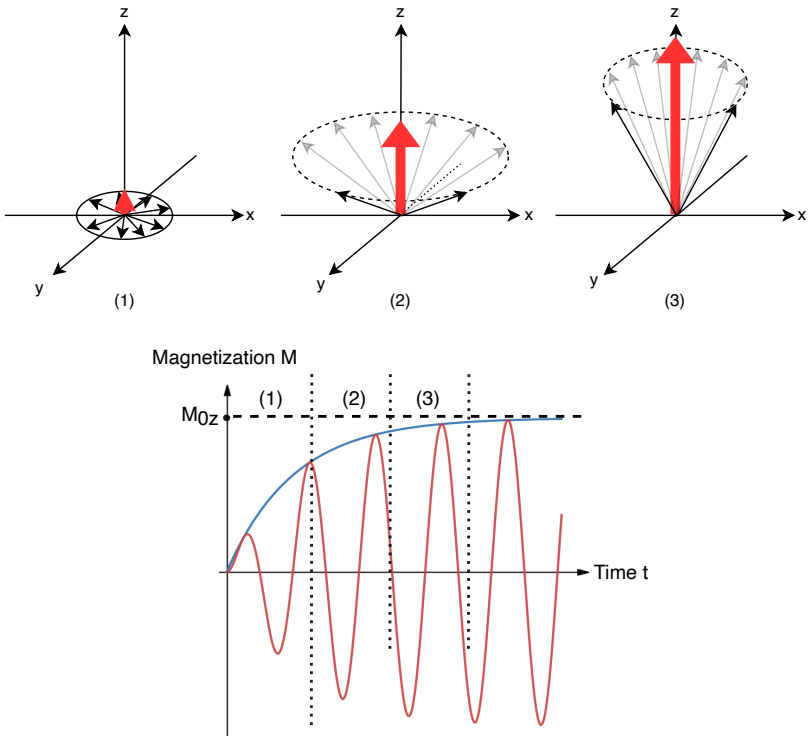

Figure 2.7: Illustration overview of T_1 decay and its corresponding states along time. Full blue line corresponds to how the signal decays overtime, and full red line corresponds to how overall T_1 signal relaxation rises overtime. Adapted from [3].

from an array of pixels the signal intensity corresponding to different points throughout the anatomy [16]. As mentioned before, the MRI image is not a common picture of the object, rather corresponds to a spatial distribution map of a sample property: spin density, spin mobility or the T_1 or T_2 relaxation times of targeted tissues [3].

Given that the MR signal originates from the entire object, instead of a single point within it like other medical devices [16], a form of encoding scheme will be necessary to obtain spatial information in each dimension, which can be achieved with a gradient coil for each axis.

The introduction of a gradient coil - providing a spatially varying magnetic field [12] - allowed atomic nuclei to precess in distinct spatial locations at different rates, as precession frequency is proportional to the applied magnetic field. In comparison to the applied magnetic field, these gradients produce very subtle perturbations to the overall field however are enough to deliver spatial information [16].

Slice Selection

The first step in **image formation** is selecting, one at a time, the two-dimensional human body slice - its location and thickness - via selective excitation. This requires that only the spins on the selected slice are excited, and none of the surrounding [3]. The encoded

image can be obtained by applying a magnetic field gradient G_z in the Z-axis[3], meaning the Magnetization will have a Larmor Frequency location dependency. This way, to select the shaded section (Fig. 2.8 A), an RF excitation pulse with the corresponding frequency bandwidth of f_1 to f_2 is emitted (Fig. 2.8 B-C), and because the whole object has a different magnetic field value, it ensures only the targeted slice is on resonance with the excitation pulse. Sequentially, if the pulse is symmetric, which is almost always the case, then there will be an opposing half gradient, a G_z refocusing gradient, which will refocus the spins in plane.

After turning the RF coil off, the MR signal is only emitted by the selected slice spins (Fig. 2.8 D), which also implies width and slice location can be adjusted by modifying the gradient coil strength and frequency range [3, 16]. In order to obtain frequency distribution of the RF pulse corresponding to the selected slice, a Fast Fourier Transform (FFT) of the pulses' time profile must be applied [15, 22].

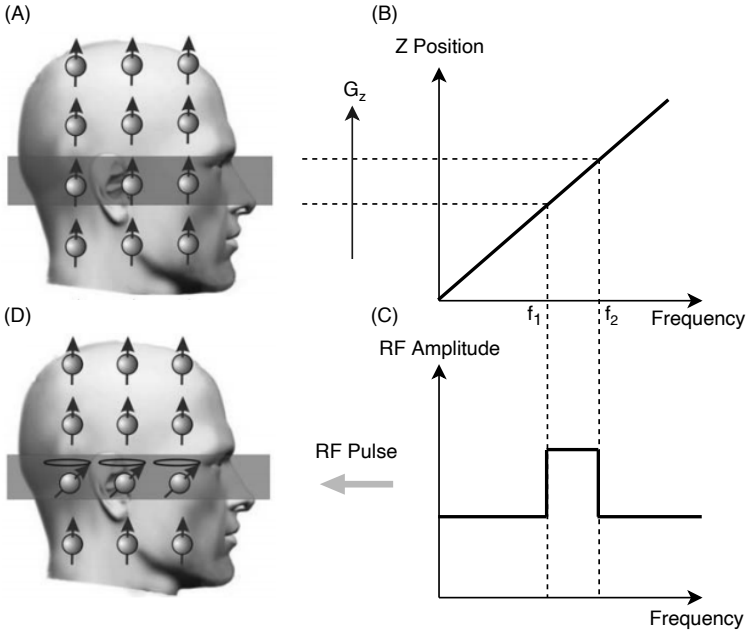

Figure 2.8: Process of **Slice Selection**. To select the shaded slice (A), a gradient G_z is applied so that its position corresponds to a frequency bandwidth from f_1 to f_2 - (B). Right after, an RF excitation pulse with that bandwidth is utilized - (C) to excite just the selected slice (D) and not the surroundings. Adapted from [16].

Following slice selection, as described in section 2.1.2, relaxation will start immediately after the excitation pulse and, because the process is extremely fast, application of other gradients must follow to provide spin distribution information inside that slice [3].

[3]In MRI, the Z-direction is generally along the magnetic field, which in turn is along the lying body.

Frequency and Phase Encoding

The second step in **Image formation**, after slice selection, will be acquiring spatial information on the slices X- and Y-position. Because the sole information on Z-axis is insufficient to form an image, usage of gradient coils in sequence will be necessary, which can be done in two Encoding steps: Frequency and Phase [3].

For the **Frequency** or **Readout (RO)-Encoding** step, by convention a gradient G_x along the X-direction[4] will make the precession frequency depend on the protons' position, allowing their distinction as they have different X-coordinates/frequencies. Sequentially, as spins are already tagged in the X-position, for the **Phase Encoding** step, the Gradient G_y will further distinguish the signal as spins vary in their phase, meaning distinct Y-coordinates have different phases [3].

Consequently, recorded MR signal differentiation depends on the strength and direction of the magnetic gradient's sequence used, meaning the characteristics of the imaged object can be determined. When different RF pulses are added to the pattern, further cementing distinction of obtained characteristics, a Pulse Sequence is created [3, 16] - images from different Pulse Sequences are shown in Fig.2.9 .

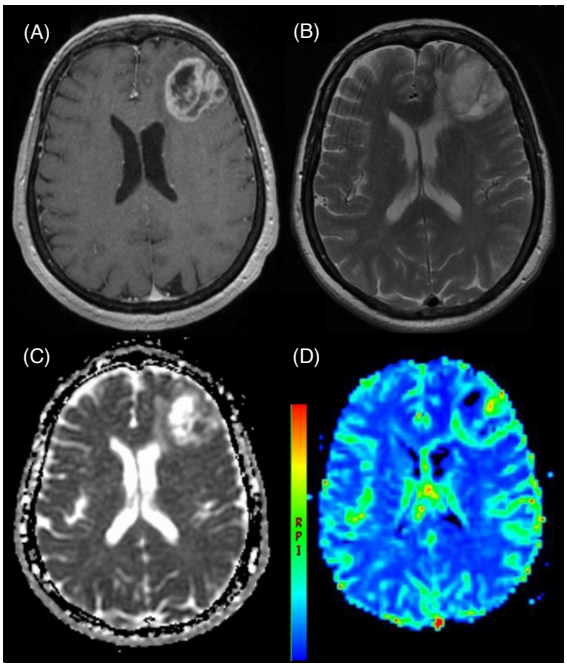

Figure 2.9: Different contrast levels obtained from different Pulse Sequences. (A) - T_1 Contrast MRI; (B) - T_2 Contrast MRI; (C) - T_1 Diffusion MRI; (D) - T_1 Perfusion MRI. Adapted from [25].

Due to the complex visualization of spin phase, magnetization, gradient strength and their subsequent relation with MR signal and the imaged object, a k-space notation was

[4]Important to note Gradient fields only change the strength of Magnetic Field on the correspondent axis, never its direction.

adopted to make it a more understandable concept. It describes MRI data acquisition, as each k-space point contains spatial frequency and phase information about all pixels in the final image [3, 20], and is commonly displayed on a grid with principal axes k_x and k_y - Fig. 2.11.

Like any time-varying complex signal can be decomposed into a series of simpler frequencies [26] - Fig. 2.10 (A), an image can be constructed from simpler components that constitute the frequency map - Fig. 2.10 (B). Using the FFT to decode the k-space representation of the MR signal into the magnetization at each point, the final spatially informative image is obtained [27].

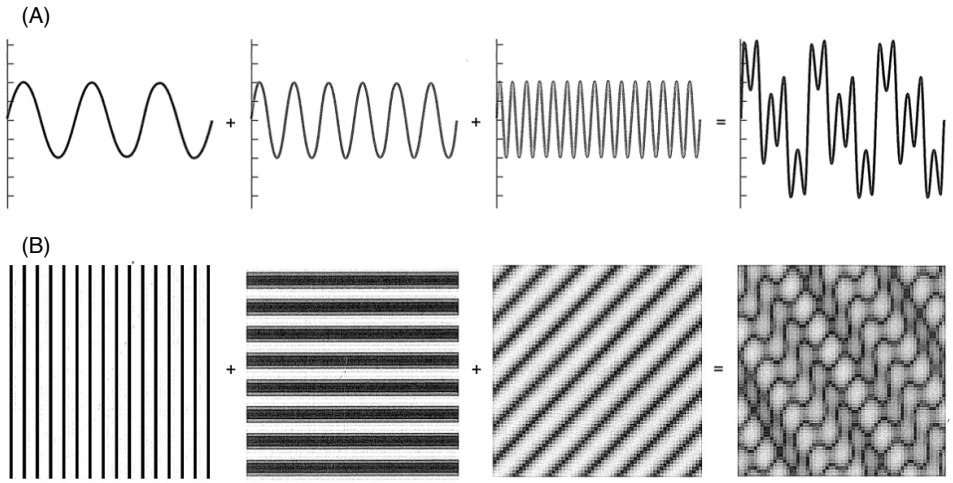

Figure 2.10: Shown in (A), construction of a complex signal, at the right, from 3 sine waves with different frequencies, at the left. Shown in (B), construction of a complex image, at the right, from 3 gratings whose patterns are determined by their spatial frequencies (distance between stripes). Adapted from [3].

More generally, for the image to be obtained, the **k-space filling** is achieved by manipulating the aforementioned phase and frequency-encoding gradients parameters, so the sampling path taken in k-space can be controlled during MR signal acquisition.

As can be seen in Fig. 2.11, after the slice selection step - if frequency encoding G_x is enabled, frequency differentiation will occur, which translates to a movement in k-space along X-direction of the data acquisition location, as can be observed in Fig. 2.11 - (1) as a green arrow. Right after, phase encoding G_y is turned on, changing the amount of phase, represented by red arrow movement in k_y - Fig. 2.11 - (2). The sequence is ended by data acquisition along the whole k_x line, as the process is repeated line by line until all "n" lines are scanned [3, 22].

It is important to note that this is an analog to digital conversion process, i.e. k-space sampling occurs in a discrete set of data points, as each line in k_y represents a different amplitude of G_y and k_x is sampled with a specific interval, which are translated to pixels by an FFT [16]. This way the acquired signal is only dependent on the gradient's waveform

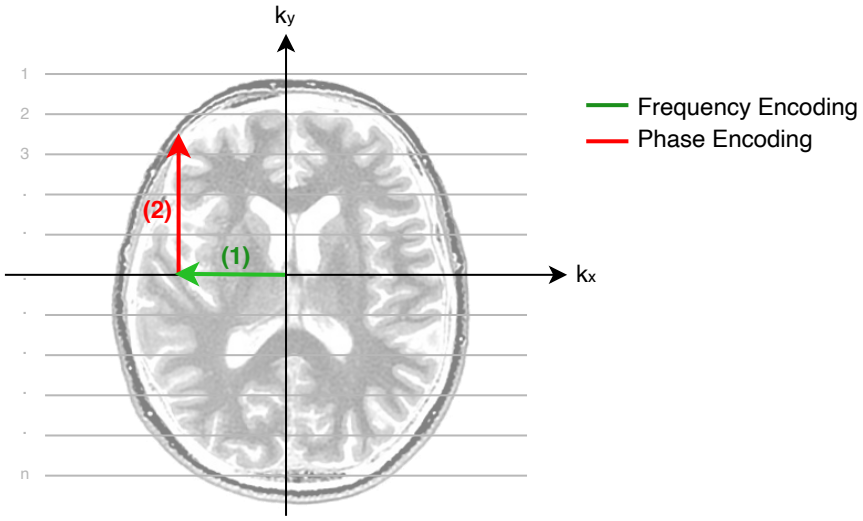

Figure 2.11: Schematics of the k-space with a 2-dimensional Pulse Sequence example. After the **Slice Selection** step, G_x gradient (**Frequency Encoding**) is used and a movement in k-space along X-direction of the data acquisition location is performed - green arrow (1). Finally gradient G_y (**Phase Encoding**) is enabled - red arrow movement (2) - followed by data acquisition. The process is repeated for every k_y line until all "n" lines are scanned. Adapted from [3, 7].

integral, meaning a larger amplitude but shorter duration will have a higher rate of k-space traversing than a lower amplitude with larger duration, but will have equivalent images - Fig. 2.12 [23].

As mentioned before, one other way to analyse k-space can also be with the object's spatial frequency in the image space which can be defined as how often a pattern occurs. The periphery portion of this image, corresponding to the high spatial frequency data, is commonly known as the image details and spatial resolution - Fig. 2.13 (A). On the contrary, information like image contrast and SNR are encoded on the center, corresponding to the low spatial frequency data - Fig. 2.13 (C). This becomes of extreme importance when small lesions are the focus of the investigation, as the objective of acquiring maximum contrast that is useful in clinical studies, while maintaining a minimal loss of information and the least number of artefacts can only be achieved by the correct mapping of the MR signal's varying magnetization during data collection [23]. Only by combining the two, a useful image is obtained, as their separation will provide an image either lacking spatial information or low signal and overall brightness differences.

This way it becomes of extreme importance to understand how MRI, k-space and image formation relate and can be combined to create pulse sequences for different tissues to be analysed and new experiments in specific conditions can be idealized.

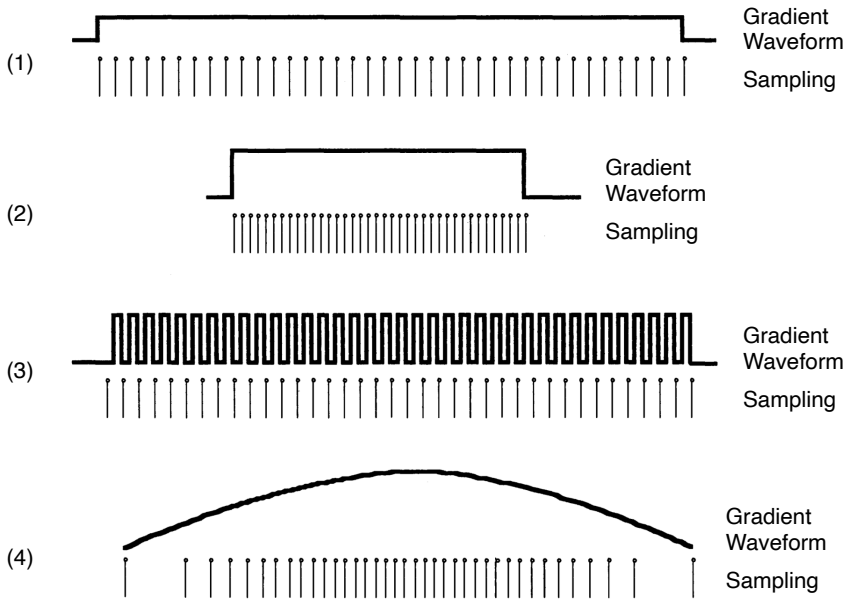

Figure 2.12: The MR is sampled digitally in the presence of magnetic field gradients - the signal is sampled discretely, rather than continuously, i.e. the spatial encoding depends only on the integral of the gradient waveform. The 4 spatial encoding schemes above all represent the same image, even though their waveforms are different, their areas are the same. Retrieved from [23]

.

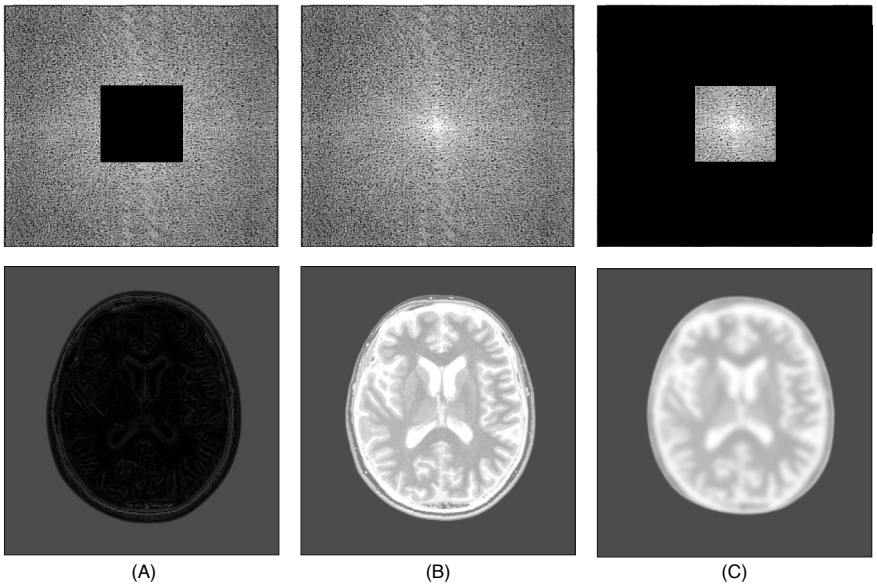

Figure 2.13: Relationship between k-space location and spatial frequency. In (B), it is possible to see raw k-space data and the resulting image. In (A), if the center of k-space is zeroed, only the **high spatial frequency** remains with its corresponding image, where it is possible to see the image details and spatial resolution. In (C), if the periphery of k-space is zeroed, only the **low spatial frequency** remains with its corresponding image, where it is possible to see the image contrast features. Adapted from [7, 23]

.

3

Pulse Sequences

After understanding how MRI obtains and processes data to obtain the final observable image, we can then step into how each pulse sequence works to produce different image types. As previously mentioned, image contrast is the intensity difference between distinct signal levels, which can be achieved in numerous ways - corresponding to different pulse sequences - each providing a unique image with different information for each tissue.

There are two main approaches used to create contrast: **static** and **motion contrast**. The **first** is mainly used to get images that determine brain anatomy and can be sensitive to relaxation time, chemical concentration or a specific molecular type; the **second** is used to obtain information about dynamic characteristics of protons in the brain, like blood flow, water diffusion or capillary irrigation. In addition, contrast can be further distinguished into endogenous or exogenous contrast, depending on whether it's derived from intrinsic biological tissue properties or the presence of external substances in the body, respectively. Focusing more on endogenous static contrast due to their potential in acquiring more clinical useful imaging, there are several varieties of MR contrast like Proton Density, T_1 and T_2 contrast [3].

Tissues differences in the latter parameters create different contrasts on images as they produce varying levels of sensitivity to different relaxation times. The two key factors that influence when the images should be collected are Repetition Time (TR) and Echo Time (TE). TR is the time interval between successive RF excitation pulses. Regularly, because time decays are exponential, these excitations occur in time intervals that don't allow full recovery of M_{xy}, there is a point where the gain in contrast doesn't surpass the wait time. The TE is the time interval between the application of RF pulse and the peak of the echo detected at the k-space centre, where the signal is strongest. Both concepts can be observed in Fig. 3.1

Remembering how an MR image is obtained, a pulse sequence can also be described both as the gradient and RF pulses waveform applied in MR image acquisition. One other way of referring to a pulse sequence is via a diagram - Fig. 3.2 (B). It represents the series of instructions sent to the RF generator and gradient amplifiers, consisting in several

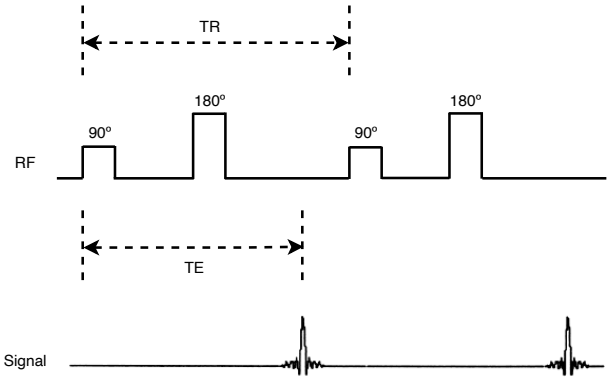

Figure 3.1: Schematic representation of TR and TE. Adapted from [28]

lines for each parameter: one for the RF pulse, z- (G_{slice}), y- (G_{phase}) and x-axis ($G_{readout}$) gradients, which will result in its corresponding k-space trajectory - Fig. 3.2 - (A) [29].

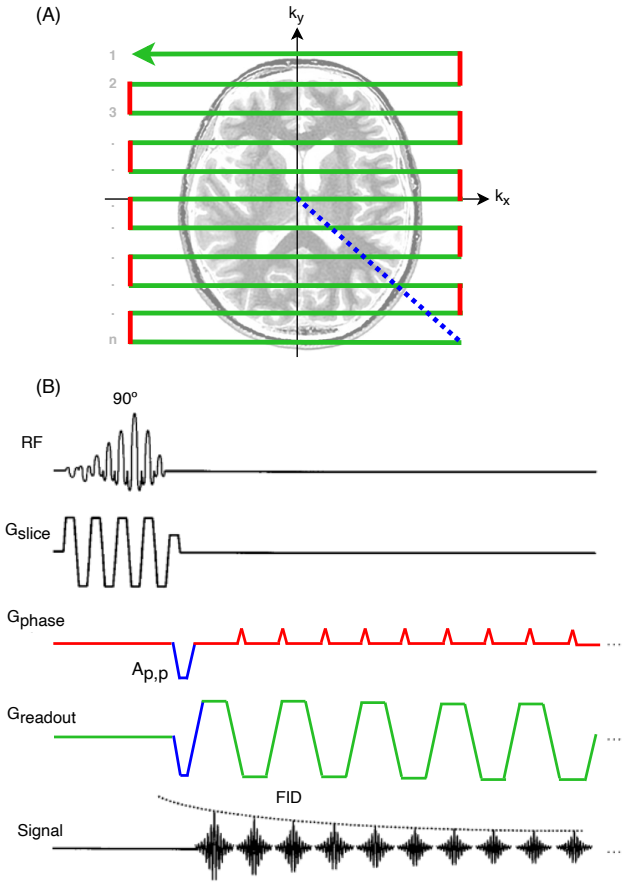

Figure 3.2: (A) - EPI k-space trajectory. (B) - EPI diagram of its k-space trajectory, with corresponding colours of what is executed by each gradient. Adapted from [7, 27].

3.1 Types of Sequence

There are two main types of MR pulse sequences: Gradient-Echo (GRE) and Spin-Echo (SE). All other sequences are modifications of these with slight variations but always based on those two [29].

In a **GRE sequence** - Fig. 3.3 - only one RF pulse and typically less than 90º, is combined with two frequency gradients with opposite polarities that rephase and dephase transverse magnetization M_z, which results in shorter TR's and faster imaging acquisitions. Despite this speed coming at a cost, as signal formation is also more sensitive to hardware related and tissue properties B inhomogeneities, advances in hardware improved Shimmming[1] and gradient performance while allowing the successful application of GRE imaging with reliable and reproducible image quality [29, 30].

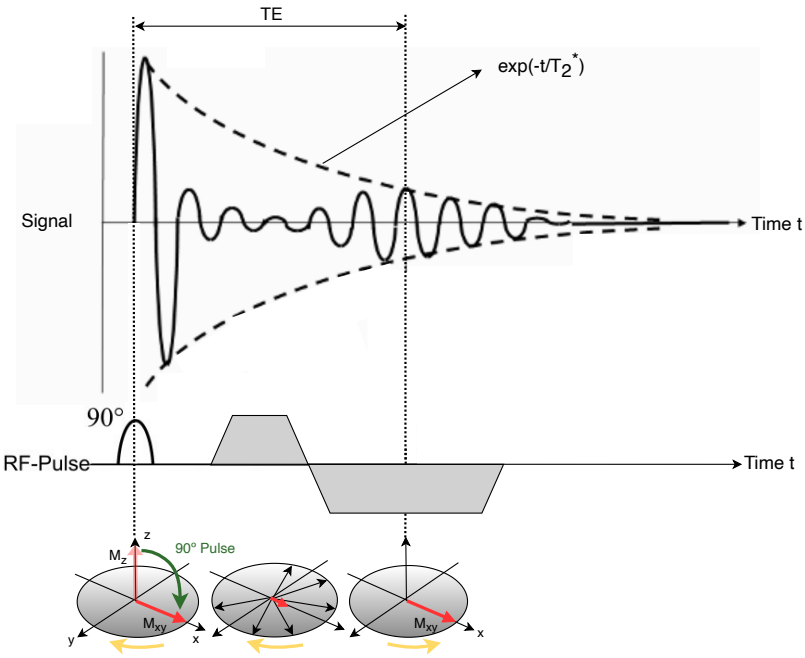

Figure 3.3: GRE Sequence with its signal decay (above) and corresponding states along time (bellow) with isochromats direction in yellow. Adapted from [30, 31].

A standard **SE sequence** - Fig. 3.4 - consists of an initial 90º excitation pulse, that flips the Net Magnetization into the transverse plane, progressively starting to dephase from that point due to T_2 effects. This occurrence will cause some spins to precess faster than others, and if a 180º refocusing pulse is introduced halfway between the excitation pulse and TE, faster spins will then be behind the slower ones, meaning they will all be in phase at TE, reversing the loss of phase coherence and overturning it to the original value. The refocusing pulse has the advantage of eliminating field inhomogeneity effects. Another analogy to this event can be seen in Fig. 3.5 for better understanding [3, 29].

[1] Term originated from Shimming Coils, which are EM coils that compensate for inhomogeneities in B_0 [3]

Typically SE sequences take very long to acquire, they are slow sequences, but some technology advances like RARE, Fast and Turbo Spin Echo have allowed speeding SE imaging although at a cost of image quality [32].

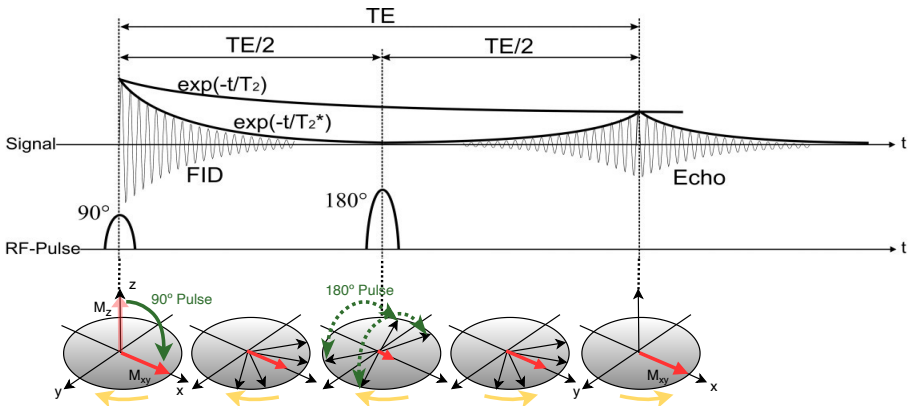

Figure 3.4: SE Sequence with its signal decay (above) and corresponding states along time (bellow) with isochromats direction in yellow. Adapted from [31].

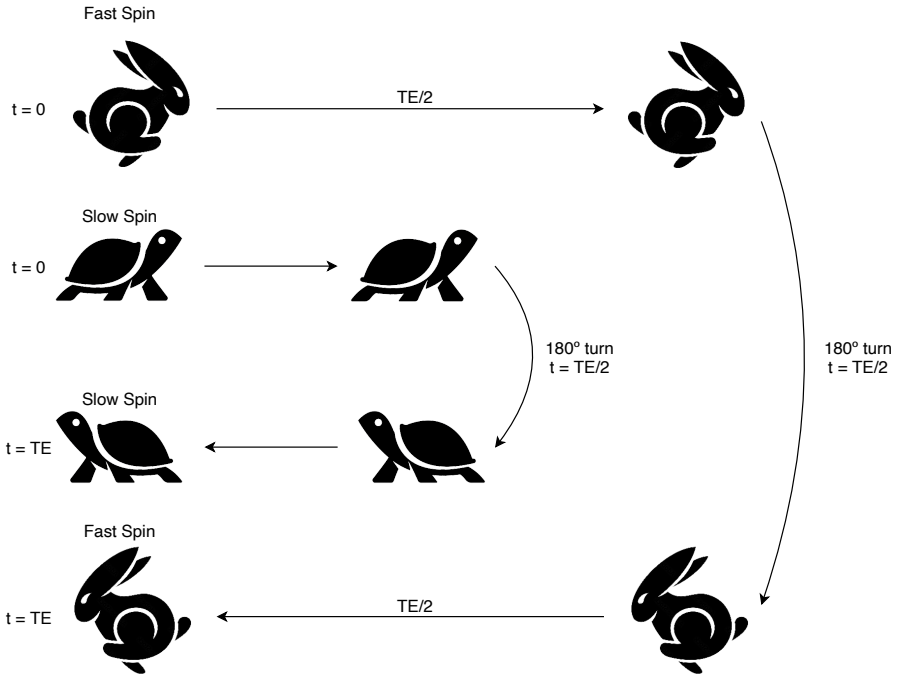

Figure 3.5: SE 180° refocusing pulse analogy. After the initial excitation pulse, B inhomogeneities will cause phase coherence loss, as some spins (rabbit) will be faster than others (turtle). If a 180° pulse is introduced midway at TE/2, the precession direction will be flipped, and at time TE all spins will have the original phases - as the rabbit and turtle return to the original position. Adapted from [3].

From the aforementioned sequences, some of the most common types of contrast that are obtainable will be:

- **Proton Density Contrast imaging**, based on the number of protons in a Voxel - three-dimensional volume element and basic sampling unit of an MRI, the smaller the Voxel, the easier it is to identify the brain fine structure, for e.g. - which depends on the type of tissue. Both SE and GRE echoes can be used as long as T_1 and T_2 contrasts are minimized. These types of images are also extremely useful for human brain segmentation, to understand damage or how atrophy alters its functional properties, and for high-resolution reference images to determine the anatomical structure of the brain, being extremely used in fMRI studies.

- **T_1 Contrast imaging**, as the name implies, comes from images whose voxels' signal intensity depend on the T_1 value of the tissue - shorter values mean that magnetization recovers faster and greater MR signal, like white matter and bone marrow, and starts reducing as it goes from grey matter to water. It's also one of the most used and basic in clinical scans, and both SE and GRE echoes can be used.

- **T_2 Contrast imaging** can only be obtained using a SE pulse sequence, as only these sequences allow true spin-spin relaxation that doesn't depend on field inhomogeneity. As mentioned in chapter 2, T_2 relaxation times are dependent on spin-spin interactions, so homogeneous tissues have a tendency to have higher signal, like fluid-filled regions like Cerebrospinal Fluid (CSF) and ventricles, other areas like grey matter have medium signal while white matter has the lowest, which is in agreement with their T_2 values.

- **T_2^* Contrast imaging** although similar, is the basis for BOLD-contrast fMRI as these images are sensitive to the blood's concentration of deoxygenated hemoglobin, which in turn varies according to the metabolic activity of neurons. It is widely used to generate brain's venograms - huge amount of deoxygenated hemoglobin - and it can also be achieved with a GRE sequence.

In short, while SE are RF-refocused, the removal of field inhomogeneity artefacts allows much later echo times, increasing T_2 contrast in these images, which is extremely useful for tissue characterization in medical diagnosis, on the other hand GRE imaging is gradient refocused and has echo amplitudes determined by T_2^*-decay [27, 30]

3.1.1 Echo Planar Imaging (EPI)

The total amount of MR signal that is obtained from a biological tissue can sometimes be extremely small, which isn't something that a researcher/clinician desires when using any Imaging Method. In order to achieve increased contrast and resolution, an improvement in spatial resolution is necessary, which can be attained by carefully decreasing signal from some tissues, while retaining signal from others. In what was previously discussed, this issue was dealt with by repeatedly signal sampling and building image data from there, however that would take too long and some acquisitions where time is key simply would not be feasible [23].

This way, EPI may provide the solution, as it is one of the fastest MRI Pulse Sequences that lowered the time scale in obtaining images from a couple of seconds down to a few tens of milliseconds, allowing reduction of motion artefacts like involuntary movement, heartbeat, blood flow or breathing. Besides providing a necessary tool to investigate some of the fastest events in the Human body, like neurofunctional brain mapping, cardiac imaging, blood flow interactions or even real-time imaging due to the shift in the time frame, it lowered examination times, allowing more unsettling patients to be examined while keeping the costs down [27].

An EPI pulse sequence works fundamentally different than conventional pulse sequences, allowing the formation of a complete image **under a single pulse excitation** - Fig. 3.6 (B) instead of several RF pulses like before - Fig. 3.6 (A). It differs mainly in how encoding is applied: a sequence of bipolar RO and phase gradients are used to generate a train of gradient echoes and to spatially encode several k-space lines, respectively, allowing both a more efficient sampling of k-space while the FID signal is still detectable [23] and ensuring adequate MR signal during the entire data encoding and collection period [27, 29].

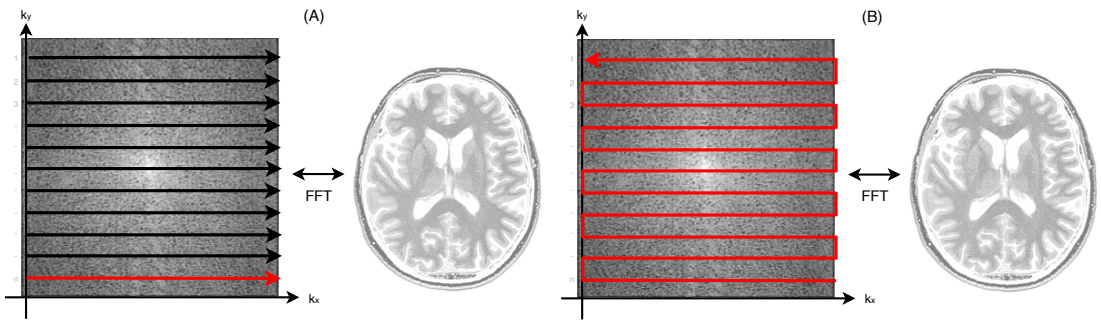

Figure 3.6: (A) - In other Pulse Sequences, for each line to be acquired an echo has to be produced; (B) - In EPI, a single echo can sweep all of k-space, speeding measurements. Adapted from [7, 27].

As a result of the single excitation pulse, all data must be acquired before considerable T_2 or T_2^* decay can occur, which - considering the average decay of tissues, 50 ms for muscle or 80 ms for the brain - needs to occur in that order of magnitude of up to 100

ms [32]. Thus, instead of individually collecting each k-space line - Fig. 3.6 (A) - the **whole of k-space data is quickly filled** using the referred rapid gradient switching in a **single and continuous trajectory** where most common patterns are to scan alternating lines in opposite directions - Fig. 3.6 (B). This constant switchback to allow acquisition in different directions overloads the gradient coil, plus the added inefficiency of data collection while changing k-space lines - vertical lines in Fig. 3.6 (B) which are not used in image creation - are some of the problems associated with this sequence. This means post-processing will be necessary to correct inconsistencies and misalignments - reversing every other k-space line, removing vertical lines, etc. as they will result in image artefacts, due to field inhomogeneities related losses in MR signal as well as geometric distortions due to the long time spent acquiring data after excitation - small field variations over time can considerably distort images [23, 27, 32]. More on that will be discussed in section 5.2.5. This zig-zag trajectory used in EPI although the most common, is not the only one, circular, radial, PROPELLER, etc. are other trajectories to mention that can solve some problems related to zig-zag but may have others [27].

Among others, the two most common types of EPI pulse sequences are **Gradient-Echo EPI (GRE-EPI)** and **Spin-Echo EPI (SE-EPI)** sequences, which will be the respective sequences' combination. Both rely on gradient echoes to sample multiple k-space lines however, in the first echoes are formed under the envelope of an FID, while in the second they are formed under the envelope of a spin echo. Also, comparing the pair, GRE-EPI has a heavier T_2^* weighting which is important in fMRI and BOLD contrast, and SE-EPI will have fewer artefacts as off-resonance effects are more easily minimized (B_0-field inhomogeneity, susceptibility variations, chemical shift[2], etc.) [27].

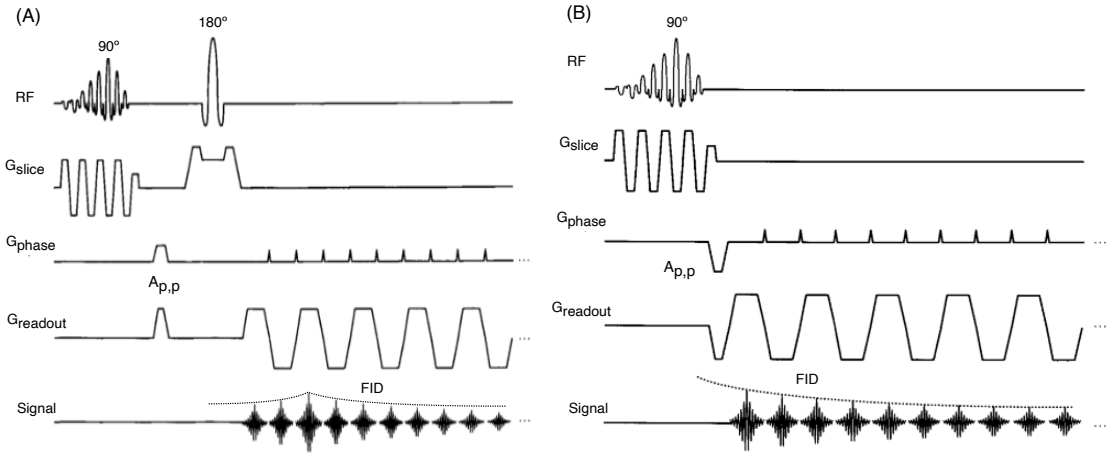

Figure 3.7: Diagram example of (A) a SE-EPI and (B) GRE-EPI. Adapted from [27].

Finally, EPI is an extremely useful and versatile imaging technique that allows clinical applications with very short imaging times and low sensitivity to motion. Any MRI

[2]Difference in proton resonance frequencies in different molecules due to shielding effects in a magnetic field [3, p. 132]

protocol that has been developed for lesion detection can be adapted to EPI, just by replacing the constant readout gradient used in conventional sequences by the EPI readout version, with a plus of both less vulnerability to motion artefacts and a higher probability of acquiring clinically useful images on claustrophobic and restless patients. Because EPI is one of the fastest MRI pulse sequences, it is of fundamental usage in Medicine for the numerous mentioned arguments and that is the reason denoising methods will be here applied.

3.1.2 Other Pulse Sequences

As mentioned before, besides EPI, there are many more pulse sequences like **Diffusion Weighting Imaging (DWI)**, where the molecular diffusion in tissues is measured with magnetic gradients, **Fast Low Angle Shot (FLASH)**, a GRE sequence combining a slice selective RF pulse, **Multi Slice Multi Echo (MSME)**, a sequence used to acquire images of the target at different TE's in order to create T_2 variation maps, **Rapid Acquisition with Relaxation Enhancement (RARE)**, a type of multi-echo SE sequence, commonly used for faster acquisitions as it can sample multiple k-space lines/trajectories following each excitation pulse, along others, which won't be the scope of this dissertation but are well documented in [3, 27, 33–35] for interested readers.

4

Denoising Strategies

As mentioned in Chapter 1, one of the most important parameters that can be used to determine whether an image has a higher quality than another is the SNR, which can be defined as the relative strength of a signal compared with other sources of variability in the data.

Albeit it is importance in imaging, there is no universally accepted method to measure SNR, highly due to the increased difficulty to estimate and measure both noise and signal. There are several ways to assess these parameters, as depending on the situation some will fit better than others, therefore the ideal case would be finding a method that is the most suitable for every circumstance encountered [36].

4.1 SNR Measurement

For the **signal estimation**, a very widely accepted and common approach is to use the pixel mean value S of the Region Of Interest (ROI) enclosing most of the subject we are interested in measuring [37].

For the **noise estimation**, due to its random nature, a probabilistic modelling might be the most appropriate solution. It is a common practice, with experimental evidences [38], to assume noise in both k-space and image domain to have a zero mean and spatially uncorrelated **Gaussian distribution**, which in turn can also be separated in real and imaginary components with equal variance. In the case where data was acquired using multiple coils, the same assumption is still valid [39]. This assumption is also commonly known in the literature as *white noise*, as a result of the latter being equally distributed along all frequencies [40].

On account of SNR being used for image comparison, thus having the requirement to be a single value, the magnitude signal $|Z|$ has to be calculated from the complex signal, pixel by pixel. As the operation in question is nonlinear, the pixel values corresponding to noise will no longer have a Gaussian behaviour, becoming a **Rician distribution** [39, 40]. Contrasting, outside of the ROI, theoretically there will only be noise without signal, so a special Rician case occurs, simplifying to a **Rayleigh distribution** - for a visual

interpretation see Fig. 4.1.

In addition, Fig. 4.2 can be observed for a better understanding of these concepts and how they relate to the acquired Signal.

For the actual **image noise estimation**, Henkelmen [37] suggests that from a magnitude image, the standard deviation SD of an ROI around a region with only noise should be taken - in this work a 27×27 rectangle on the bottom left corner was used - which should be divided by a factor of 0.66 to account for the Rayleigh distribution of noise in the magnitude image.

The respective ratio of Signal over Noise is illustrated in eq. (4.1).

$$SNR_{\text{SV}} = \frac{\text{Signal}}{\text{Noise}} = \frac{S(ROI_{\text{Image}})}{SD(ROI_{\text{Noise}})} \times 0.66 \tag{4.1}$$

As the latter will only provide a single value, another SNR estimation might be necessary to support a more visual assessment of a map with the SNR values. This way Miyati et al. [41] introduced a variation to the previous estimator, again using the ROI Mean signal intensity S, though using the standard deviation SD of the same ROI instead - eq. (4.2) - which again should be divided by a factor of 0.66 to account for the Rician distribution of noise in the magnitude image. The value won't be as large but allows an SNR Map image to be obtained.

$$SNR_{\text{Map}} = \frac{\text{Signal}}{\text{Noise}} = \frac{S(ROI_{\text{Image}})}{SD(ROI_{\text{Image}})} \times 0.66 \tag{4.2}$$

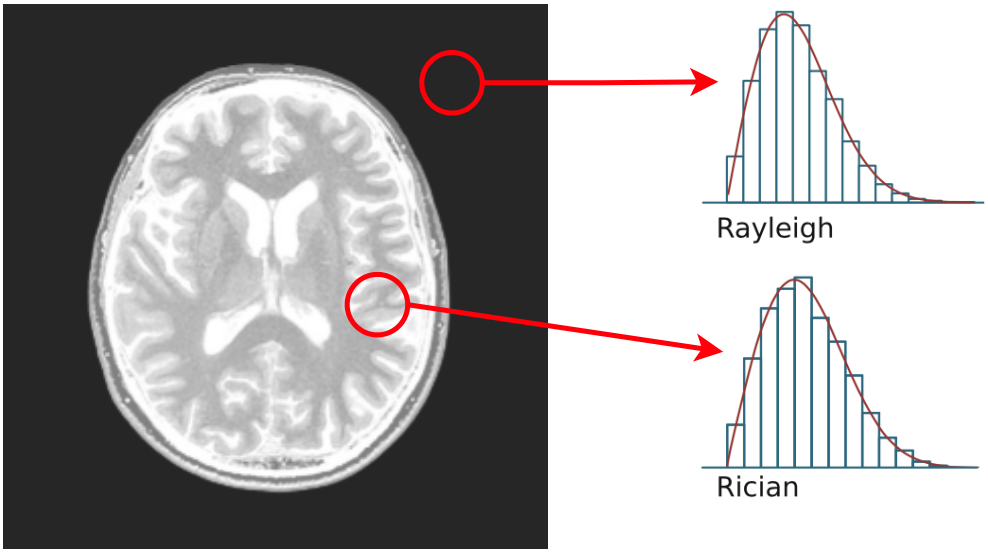

Figure 4.1: How noise distribution is displayed in an MRI. The object has a Rician distribution, and in the background simplifies into Rayleigh. Adapted from [7, 40].

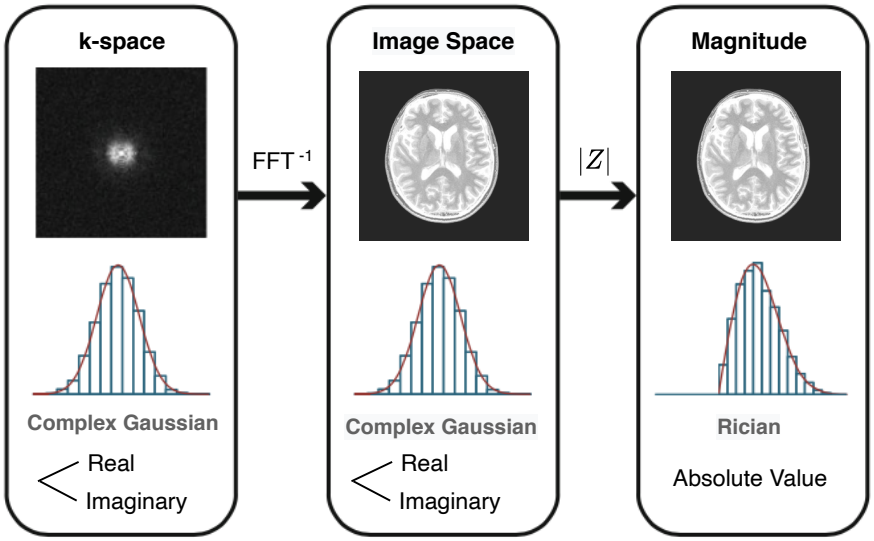

Figure 4.2: The object noise along k-space and Image Space will have a Gaussian distribution. The final image with Magnitude will have a Rician distribution. Adapted from [7, 40].

4.2 Denoising Strategies

Nowadays, it is more and more important to be able to retrieve meaningful information in the process of noise removal to obtain high-quality images. In the literature, noise removal can have several names: noise filtering, noise removal, denoising, or noise reduction, however they all converge to the same action of minimization of noise pattern in the image. As depicted in Chapter 1, many methods have been reported - and many more exist - that remove noise from MRI datasets based on signal estimation, anisotropic diffusion, Independent Component Analysis, machine learning, wavelets, etc. [40], meaning there won't be a perfect version of Denoising. The only required condition is that a good noise removal method must not **invent new data** or **remove existent data**, only estimating the signal from data with noise, thus accurately keeping the essential information [40].

Some of these proposed methods were favoured by the MRI community in the last years due to their capability of removing spatially varying and non-Gaussian noise in magnitude MR data. In 1933, Hotelling [42] was one of the pioneers of noise removal via converting a redundant dataset into a Principal Component basis, and being able to only preserve the signal-carrying principal components by "*perhaps neglecting those whose contributions to the total variance are small*" [43]. Undoubtedly this is what today is called PCA which, over the last couple of decades has surged amongst the science community as a novel denoising scheme that starts to show promise and results in noise reduction, while preserving image features [44, 45].

4.2.1 Principal Component Analysis (PCA)

PCA is hence a classical decorrelation technique tool used to transform the mentioned input variables into a new lower dimension space using the correlation matrix largest eigenvectors, or in a more practical way, it is the replication of the target data in a new coordinate system in which the basis vectors follow the greatest variance [46, 47].

Invented in 1901 by Pearson and presented in its algebric form by Hotelling in 1933 [42, 48], PCA is additionally a method of identifying and expressing data patterns in order to highlight their similarities and differences. Since patterns are difficult to find in high dimension and complex data, by being a dimensionality-reduction method - a large set of variables can be transformed into a smaller one maintaining the important information - this method is extremely useful in analysing large data sets with lots of information, like the ones in statistics, signal, image processing, etc. [49].

Recalling, a **denoising algorithm**'s most basic idea is **removing noise** while **restoring the original image**. Here, opposing details like *noise*, *edge* and *texture* are all *high-frequency components*, becoming difficult to differentiate between one another in a denoising process. If the small high-frequency coefficients are set to zero - retaining the maximum possible important signal while removing noise - the final product may end up losing some details [49, 50].

As stated before, in order to minimize loss of original features and improve SNR, PCA is one of the techniques that has had great success over the recent years, as it creates new images from uncorrelated values of different images [47]. After standardization, this is achieved by transforming the original dataset into the PCA domain and finding the most significant **principal components** of the data - new variables constructed as linear combinations of the initial variables [48] - with the most variance, which are combined into what is known as their covariance matrix. This is achieved by having several repetitions of the same slice, demonstrating data has a high redundancy and its analysis shows most of the **signal variance** is contained in a few specific components, whereas the **noise** is spread over all data [43, 45].

An alternative to the PCA technique, Singular Value Decomposition (SVD)-based denoising works under the same principles of low-rank matrix dimension reduction and both signal and noise components data breakdown, which also has been showing good results in the final observable image [44, 51].

4.2.2 Marchenko-Pastur (MP) Distribution

However, as per Razifar et al. [52], studies done with different medical imaging tools, including MRI, suggest that PCA has difficulty in separating signal from noise when the latter magnitude is relatively high, thus having the data low SNR. This way, a novel way of separating signal from noise ought to be proposed: a model-independent local noise estimation method based on the Random Matrix Theory (RMT), first studied by Eugene Wigner and Freeman Dyson in 1955 and 1962, whose results can be used to analyze noisy

covariance matrices and can be coupled with PCA to exploit the redundancy in MRI data, which is often achieved by a local or non-local selection of image patches, especially in spatially varying noise cases [53].

In 1967, using RMT and Wigner's discoveries, Vladimir Marchenko and Leonid Pastur derived an equation that serves as the MP distribution [54]. Here, when in a very large matrix, the noise contribution to the histogram of the PCA eigenvalues becomes deterministic and is well defined by the universal MP distribution - Fig. 4.3. Experiments and simulations done by Veraart et al. [55] shows this method, MP-PCA, outperforms existing common methods in terms of precision and accuracy.

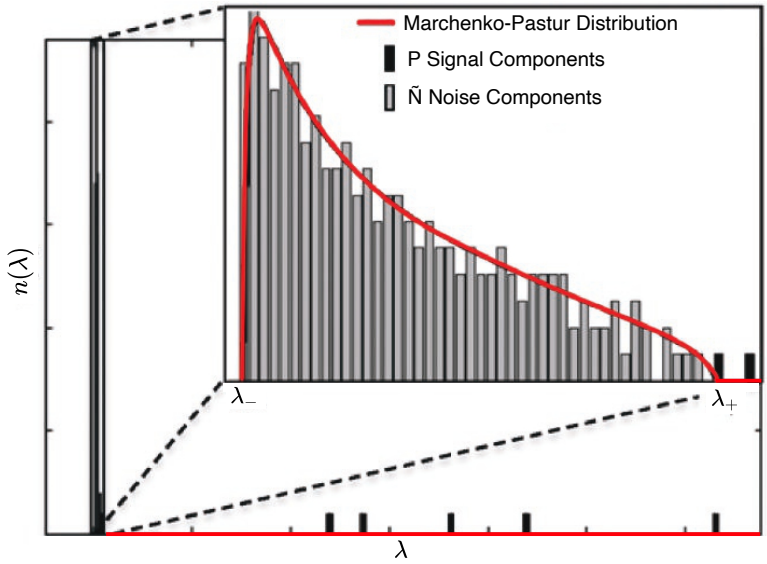

Figure 4.3: Covariance matrix eigenvalue spectrum with MP Distribution superimposed. Adapted from [55].

Using square patches of MRI data, by the principles explained above, SVD can be used to find the eigenvalues λ of the covariance matrix, which will have P eigenvalues associated with Signal itself, and $\tilde{N}$ eigenvalues associated with Noise. As long as either matrix size is much larger than the P-value and after sorting them in a descending order, the eigenvalues λ are expected to be distributed according to the universal "quarter circle" law - eq. (4.3) where $\lambda_{\pm} = \sigma^2(1 \pm \sqrt{\gamma})^2$, σ is the noise standard deviation and γ is the matrix size ratio.

$$p(\lambda|\sigma,\gamma)\begin{cases}\frac{\sqrt{(\lambda_+-\lambda)(\lambda-\lambda_-)}}{2\pi\gamma\lambda\sigma^2} & \text{if} \quad \lambda_- \leq \lambda \leq \lambda_+ \\ 0 & \text{if} \quad \lambda \geqslant \lambda_+\end{cases} \tag{4.3}$$

Here, there is a well-defined curve between λ_- and λ_+, with the $\tilde{N}$ Noise eigenvalues - grey rectangles - well distributed, and if $\lambda > \lambda_+$ the curve will be zero, thereby with just P Signal eigenvalues - black rectangles. Thus the upper edge λ_+ is able to efficiently separate the desired *noise* and *significant signal-carrying principal components* - Fig. 4.3. These boundaries $\lambda_\pm$ are dependent on noise standard deviation σ and matrix size ratio γ, being a good estimation of the noise present in the analyzed dataset [54, 55]. More details on the exact expression are well documented in [54, 55] for those interested in more details. Worth emphasizing that, depending on the noise level, some of the significant noise eigenvalues can fall beyond λ_+, becoming "invisible", and so impossible to remove [55, 56].

5

Experimental Method

5.1 MRI Protocol

All MRI experiments were conducted on a 9.4T horizontal MRI scanner (BioSpec 94/20 USR, Bruker BioSpin, Germany) equipped with a gradient system capable of producing up to 660 mT/m in all directions. An 86 mm resonator volume coil was used for transmittance, and a 4-channel array surface cryocoil was used for reception, allowing SNR enhancing. Imaging was performed using Paravision 6.0.1 (Bruker Biospin MRI GmbH, Ettlingen, Germany).

All animal experiments reported in this thesis were preapproved by the competent national and international authorities and conducted according to EU directive 2010/63.

The files obtained from the MRI scanner were as follows: an ***FID*** file with the complex data obtained from the scanner, a ***Method*** file where every parameter of the acquisition is depicted, and a ***pdata*** folder with Bruker's reconstructed image obtained from the data, among others. It's relevant to emphasize the latter corresponds to the raw reconstruction of the image, no post-processing is executed and is what most researchers use since it is the easiest to obtain, however not always the best. From the first two files is possible to reconstruct the pipeline that follows.

5.2 Pipeline

In order to obtain our final image, a pipeline was created with the necessary steps to achieve our goal. From organizing and reshaping raw complex data to ghost correcting the data, using MP denoising and finally reggrid it to the final image, those are some of the steps of the pipeline which are summarized in Fig. 5.1 and will be thoroughly described in the following subsections. Although presented with this order, for future work some of these steps may be interchangeable as required.

Besides EPI, the pipeline is also fully optimized for obtaining images for the following 3 Pulse Sequences: Fast Low Angle Shot (FLASH), Multi Slice Multi Echo (MSME) with T_2 mapping and Rapid Acquisition with Relaxation Enhancement (RARE), all briefly

described in section 3.1.2.

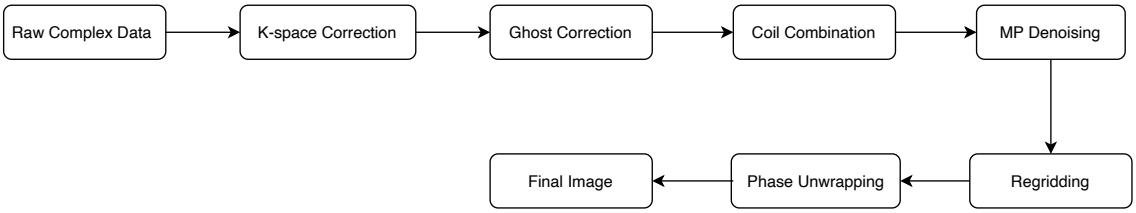

Figure 5.1: Pipeline Schematics.

5.2.1 K-Space Correction

After being decrypted from a 32 bit file, the *FID file* is a long vector that contains alternating real and imaginary data that must be reshaped to the correct dimensions. As depicted in section 3.1.1, every other k-space line must be reversed to be correctly organized and ready to be processed, so that the trajectory in Fig. 3.6 - (B) can almost be turned into (A), while taking into consideration regridding, which will be further discussed ahead in section 5.2.5.

5.2.2 Ghost Correction

As described in section 3.1.1, due to alternating EPI RO lines, eddy currents and imperfect gradients, inconsistencies between k-space lines of opposite polarity can be created – odd and even echoes - and manifest in the image as *Nyquist* or *N/2 Ghosts* – Fig. 5.2 - (A). These types of artefacts are regularly corrected by **Navigators**, acquisitions that can be used to reverse object displacements and phase shifts between alternating RO lines, just by recording tissue movement during a segment of the acquisition, thus correcting the degraded image [27, 57]. Nonetheless, those navigators are extra echoes or reference data acquired during the experiment, taking the time that, if removed, may be valuable to decrease imaging time, hence **Referenceless Methods** were proposed.

Here, EPI data itself is used for correction by defining the cost function that is minimized when the data is ghost-free. As the phase difference can be modelled like a 1^{st} order polynomial only dependent on phase ϕ and pixel shifts κ between lines, the minimization of the cost function can be achieved by estimating ϕ and κ solutions [58].

The ghost correction that was used in the pipeline is an adaptation from the Referenceless Method code created by Mckay and et al. [58], consisting of the SVD method, the cost function $f_{cost}(\phi, \kappa)$ is calculated based on the singular value decomposition of k-space after rearranging into a linear growing kernel which will produce the final ghost corrected image - Fig. 5.2 - (D).

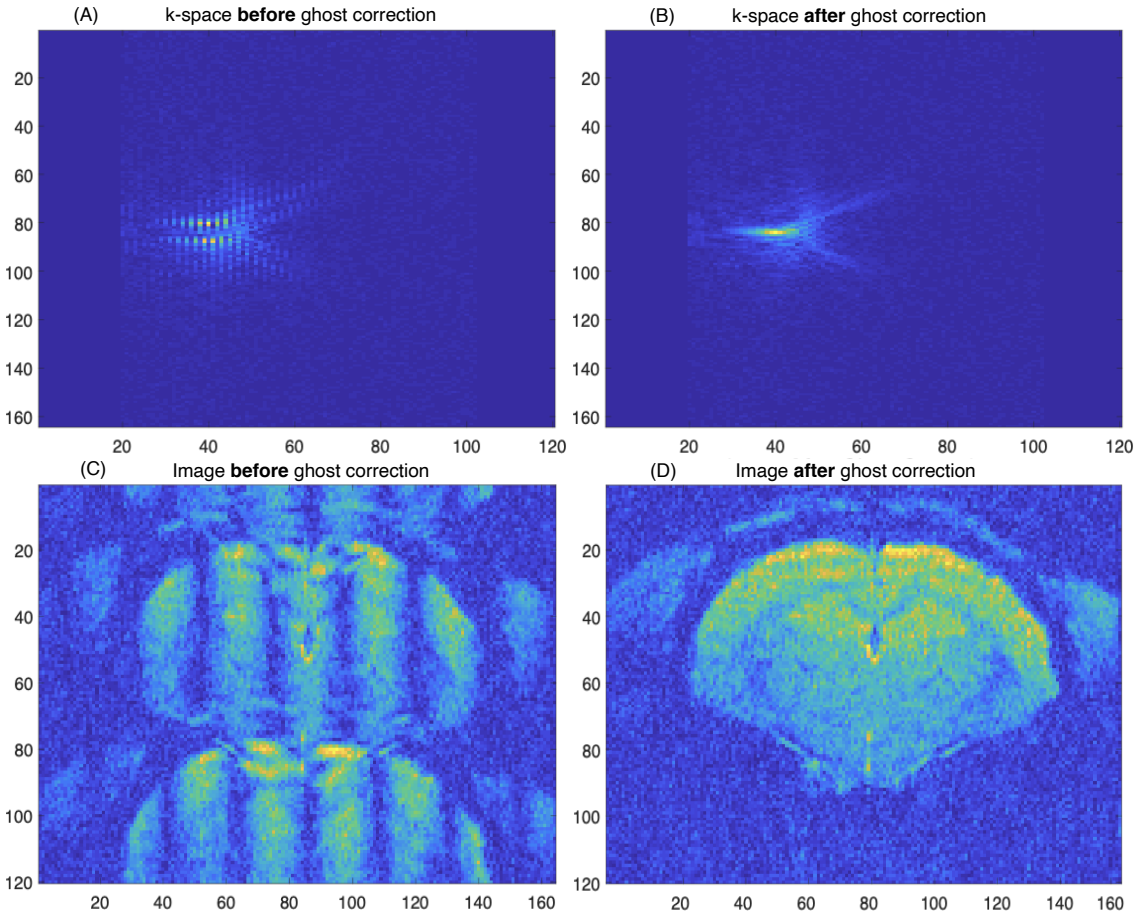

Figure 5.2: Above, k-space before - (A) - and after - (B) - ghost correction. Bellow, image before - (C) - and after - (D) - ghost correction. In (A), the odd and even lines are misaligned, and in (B) are correctly placed. In (C), the odd and even echoes and respective resulting ghosts are clearly visible, which are corrected in (D).

5.2.3 Coil Combination

In some special cases, the data might have been acquired by 4 channels, instead of the usual one. Nowadays many scanners allow for simultaneous signal acquisition in a phased array system. These types of systems use multiple detector coils and were originally developed not only to improve spatial coverage while maintaining high sensitivity [3] but also to reduce scanning time, avoiding problems with moving structures [59]. Here, coils are distributed around the object that will be scanned, and each will be more sensitive to the areas which are closer, leading to a non-uniform spatial sensitivity acquisition [40]. In order to get the final magnitude uniform image, as each coil has one complex image available, a combination into one will be necessary.

There are several methods that are used to achieve a correct Coil Combination, particularly the Sum-of-Squares (SoS) which has become sort of a universal choice, yet introduces signal bias over-increasing signals magnitude, while other methods may either need coil

sensitivity pixel-by-pixel which many times isn't available [60]. On the other hand, another common method that doesn't have those issues is the **Weighted Coils Combination Method**. Here, each channel N_c can be reconstructed independently and combined to a single image using eq. (5.1), with the weighted sum $b_c \cdot |S_c|$ for all 4 Coils, where b_c corresponds to the specific Coil weight determined by the SNR map median for the masked Coil Image S_c over the sum of the weights [60, 61].

$$CC_{\text{SNR}} = \frac{b_c \cdot |S_c|}{\sum_{c=1}^{N_c} b_c} \tag{5.1}$$

In Fig. 5.3 on the left the images acquired by individual coils in a four-element phased array can be observed. Although all coils are simultaneously active and receiving data, it's possible to understand that each image has no coupling to the rest - no superimposition is seen image-wise. Since the images have no signal transferred between Coils, that also has the same implication for Noise, no significant parcel is transferred, being each coil independent from one another without noise correlation [61].

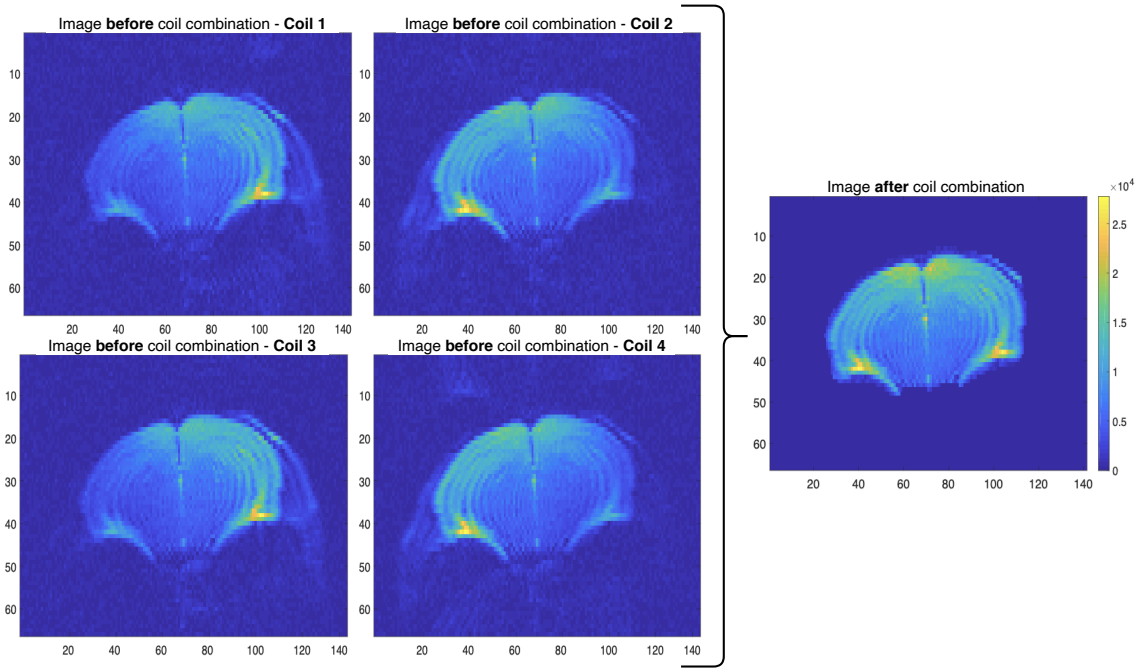

Figure 5.3: On the left, the 4 coils images can be observed with an increased magnitude depending on the position of the coil and on the right, the image with the combination of all 4 coils. The colormap scale is the same for all images.

5.2.4 Marchenko-Pastur (MP) denoising

As previously explained in section 4.2.2, after processing the data and obtaining the corrected image, the noise removal can finally be applied. The denoising method here implemented was originally created by Jonas Olesen, Mark Does and Sune Jespersen for diffusion MRI (dMRI) data [62], another pulse sequence though the code can also be used for all MR sequence, and was based on the algorithm presented by Veraart et al. [43]. The denoising inputs are the target Image with its Repetitions, which can be either the Image itself or its k-space, and the patche's Window Size, where the denoising will be applied. This window size may be either 2D or 3D, ranging from 1 to the image dimension, and as per [62] the ideal window size should be $\sqrt{\text{No. of Repetitions}}$.

More on that subject will be elaborated in chapter 6 and 7, but the **ghost corrected k-space** was chosen to be denoised. The before and after denoised images can be seen in Fig. 5.4 (A) and (B).

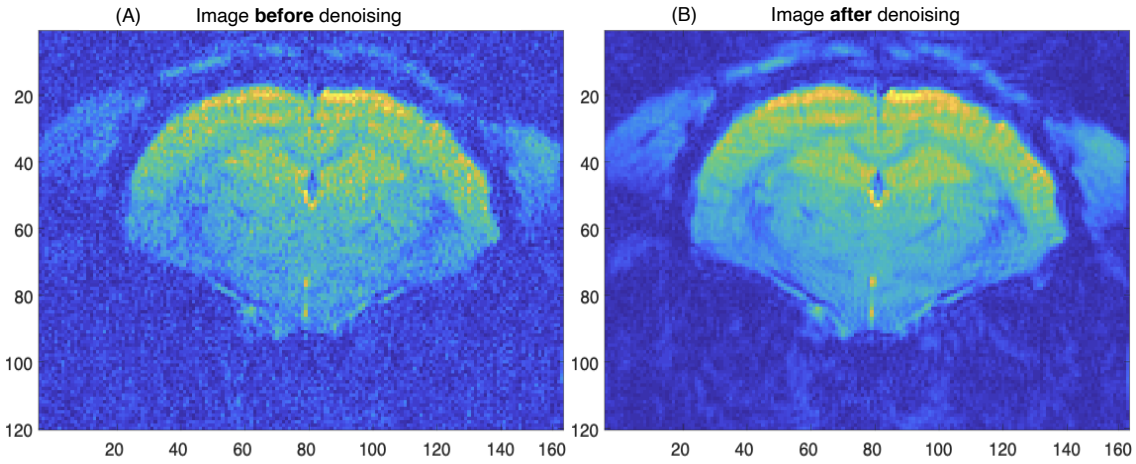

Figure 5.4: (A) - Image before and (B) after denoising image (A) is the same as the ghost corrected image in Fig. 5.2 (D).

5.2.5 Regridding

As reported in section 3.1.1, due to the single excitation pulse used in EPI, although it allows increased speed in image acquisitions among other benefits, the use of the non-conventional non-Cartesian trajectory introduces new problems that create inconsistencies and misalignments which need correction and will otherwise result in image artefacts and geometric distortions.

The use of non-Cartesian trajectories makes it impossible to directly use the FFT due to the interpolation difficulty to go from the measured grid to the Cartesian grid - or from the measured trajectory to the "perfect version" like the one in Fig. 3.6 (A). Therefore, more complex methods have to be employed, like the Regridding algorithm which interpolates the k-space data to a cartesian grid before applying the inverse FFT [63].

This process was originally created by Brouw in 1975 in the context of radio telescopes and synthetic aperture imaging [64], was first adapted to CT by O'Sullivan in 1985 [65] and later introduced to MRI, granted the possibility to use non-uniform k-space trajectories without extra artefacts when acquiring the final image [66].

The **regridding** algorithm is summarized in Fig. 5.5. The first step is to density compensate the image, which makes a correction for the increased k-space sampling density in case its trajectory is non-uniform - that would introduce unwanted weighting, ultimately blurring the image [63]. Afterwards, each k-space point $k(x)$ is distributed along some trajectory to a $W \times W$ Cartesian Grid $CG_{\mathrm{W\times W}}$ via convolution with an interpolation kernel K, usually a Kaiser-Bessel window K_{KB} [63, eq. (3.1)], as illustrated by Fig. 5.6. This step translates to a k-space that is regridded to an oversampled and larger matrix - Fig. 5.5 (1). Afterwards, the inverse FFT is applied to acquire the regridded image - 5.5 (2) - which will be much larger than intended, meaning an image crop is necessary to obtain the original size - Fig. 5.5 (3). At last, because a convolution with the interpolation kernel K_{KB} was performed which gave the image a non-uniform weighting, that "weight" needs to be removed via an operation known as deapodization. The apodization function is achieved by the FFT of the interpolation kernel, and after dividing the image by this new function, any existing weighting is removed - Fig. 5.5 (4) [63, 66] .

Due to the smoothing effect of the convolution, it is much less susceptible to errors than just a direct interpolation. The Regridding performance depends largely on the size of the gridding kernel: it can't be too small or it won't have the accuracy, it can't be too big or it will need an enormous computational power [66].

In Fig. 5.7 it is possible to observe both the before and after regridding images, where less ringing and artefacts around the image are visible.

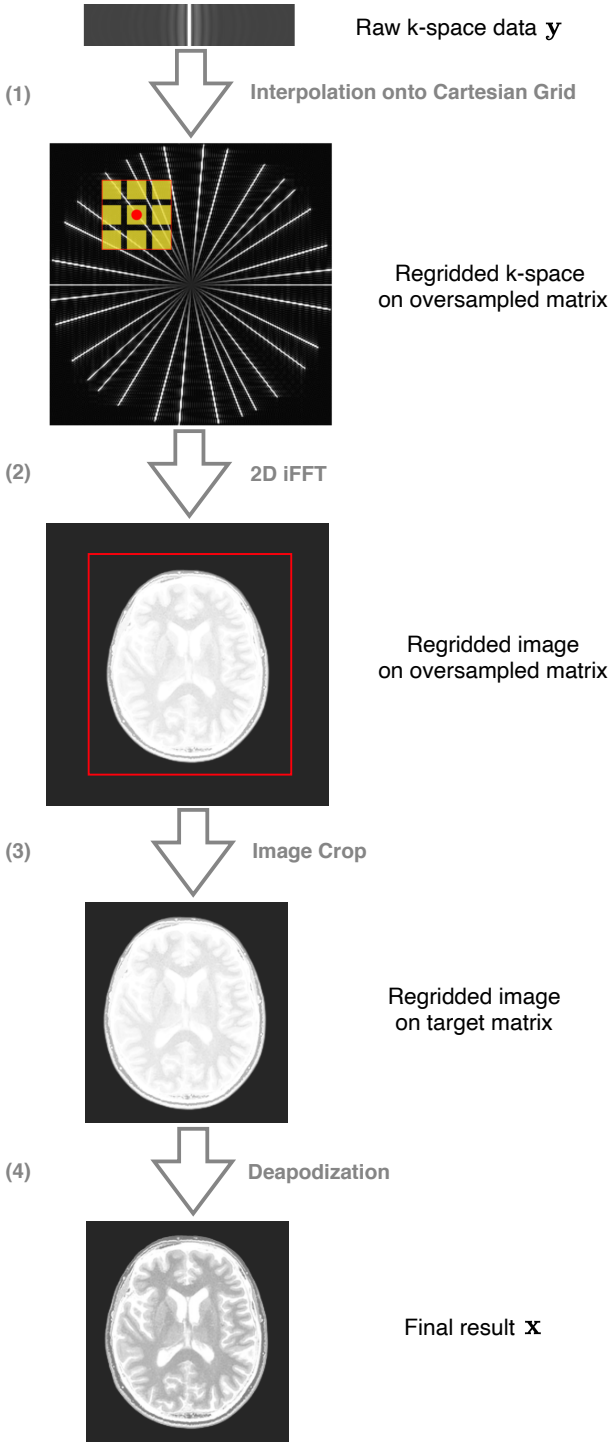

Figure 5.5: 2-D Regridding. (1) The k-space data is first density compensated and convolved to a larger Cartesian Grid, followed by a 2-D inverse FFT (2). Afterwards, the image is cropped (3), and finally, Deapodization is applied to remove the unwanted image modulation (4). Adapted from [7, 63].

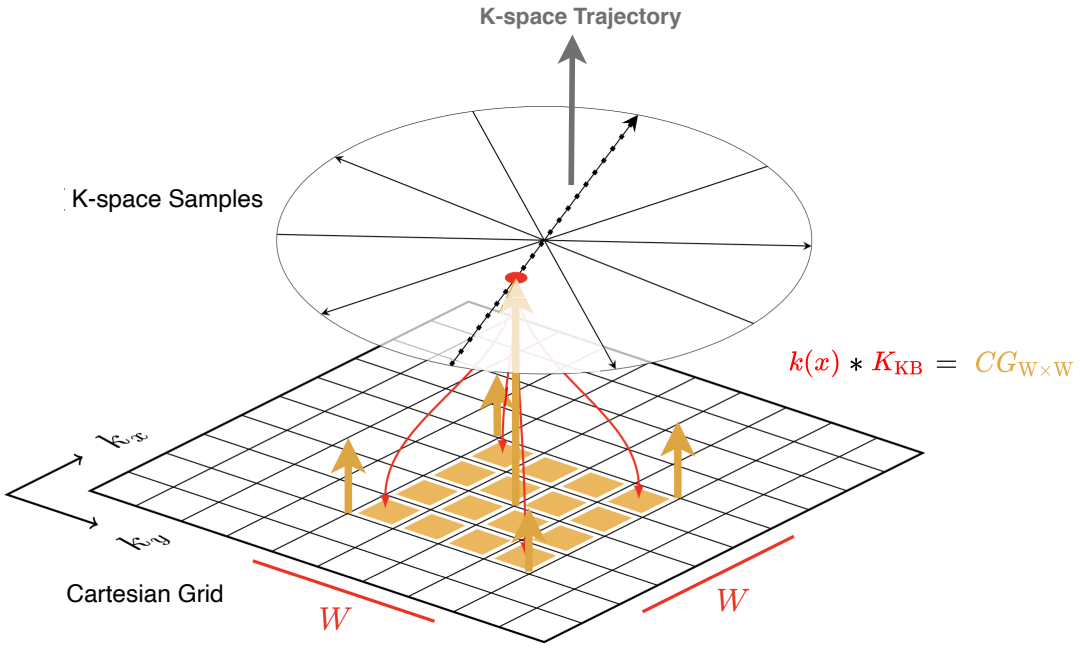

Figure 5.6: Each Sample $k(x)$ is distributed onto a $W \times W$ Cartesian Grid $CG_{\mathrm{W\times W}}$ via convolution with the interpolation kernel K_{KB} in step (2) of Fig. 5.5. Adapted from [63].

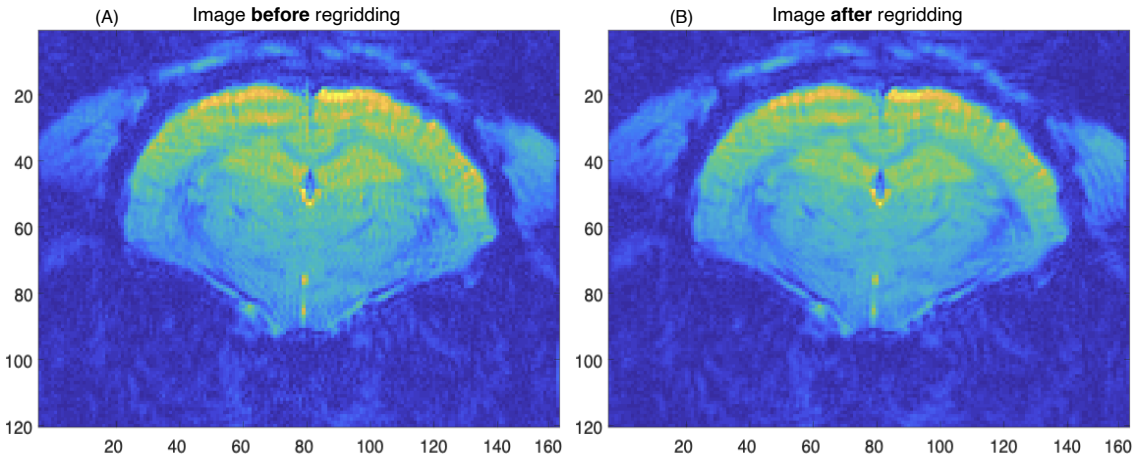

Figure 5.7: (A) - Image before and (B) after regridding, where it is possible to see, although subtle, reduced ringing. Image (A) is the same as the denoised image in Fig. 5.4 (B).

5.2.6 Phase Unwrapping

Considering an MRI is complex based, there are 2 types of information that can be obtained: Magnitude $|Z|$ and Phase ϕ. Although the phase information may be ambiguous, and the reason why the magnitude image is preferred for clinical diagnosis, it may contain important information which can only be decoded from the signal phase. Given any complex data, by definition, the phase can only be a value between [-π, π], meaning any angle outside that interval has to be *wrapped around*, adding/subtracting multiples of 2π to reveal the true phase. The removal of these extra angle turns is named **Phase Unwrapping** [67].

Having a non-uniform phase along the image slice is caused by small deviations from the resonance frequency induced by residual magnetic field inhomogeneity [68] which can cause considerable geometric distortions to datasets, hence the importance of unwrapping the image as corrections use field maps without phase discontinuities [69].

Additionally, Eichner et al. [70] demonstrate that in low-SNR regions data is dominated by noise floor related to the noise non-Gaussian distribution which affects overall signal estimation [71]. To remove that bias, the **real component of the image** should be used so data is dominated by a zero-mean Gaussian noise distribution, yielding MRI data without noise bias [72].

MRI phase maps may also have several other applications like susceptibility-weighted imaging, human brain phase imaging, mapping magnetic field inhomogeneities, quantifying blood flow velocity, characterizing chemical shift effect, temperature mapping and EPI distortion correction [68].

The unwrapping method used in the pipeline was created by Spottiswoode et al. [73] and adapted from Ghiglia and Pritt [74]. The before (A) and after (B) unwrapping images and corresponding image phases - (C) and (D) - can be seen in Fig. 5.8.

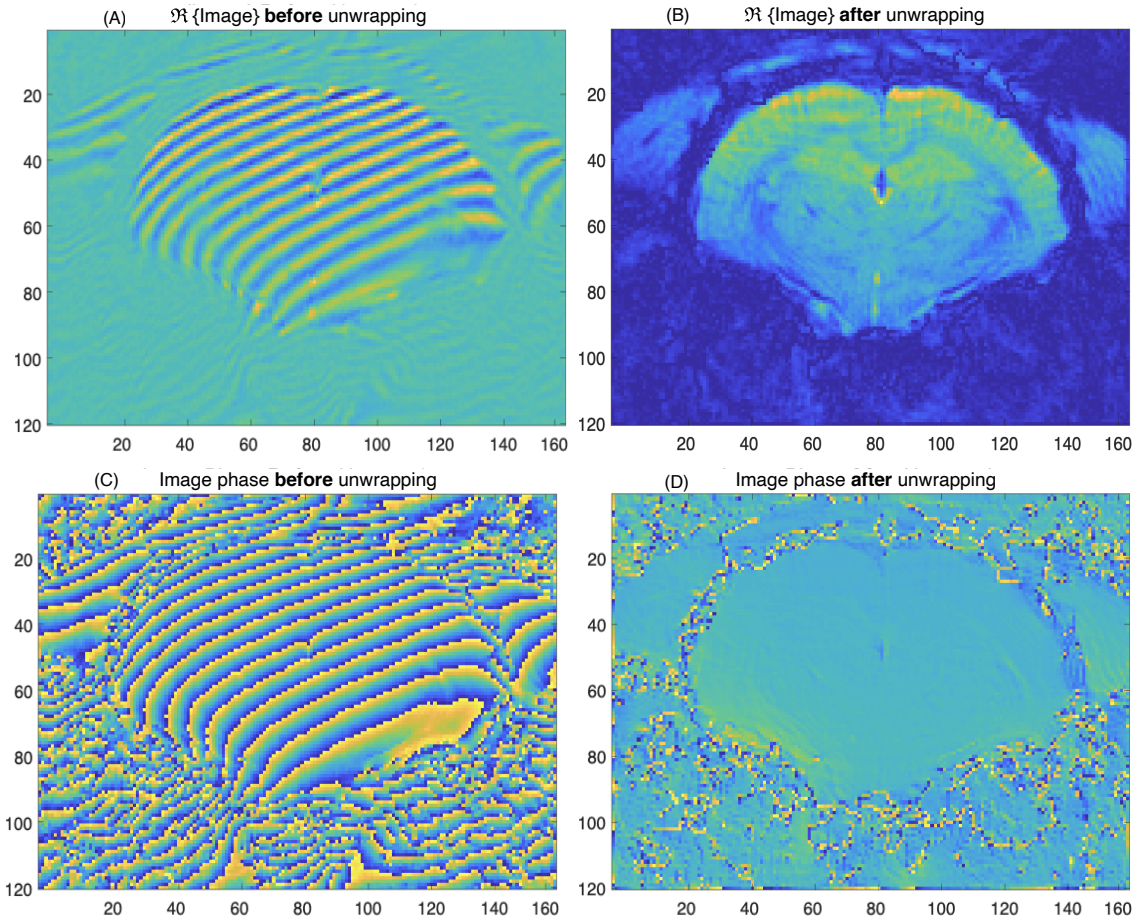

Figure 5.8: (A) - Real component of the image before and (C) after unwrapping, and corresponding image phase in (B) and (D).

5.3 MRI Pulse Sequences: Imaging Parameters

Two different pulse sequences were used in this study: an EPI fMRI sequence and a Diffusion EPI. In the first sequence, 306 repetitions of 12 slices were taken with a thickness of 0.65 mm and a phase encoding direction from left to right. The sequence was applied with a matrix size of 164 × 83, a Field of View (FOV) of 20.5 × 15 mm^2, a TR of 1500 ms, TE of 16.7 ms, a bandwidth of 375 000 Hz and a partial Fourier Factor of 1.44, which means only 72% of k-space in the phase-encoding direction was acquired, and so the matrix has to be zero-filled on either side in order to have the same size as Bruker's version (164 × 120). This sequence was also collected using just 1 coil fitting the case of **single channel**.

In the second sequence, 632 repetitions of 5 slices were taken with a thickness of 0.85 mm and a phase encoding direction from left to right. The sequence was applied with a matrix size of 141 × 66, a FOV of 16.66 × 12 mm^2, a TR of 3000 ms, TE of 57.8 ms, a bandwidth of 250 000 Hz and acquiring the full k-space in the phase-encoding direction.

In addition, the number of averages was 2, meaning the signal was accumulated twice prior to reconstruction, which will translate to a higher SNR and this sequence was also collected using 4 coils fitting the case of **multichannel**.

Also in this sequence, due to a non-uniform signal sampling in the readout gradient ramps, a *compensation* for the resolution loss had to be done - acquisition of more points in the EPI trajectory. This will result in a post-correction requirement, a k-space crop that can only be done after regridding, when the points have been sampled to a cartesian grid, to obtain the same size as Bruker's version (92×66).

Finally, to avoid any confusion, it's important to clarify that the term *channel* is the same as *coil*.

6

Results

In the following sections, the most relevant results of both Single Channel and Multichannel are presented as well as the experiments related to when and how should Denoising be applied.

As stated in section 5.1, it is possible to find in the ***pdata*** folder the Bruker's reconstruction of the complex data, which is the simplest version of the image and both the easiest and most used version by researchers. This image will be the **standard** throughout this work to understand whether quality improvements exist. To remove outside noise which may bias analysis, the same mask was applied in every image.

6.1 Experimental Data - Single Channel

In the Single Channel case, the section "*Comparison between the vendor image and the denoised image*" used k-space after ghost correction with a Window Size of 48, section "*Denoising k-space vs image-space*" compares both denoising options and "*Denoising window*" highlights how SNR develops as the Window Size increases. All SNR maps were calculated using the mean of the first 25 repetitions.

6.1.1 Comparison between the vendor image and the denoised image

In Fig. 6.1 it is possible to see the Bruker's image in (A) and the Proposed Reconstruction (PR) image in (B). Both images are visually similar and so is their SNR histogram - both SNR_{Map} means 5.18 ± 0.47 and 4.38 ± 0.43 (SNR Mean μ ± SNR Standard Deviation σ), while the other SNR_{SV} parameter, which may be considered more truthful and reliable as it represents noise variation more accurately, will be 21.05 and 16.97 respectively. Thus, as both relative differences are bellow 20%, 15.44% and 19.38% respectively, the image's visual similarity and resembling histograms confirm the hypothesis that the PR is at the same level of image reconstruction as the scanner's manufacturer.

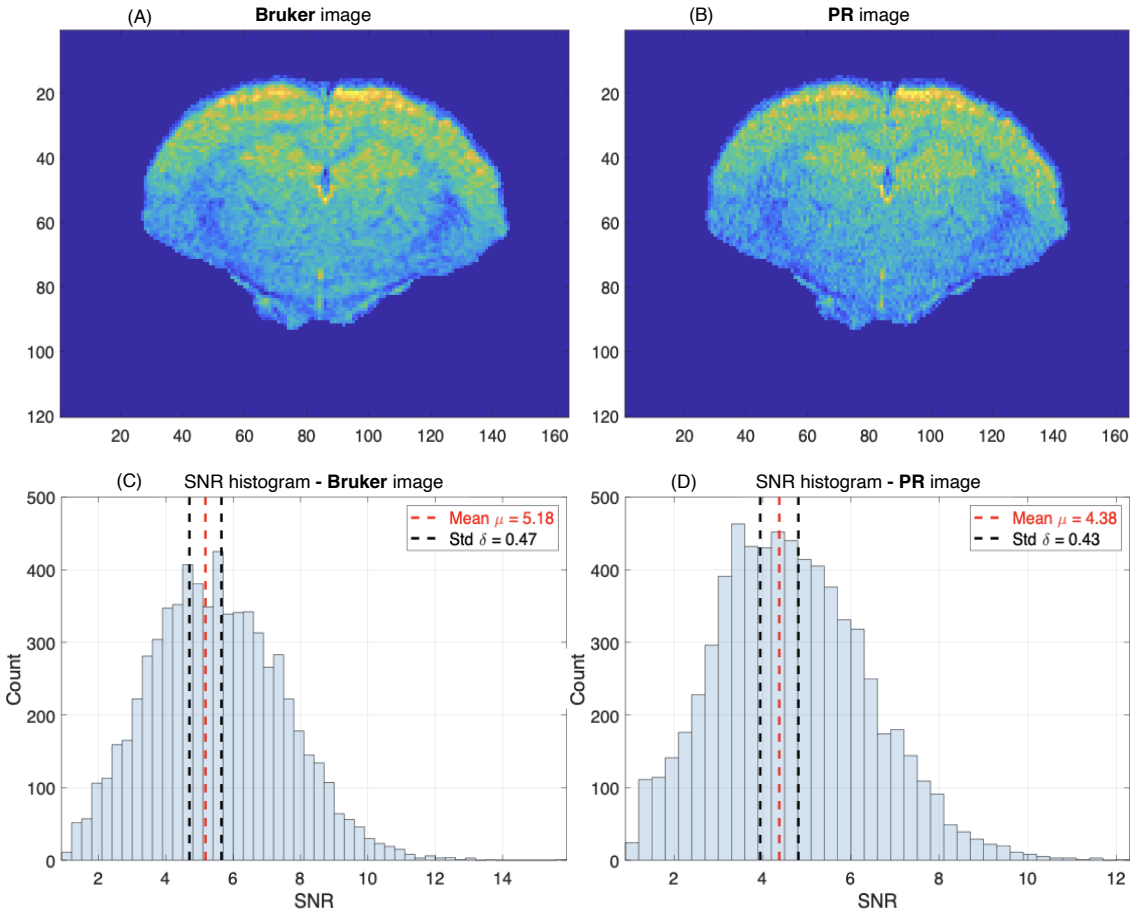

Figure 6.1: Side-by-side comparison between (A) the Bruker image and respective histogram in (C) and (B) the Pipeline Reconstruction (PR) image and respective histogram in (D). It's possible to see the visual similarity between images.

Afterwards, **Denoising** was applied to Fig. 6.1 (B), resulting in the denoised PR image - Fig. 6.2 (B). In (A) the Bruker image can be seen for comparison, and with their SNR histograms it is possible to see an increase of the SNR_{Map} mean from 5.18 ± 0.47 to 20.92 ± 2.61, which corresponds to a relative increase of 303.86%. The SNR_{SV} increases from 21.05 to 69.85, a relative increase of 231.83%.

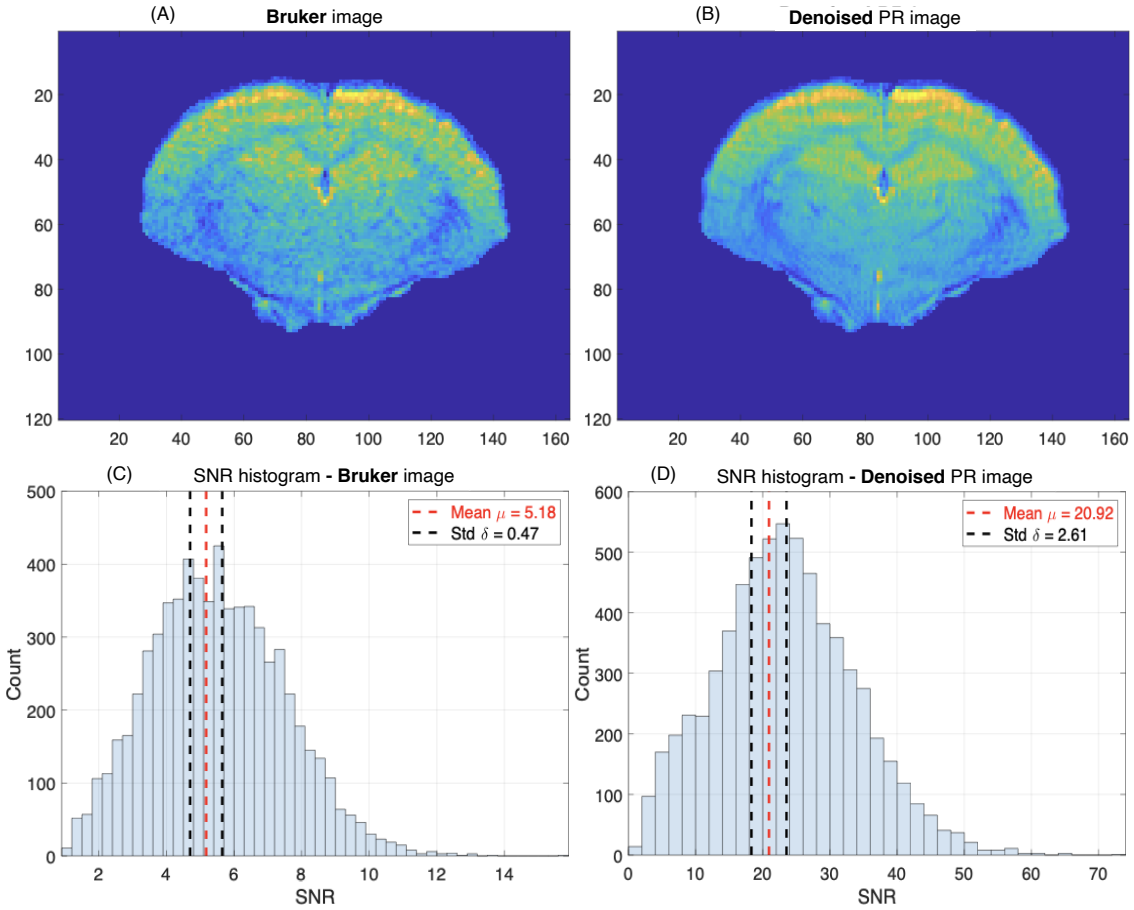

Figure 6.2: Side-by-side comparison between (A) the Bruker image and respective histogram in (C) and (B) the denoised PR image and respective histogram in (D). It's possible to observe the decreased noise level between both images and an increase on the SNR mean level.

Taking a look at the **Residuals** of the denoised image, i.e. the difference between the before and after denoising PR image, we may observe the image only shows noise - Fig. 6.3 (A) - meaning the process of denoising did not introduce new artefacts to the image and is able to efficiently preserve signal. Also, the histogram of the signal magnitude (B) will have a Rician distribution, and both the real and imaginary components in (C) and (D), will have a Gaussian distribution, which resembles what was discussed in 4.1, corroborating that residuals are just composed by noise and no signal.

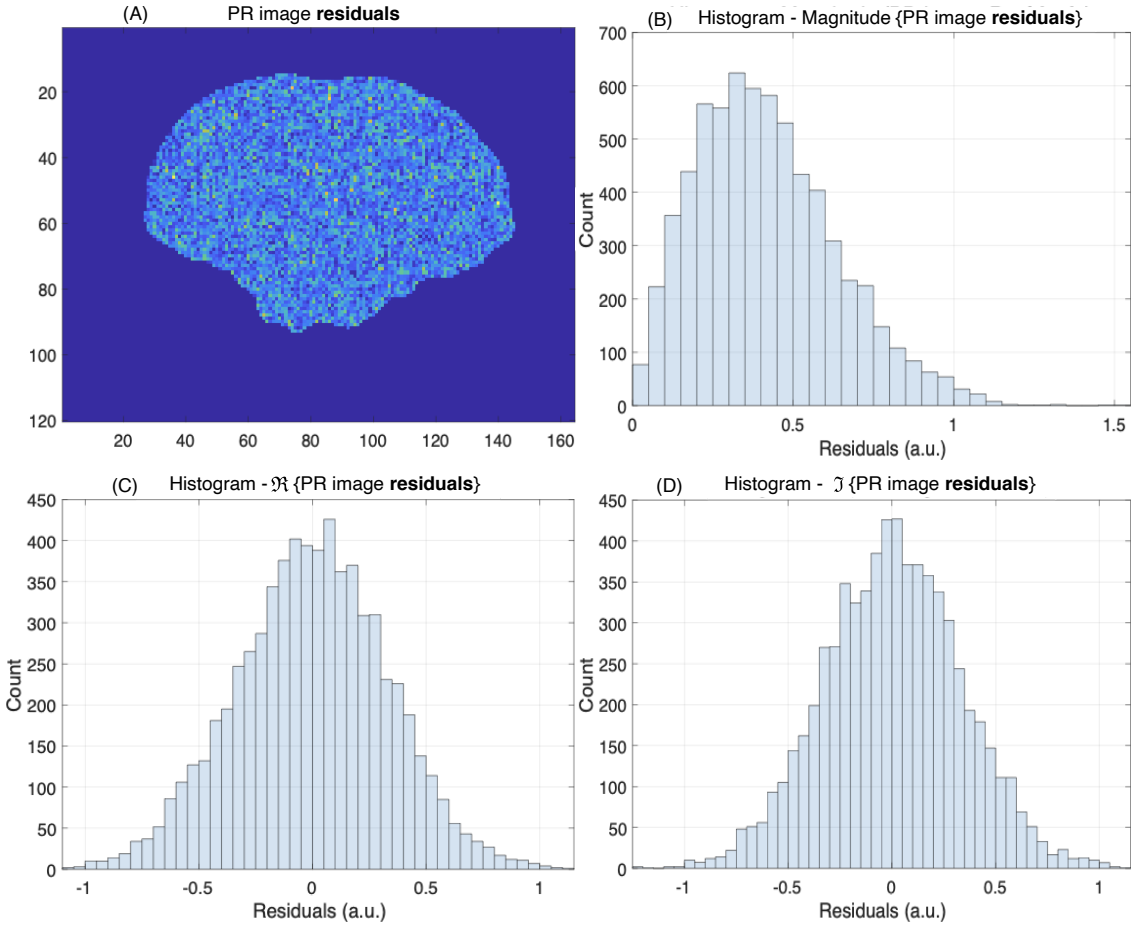

Figure 6.3: (A) Residuals of the PR image residuals along with the respective histogram of its real component (C), imaginary (D) and magnitude (B). The first two have a Gaussian distribution and the latter a Rician distribution, as expected.

Applying **Regridding**, the image will further increase the mean SNR_{Map} from 20.92 ± 2.32 to 22.00 ± 2.53 - Fig. 6.4 (B) and (D), which will result in a final relative increase of 324.71%. SNR_{SV} increases from 69.85 to 74.05, overall increasing to 251.78%.

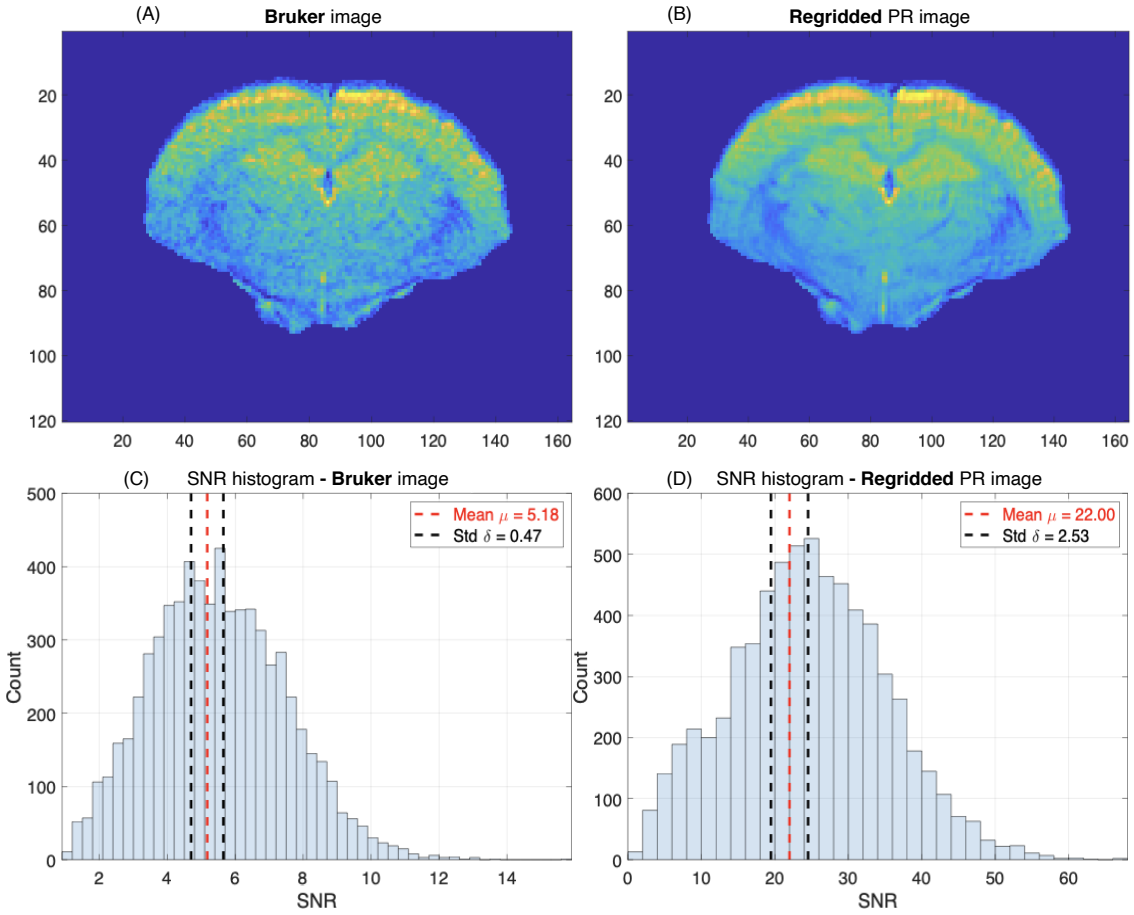

Figure 6.4: Side-by-side comparison between (A) Bruker's image and respective histogram in (C) and (B) the regridded PR image and respective histogram in (D).

Finally, because of what was discussed in section 5.2.6, to remove the noise bias the real component of final image unwrapped is displayed in Fig. 6.5 (B) alongside the final regridded image (A) and respective histograms, with an SNR_{Map} mean increase to 29.81 ± 3.53 and an SNR_{SV} of 75.79. In Table 6.1 it's possible to observe all PR results along the Bruker reconstruction for an easier interpretation.

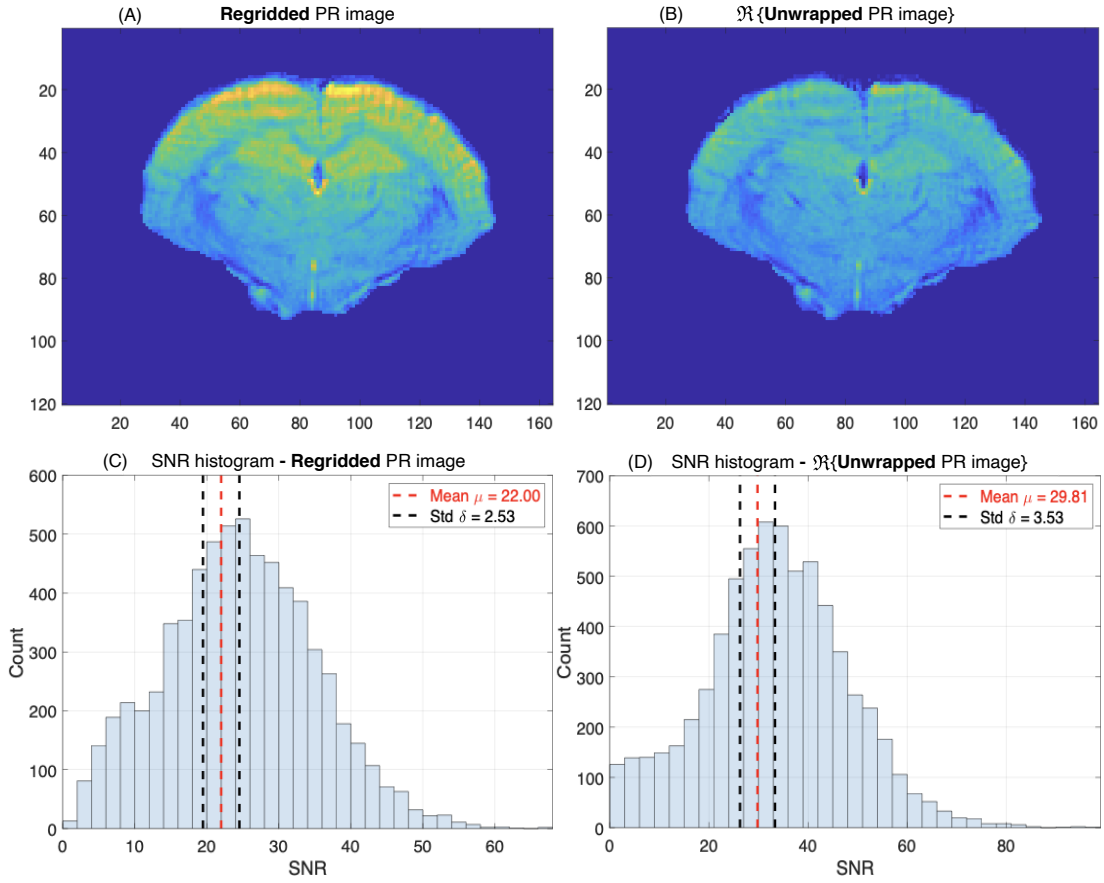

Figure 6.5: In (A) the regridded PR image is shown for comparison, and in (B) the real component of the PR image is shown, due to the noise bias removal, along with respective histograms. It's possible to see an even higher increase in SNR_{Map} mean.

Table 6.1: Summary Table of the SNR values throughout the pipeline with respective Relative Percentual Difference (RPD) of SNR values, all relative to the Bruker standard (darker blue).

	SNR_{Map} mean			SNR_{SV}	
	SNR μ	**Std** σ	**RPD (%)**	**SNR**	**RPD (%)**
Bruker image	5.18	0.47	-	21.05	-
PR image	4.38	0.43	-15.44	16.97	-19.38
Denoised PR image	20.92	2.61	303.86	69.85	231.83
Regridded PR image	22.00	2.53	324.71	74.05	251.78
ℜ{**Unwrapped** PR image}	29.81	3.53	475.48	75.79	260.05

6.1.2 Denoising k-space vs image-space

As discussed in section 5.2.4, when the MP-PCA is applied, it is possible to denoise either the image-space directly or k-space. Typically, it would make sense for Denoising to be performed on the image domain directly using voxels along the redundant dimension to construct the MP distribution and only then can the noise eigenvalues be effectively removed. Herewith, a hypothesis can be stated that one approach may be better than the other.

In Fig. 6.6 (A) denoising was performed using the **image-space** with its respective SNR histogram in (C) with an SNR_{Map} average of 14.22 ± 1.68 and an SNR_{SV} of 40.45. The Residuals map, obtained the same way as previously explained, can be observed in Fig. 6.6 (B) with the respective histogram (D) - only the real component is shown for space-wise purposes - and the same conclusion can be reached: the process of denoising here not only didn't introduce new artefacts to the image but also is able to efficiently preserve signal.

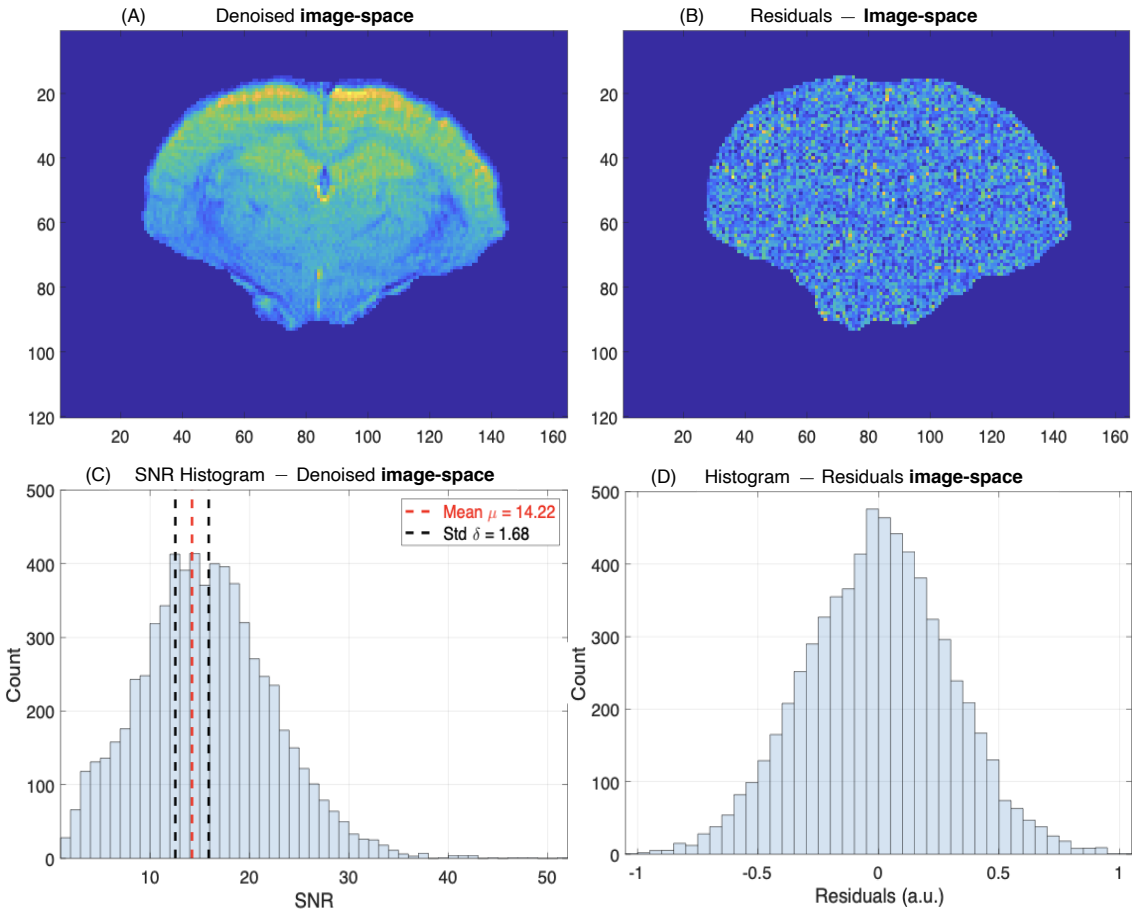

Figure 6.6: (A) Image-space denoising was performed with its respective SNR histogram (C) along its residuals (B) and histogram distribution (D). For space-wise purposes, only the real component is shown, but the other components have a similar distribution to Fig. 6.3 (B) and (D).

Considering data used in the previous section was obtained with k-space denoising, a **comparison between the two** can be attained. Fig. 6.7 shows the denoised **image-space** (A) and the denoised **k-space** (B) side-by-side with their corresponding histograms with mean SNR map of 14.22 ± 1.68 (C) and 20.90 ± 2.61 (D), respectively.

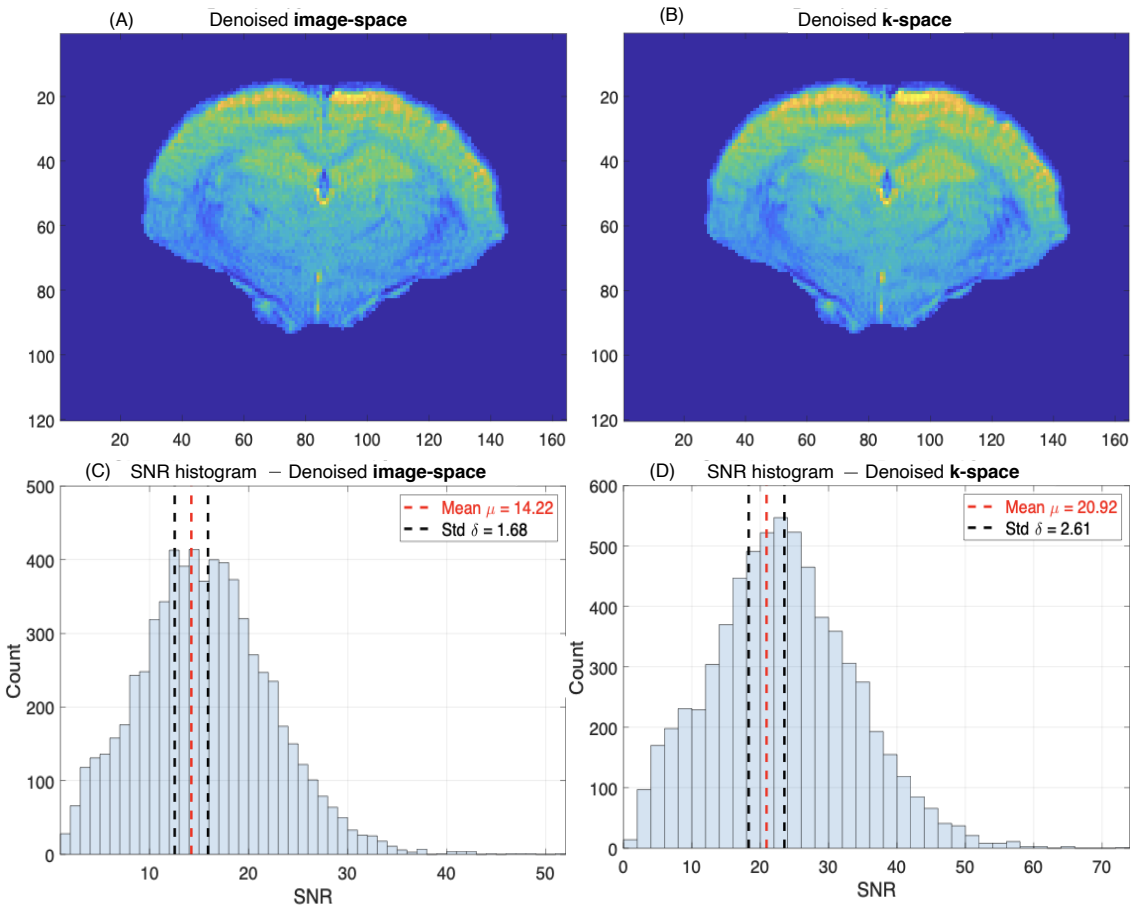

Figure 6.7: (A) Denoised image-space along with its respective histogram (C). (B) Denoised k-space along with respective histogram distribution (D).

Comparing both approaches of Denoising, Fig. 6.8 shows the EPI converted data before denoising, here named **original** (A), after the more conventional **image-space** denoising (B) and after **k-space** denoising (C). It is important to note that data quality has a significant, more smooth SNR improvement for both denoising strategies and that both Residuals and corresponding histograms - shown below in (D) and (E) - are very similar, with no presence of something that resembles signal and their distribution is Gaussian-like, implicating very signal variance is removed.

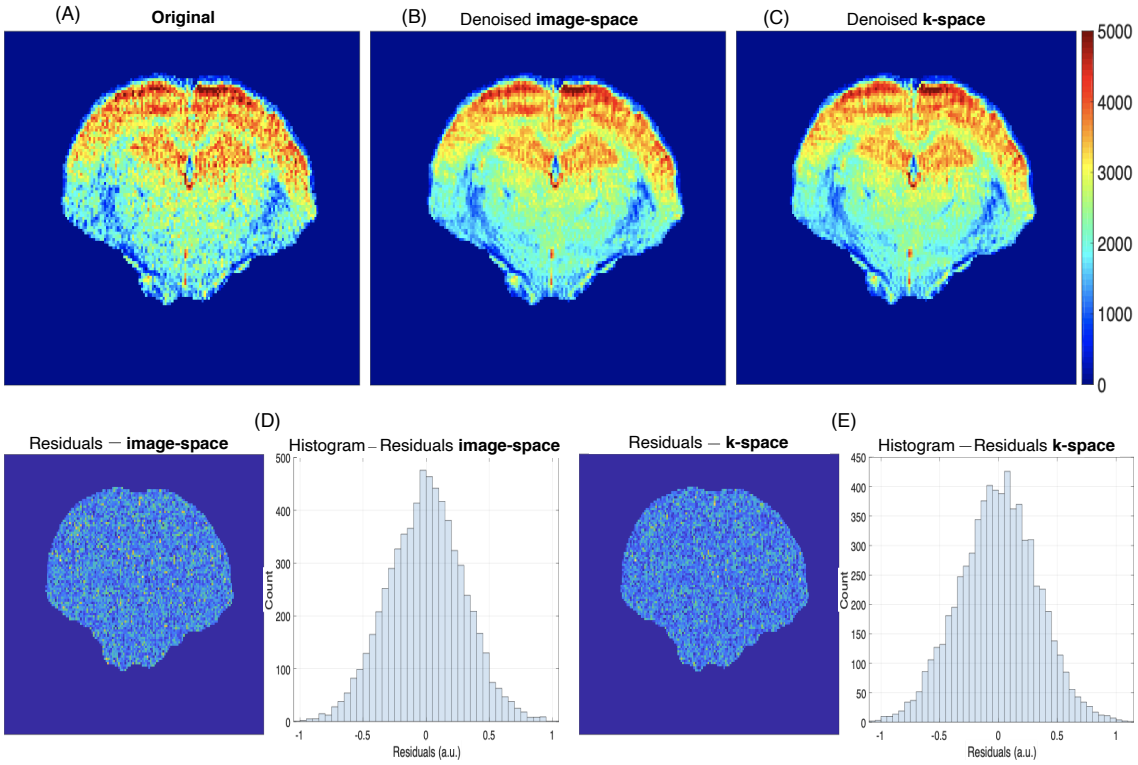

Figure 6.8: (A) Image before denoising - Original - (B) after image-space denoising and (C) after k-space denoising. The residuals and histogram distribution from (B) and (C) are shown in (D) and (E), respectively. For space-wise purposes, only the residuals real component is shown, but the other components have a similar noise behaviour distribution. The colormap of (C) is the same for all three pictures. All denoising parameters were identical except the domain in which denoising was performed.

Figure 6.9 shows the quantitative SNR maps for the 3 cases: (A) **original**, (B) after **image-space** denoising and (C) after **k-space** denoising. The original image has a signal ratio range from 0 to 8, the image-space denoising has a range between 10 to 20 while the k-space denoised image has a more predominant higher range of 18 to 25.

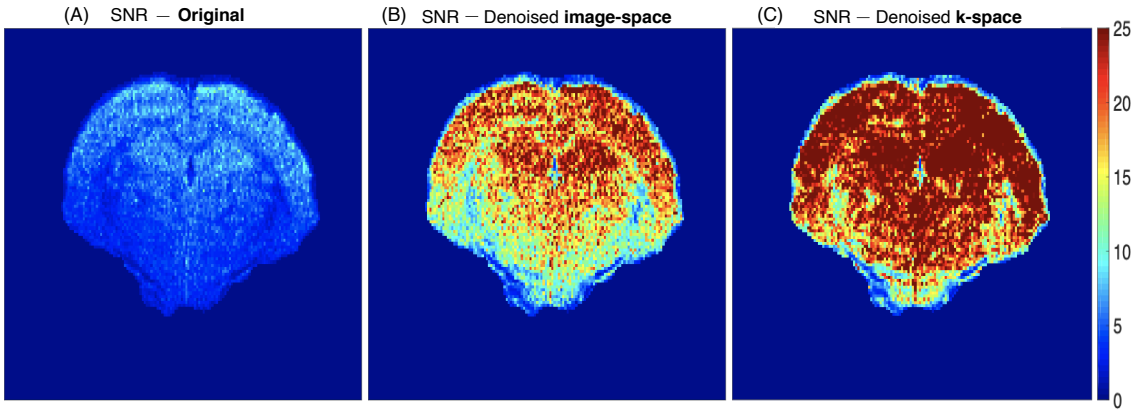

Figure 6.9: SNR quantitative maps for the 3 cases: (A) Original before denoising, (B) after Image-space denoising and (C) after k-space denoising. The colourmap of (C) is the same for all three pictures. All denoising parameters were identical except the domain in which denoising was performed.

Finally, Fig. 6.10 shows the **SNR histogram for all three stipulated cases** along with each SNR mean, 5.03 for the original image, 14.22 for the denoised image-space and 20.90 for the denoised k-space. All results can be seen in Table 6.2 for an easier analysis.

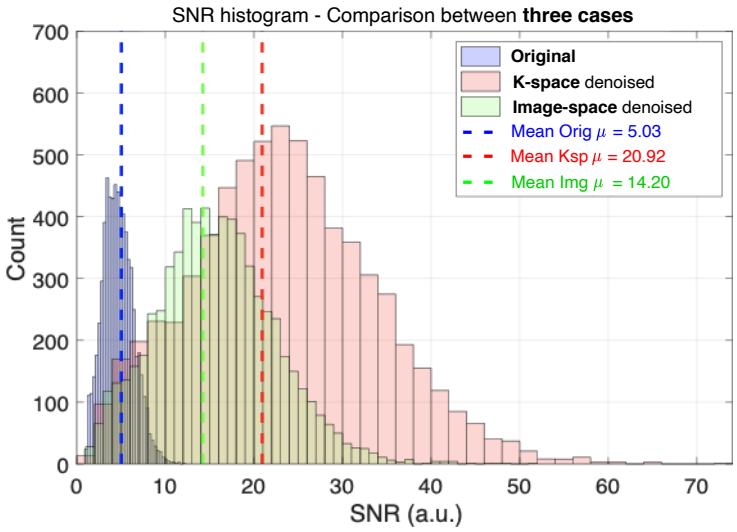

Figure 6.10: SNR histogram comparison between the 3 cases: Original (Orig), after Image-space (Img) denoising and after k-space denoising (Ksp) along with their means in coloured dashed lines corresponding to each case. All denoising parameters were identical except the domain in which denoising was performed.

Table 6.2: Summary Table of the SNR values comparison of Image-space and k-space with respective Relative Percentual Difference (RPD).

	SNR_{Map} mean			SNR_{SV}	
	SNR μ	**Std σ**	**RPD (%)**	**SNR**	**RPD (%)**
Denoised **image-space**	14.22	1.68	47.12	40.45	72.68
Denoised **k-space**	20.92	2.61		69.85	

6.1.3 Denoising window

Finally, because of the Denoising uncertainty and variables associated, the **denoising window size** was also studied to check whether the ideal window size $\sqrt{\text{No. of Repetitions}}$ has the highest SNR value or if a better value can be found.

Fig. 6.11 shows a plot of the denoising SNR level vs Window Size at 3 stages in the pipeline: After Denoising (AD), After Regridding (AR) and the real component After Unwrapping. In (A) the mean map variation is shown, while in (B) the more representative SNR parameter SNR_{SV} can be observed, and in both it's notorious the Regridding increase of SNR level along with an even higher real component, without noise bias.

Of notice that there seems to be two local maximums, being the first located around the ideal denoising window expressed by [62] in 17, however a higher SNR is possible to achieve with a Window Size of 48, going from 18.1 to 21.92, an increase of 21.10%.

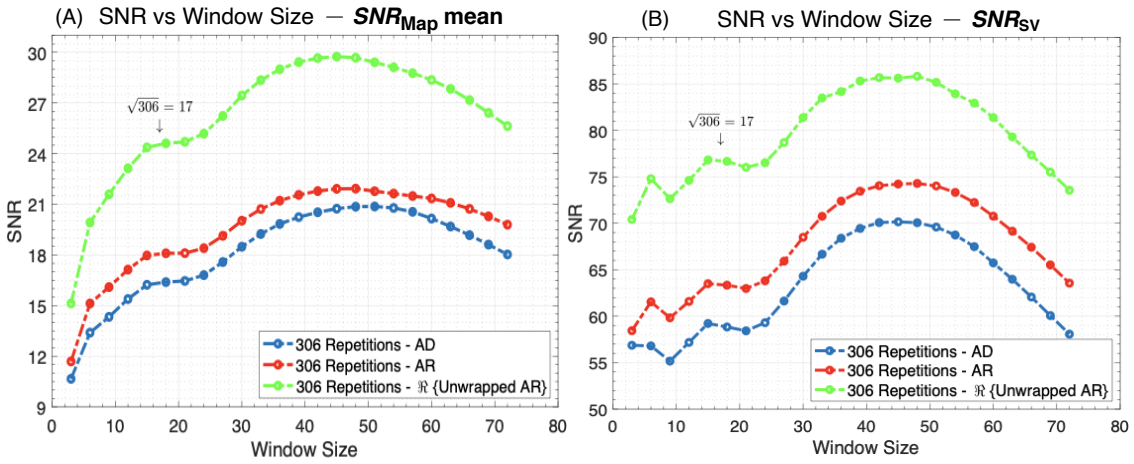

Figure 6.11: Plot of the SNR vs denoising Window Size at 3 different pipeline stages: After Denoising (AD), After Regridding (AR) and the real component of the Unwrapped Image with: (A) the parameter SNR_{Map} and (B) SNR_{SV}. All denoising parameters were identical except the Window Size with which Denoising was performed.

6.2 Experimental Data - Multichannel

Denoising in a **Multichannel** dataset introduces a new variable until now unaccounted for: coils/channels and how should they be denoised. Three possible scenarios were hypothesised to understand where the algorithm would be more effective: coil combine after ghost correction and denoise like it is one image (CC Beginning); individually denoise each coil and combine afterwards (Individual CC); and have all the coils collapse to the same dimension, creating a "Super Coil" N times bigger, if N coils were used (Super Coil). Tests were performed with both SNR parameters - Fig. 6.12 - and although the SNR_{Map} parameter (A) shows that CC Beginning is the worst scenario, it is only by 0.5 while in (B) the truer SNR_{SV} shows that scenario was at least twice as high as the others, so the chosen scenario was the former: **coil combine right after ghost correction and denoised like the Single Coil case**.

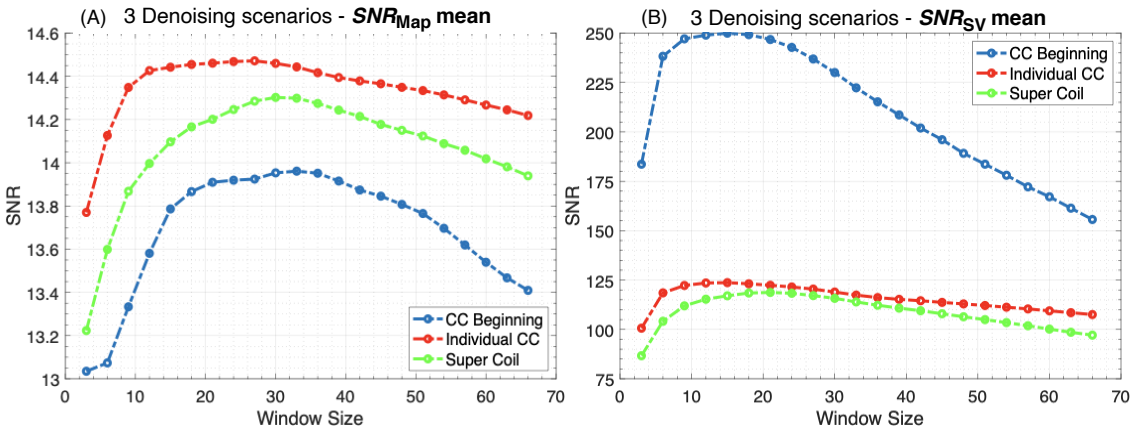

Figure 6.12: Plot of the SNR vs Denoising Window Size at 3 different Denoising scenarios: denoising after Coil Combination at the Beginning (CC Beginning), Individual denoise each Coil (Individual CC) and denoise the "Super Coil" (Super Coil) with: (A) the parameter SNR_{Map} and (B) SNR_{SV}. All denoising parameters were identical except the Window Size with which Denoising was performed.

In this case, the section "*Comparison between the vendor image and the denoised image*" used k-space after Coil Combination with a Window Size of 30, section "*Denoising k-space vs image-space*" compares both denoising options and "*Denoising window*" highlights how SNR behaves according to the window size.

Since this dataset is a diffusion EPI, all 92 images with the b=0 s/mm^2 value were used to calculate the mean of SNR parameters - b being a factor that indicates how strong the MRI diffusion is.

6.2.1 Comparison between the vendor image and the denoised image

Fig. 6.13 (A) shows the Bruker's image and the PR image in (B) with the respective histograms. The images aren't the same size due to the sampling compensation explained in section 5.3, thus the masks and image size will only be the same at the last step, and only then a comparison between the two is viable. Until there the comparison is performed **between PR images**.

Apart from the noticeable ringing effect, due to the EPI trajectory and only corrected at a later stage in Regridding, both images are visually similar - SNR_{Map} means are 9.08 ± 0.88 and 8.28 ± 0.99, meaning the PR is almost at the same point of image reconstruction as the scanner's manufacturer. Using the SNR_{SV} a value of 103.49 is obtained for Bruker and 46.20 for PR - a difference explained by a different 20 × 20 Noise ROI, since using the previously established ROI won't have only noise, one of the requirements for the ROI_{Noise}.

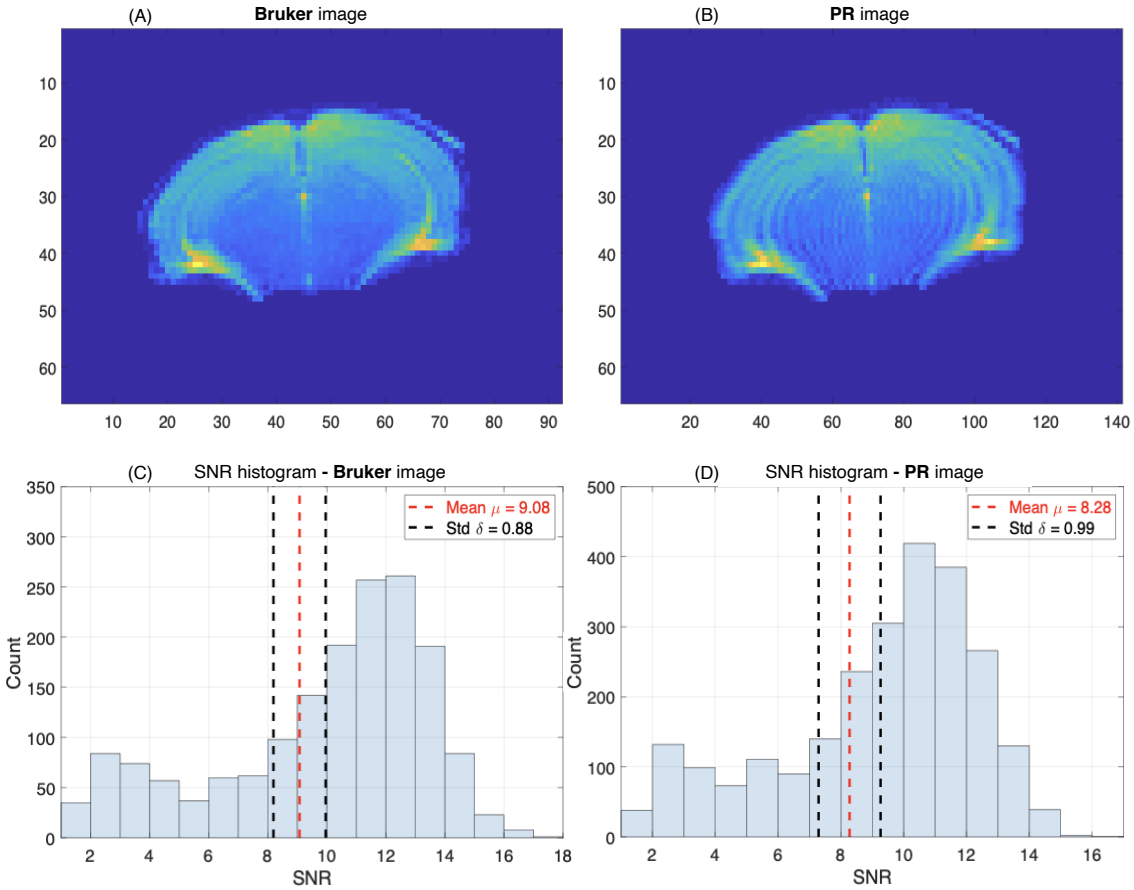

Figure 6.13: Side-by-side comparison of (A) Bruker's image and respective histogram (C) and in (B) the PR image and respective histogram in (D). Apart from the ringing, corrected at a later stage, it's possible to see the similarity between images.

After **Denoising**, the resulting PR image is displayed in Fig. 6.14 (B) with the respective histogram in (D). Again the Bruker image and its SNR distribution is displayed for an easier visual comparison. SNR value increases from 8.28 ± 0.99 up to 9.54 ± 0.82, corresponding to a relative increase of 15.22%. In SNR_{SV} the value will be 155.29, increasing 236.13%.

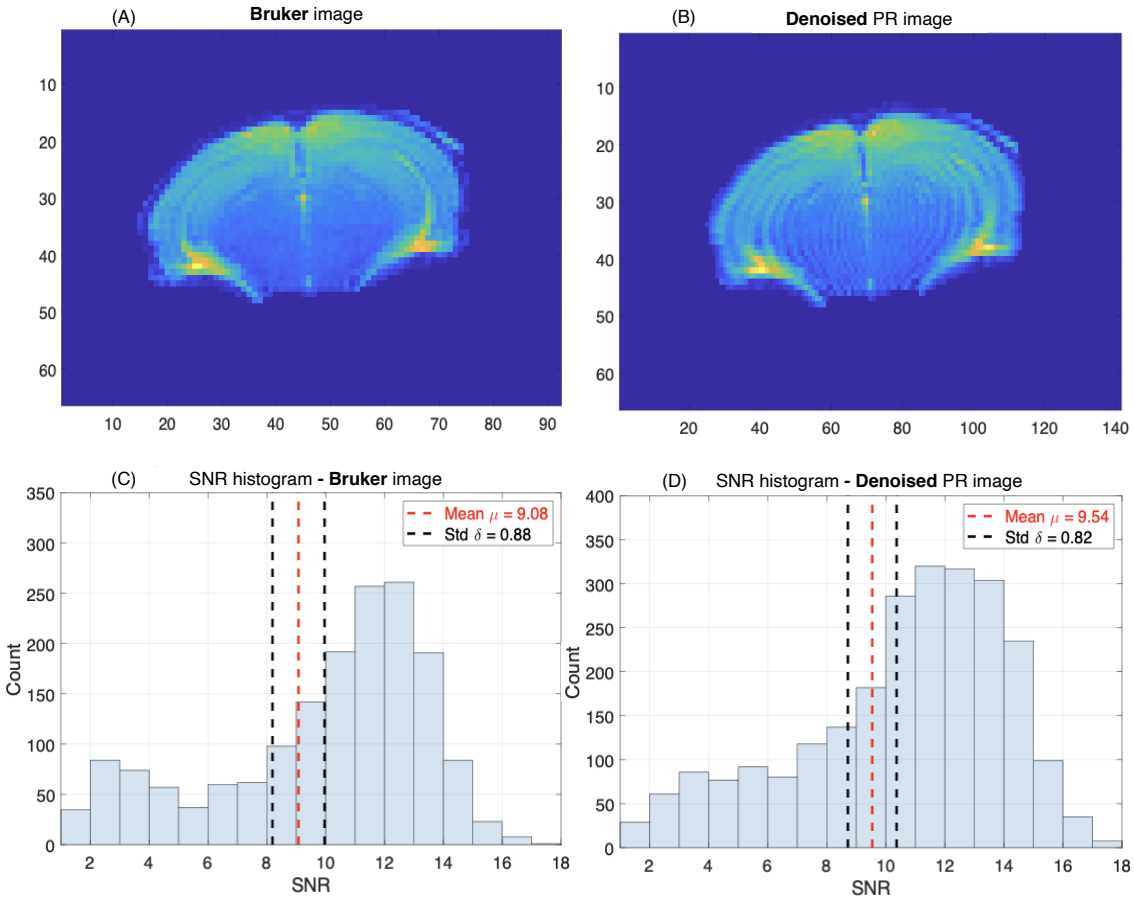

Figure 6.14: Side-by-side comparison between (A) Bruker's image and respective histogram in (C) and (B) the PR image after denoising (AD) and respective histogram in (D).

Using the denoised **image Residuals map** - Fig. 6.15 (A) - and the real data distribution (B), it is possible to confirm only the presence of noise and little to non-existent signal, which implies there was good signal preservation and no introduction of artefacts. As the Weighted Coil Combination Method used the data magnitude to combine coils - eq. (5.1) - it only makes sense to calculate the real data component histogram.

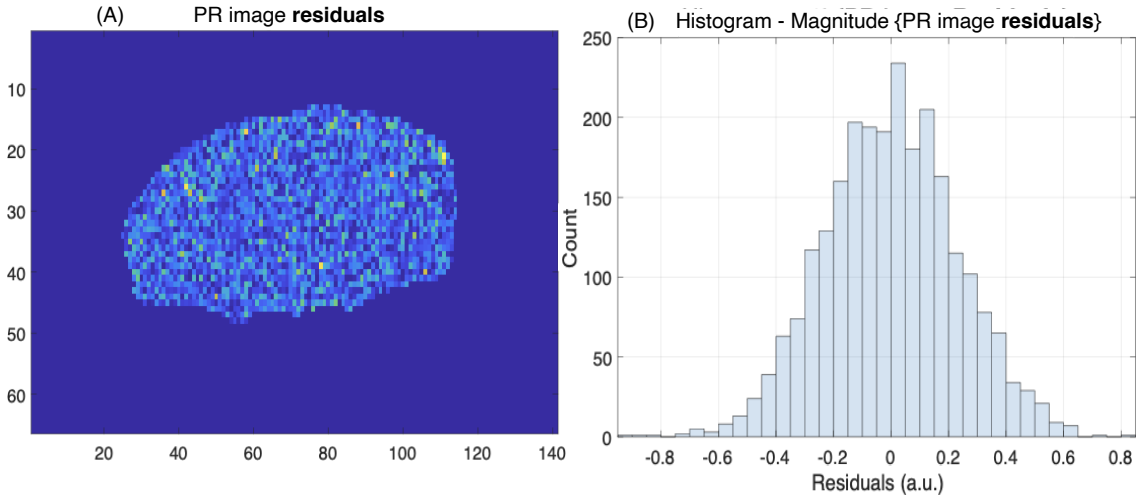

Figure 6.15: (A) Residuals of the PR along with the histogram of its real component (B), the latter having a Gaussian distribution, as expected. Since the coil combination uses the magnitude of the data to combine coils, it's only possible to calculate the magnitude histogram.

After applying **Regridding**, the ringing effect of the image is completely removed - can be observed in Fig. 6.16 (B). Nonetheless - data not shown - before cropping the image, the SNR level reduces to 9.12 ± 0.66, which will result in a final relative increase of 10.14%. Although the SNR_{Map} mean reduces, the more reliable SNR_{SV} level increases from 155.29 to 176.27, with a final relative increase of 281.54%, indicating the image has an overall quality increase.

After the *compensation correction*, and both unwrapping and taking the real component, the Fig. 6.16 (B) is obtained, while in (A) Bruker's image is displayed for comparison with respective histograms. Here SNR_{Map} means are 9.08 ± 0.88 and 13.95 ± 0.82, while the SNR_{SV} is 103.49 and 230.05, representing a final increase of 53.63% and 122.29% respectively.

At this point and because a crop had to be made to match Bruker's dimensions, a **scaling factor** may be a key factor in image reduction, however we need further evidence to check the benefits of denoising. It was not the scope of the investigation to deduce this factor. Noteworthy the ROI for the noise in the cropped images was a 20 × 20 rectangle, instead of the usual 27 × 27, explaining the increased SNR_{SV}. Also, in Fig. 6.16 (B) the real component of the unwrapped image won't have a different visual look contrasting with the Single Case - Fig. 6.5 (B) - because of the way coils were combined.

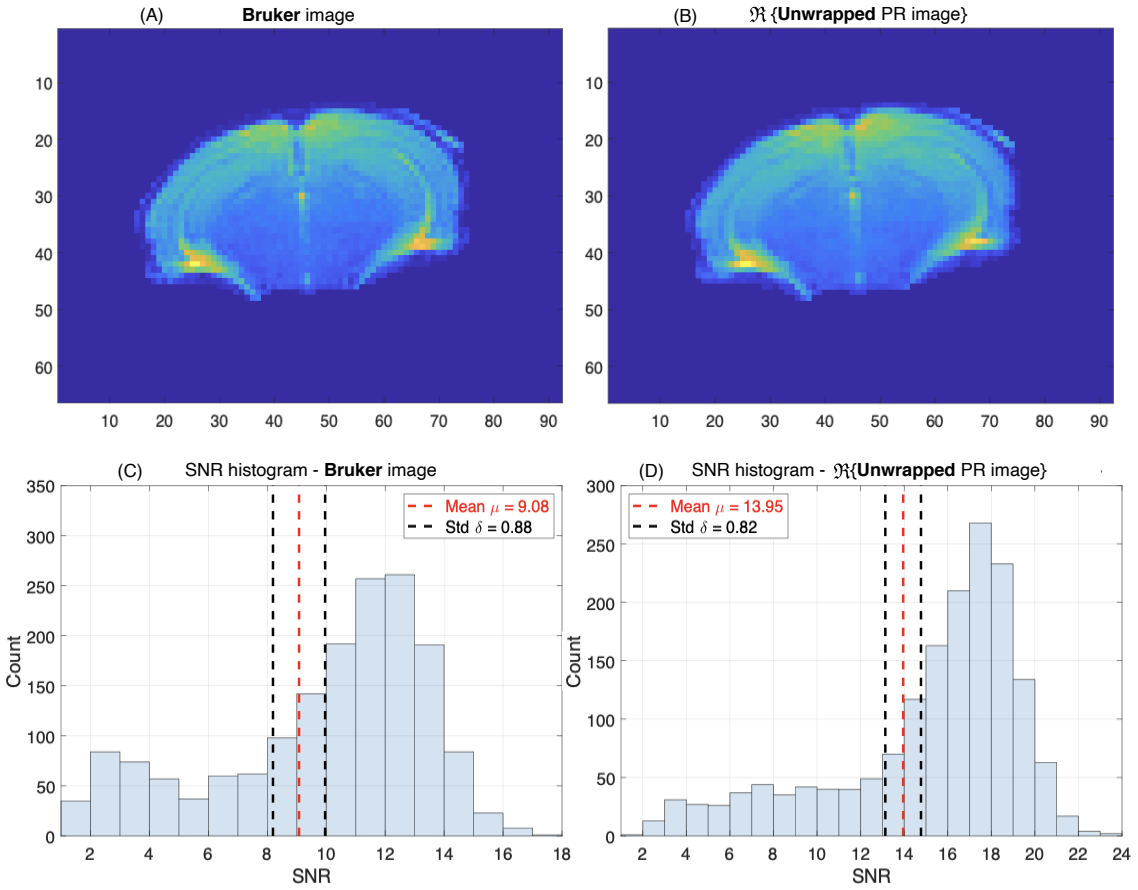

Figure 6.16: Side-by-side comparison between (A) Bruker's image and respective histogram in (C). In (B) the real component of the unwrapped PR image is displayed with the respective histogram in (D).

Finally, to demonstrate Denoising can also have a **more visual impact** in multichannel images, a higher value b image is shown in Fig. 6.17. Here it is possible to see for comparison the Bruker version (A) and the final unwrapped PR image real component (B) with respective histograms. The former has a mean SNR map of 1.86 ± 0.09 and the latter 3.53 ± 0.80, corresponding to a relative increase of 89.79%. The SNR_{SV} has a value of 29.11 and 58.48, respectively, with an increase of 100.89%. In Table 6.3 all results for both b values can be examined for an easier analysis.

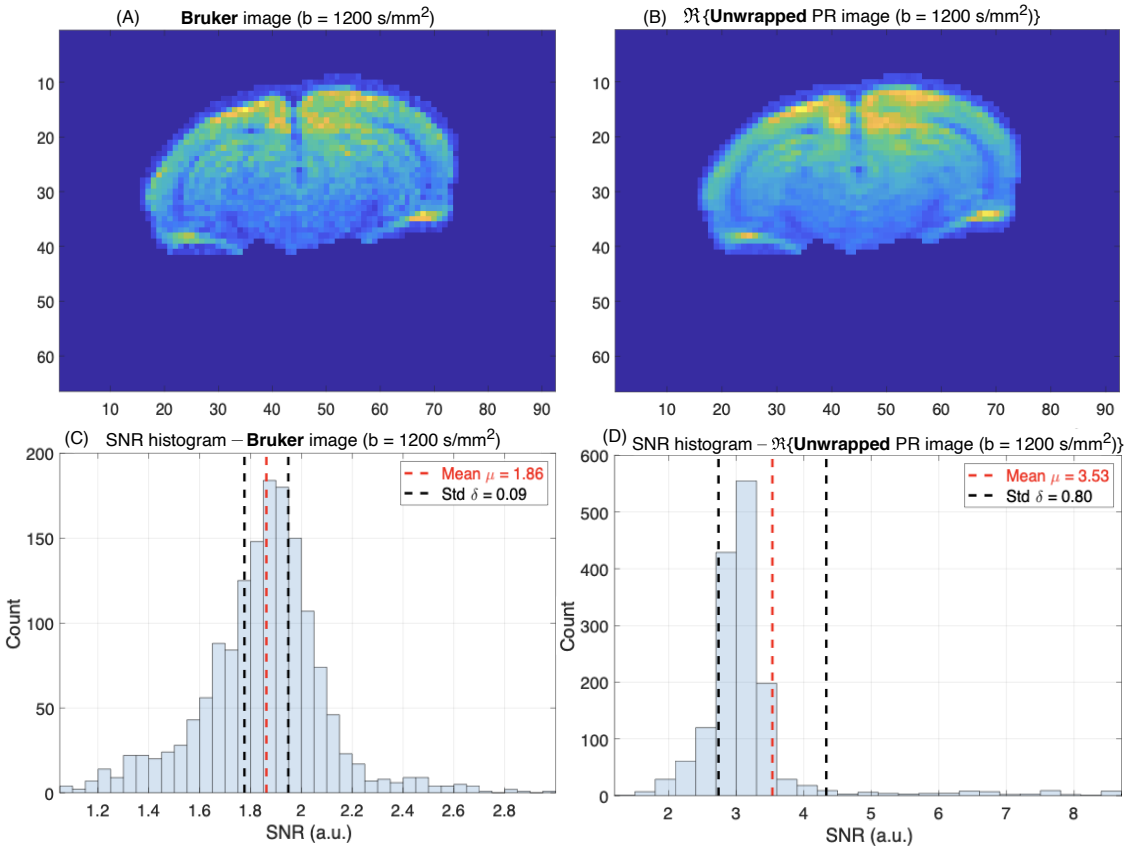

Figure 6.17: Bruker image (A) and the real component of the unwrapped PR image (B) with respective histograms with b = 1200 s/mm^2. The Denoising effect is more pronounced and visible at a higher b value.

Table 6.3: (i) For b = 0 s/mm^2, the Summary Table of the SNR values throughout the pipeline with respective Relative Percentual Difference (RPD) of SNR values is displayed. (ii) For b = 1200 s/mm^2, the Summary Table of the SNR values with respective Relative Percentual Difference (RPD) of SNR values is displayed.
In $^{(a)}$ the RPD is relative to the PR image due to the size difference, and in $^{(b)}$ is relative to respective Bruker standard (darker blue).

	$SNR_{\mathbf{Map}}$ **mean**			$SNR_{\mathbf{SV}}$	
(i)	**SNR** μ	**Std** σ	**RPD (%)**	**SNR**	**RPD (%)**
Bruker image	9.08	0.88	-	103.49	-
PR image	8.28	0.99	-	46.20	-
Denoised PR image	9.54	0.82	15.22$^{(a)}$	155.29	236.13$^{(a)}$
Regridded PR image	9.12	0.66	10.14$^{(a)}$	176.27	281.54$^{(a)}$
$\Re\mathfrak{e}${**Unwrapped** PR image}	13.95	0.82	53.63$^{(b)}$	230.05	122.29$^{(b)}$
(ii)					
Bruker image	1.86	0.09	-	29.11	-
Denoised PR image	3.53	0.80	89.79$^{(b)}$	58.48	100.89$^{(b)}$

$^{(a)}$relative to **PR** image

$^{(b)}$relative to respective **Bruker** image

6.2.2 Denoising k-space vs image-space

Making now the same analysis of **image-space** and **k-space** denoising, the same hypothesis was stated that one approach may provide a better SNR level than the other.

In Fig. 6.18 (A) **image-space** denoising is shown along its SNR histogram in (C) with an SNR level of 9.92 ± 0.77 and an SNR_{SV} of 208.95. The Residuals map is shown in Fig. 6.18 (B) with its distribution in (D) - only the real image can be calculated - and also no high signal is present in the image, being signal correctly preserved.

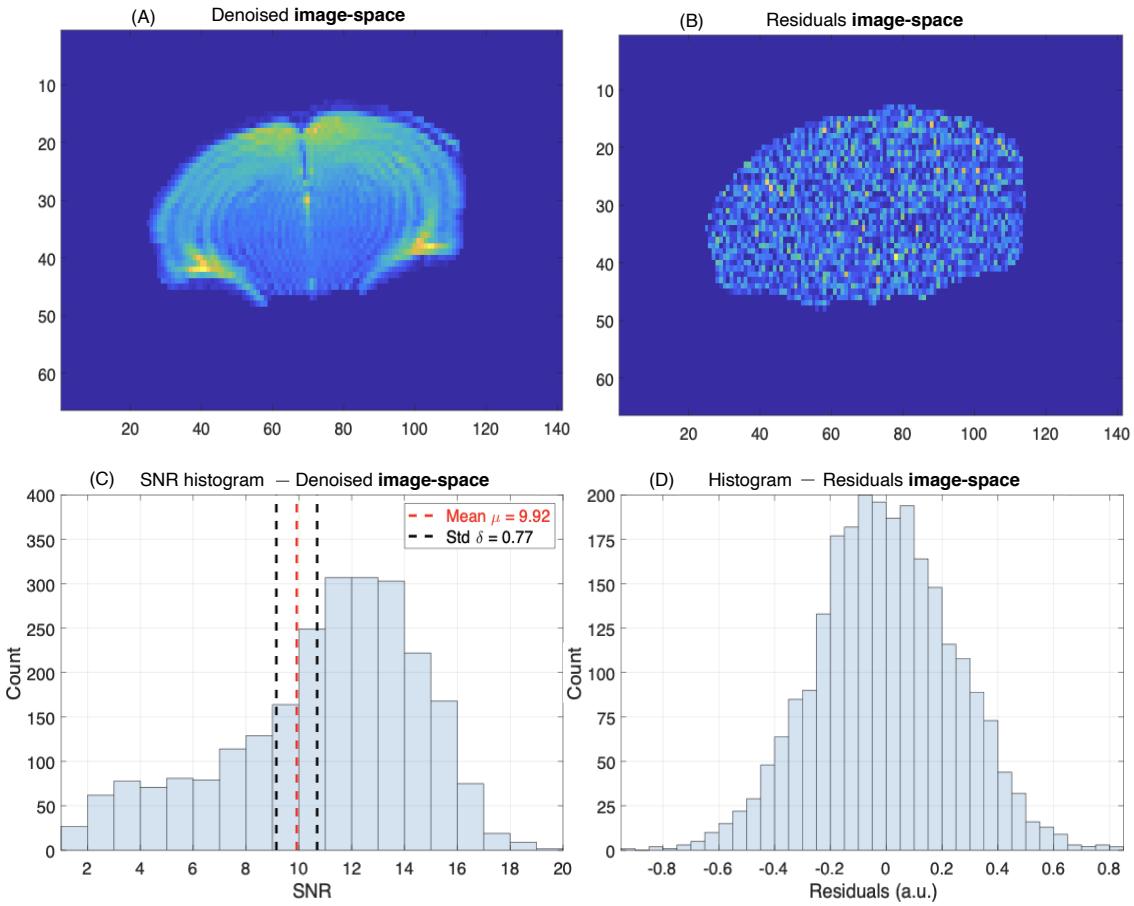

Figure 6.18: (A) Image-space denoising was performed with its respective histogram (C) along with its Residuals (B) and histogram distribution (D). As expected it has a Gaussian distribution, and is also the only dispersion that is possible to calculate due to coil combination.

Since data in the previous section was obtained with k-space denoising, the **two can be compared**. Fig. 6.19 shows the denoised **image-space** (A) and the denoised **k-space** (B) side-by-side with their corresponding histograms with a mean SNR of 9.92 ± 0.77 (C) and 9.54 ± 0.82, respectively.

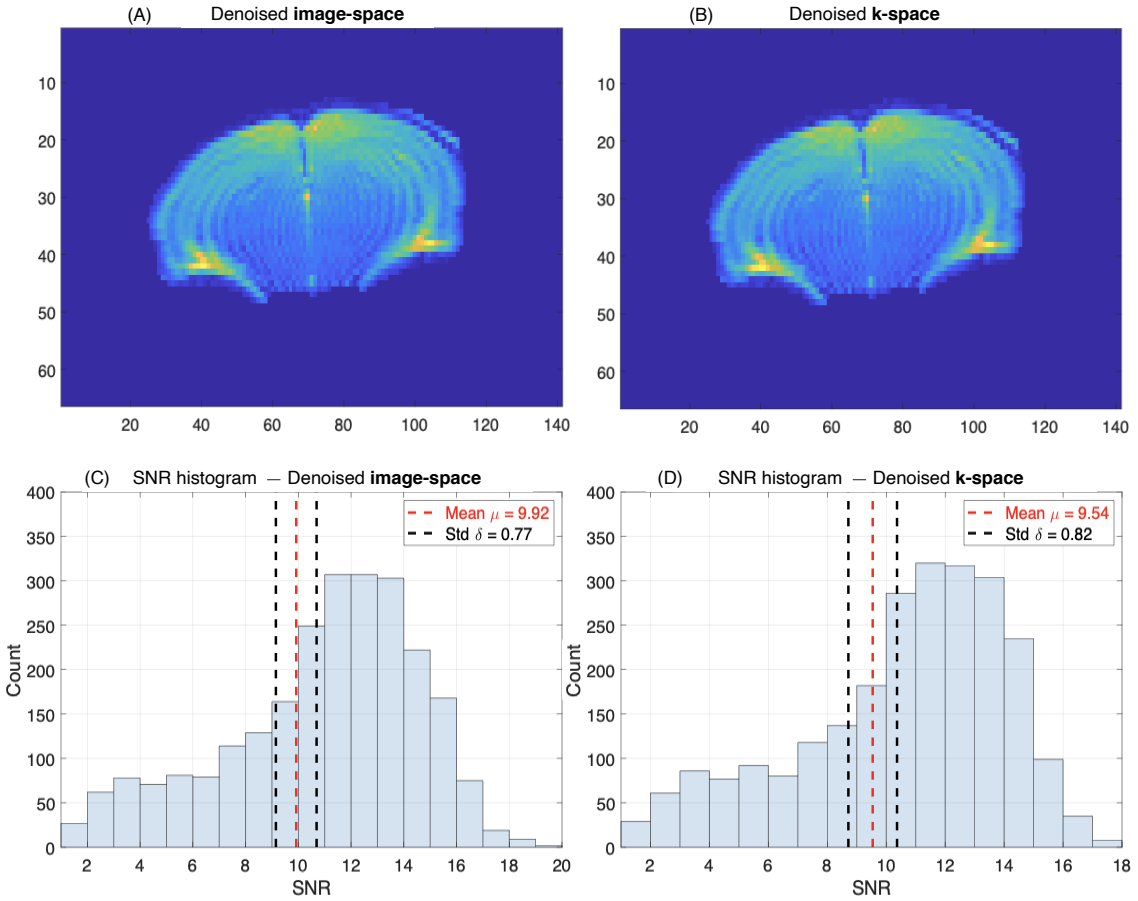

Figure 6.19: (A) Denoised image-space along with its respective histogram (C). (B) Denoised k-space along with respective histogram distribution (D).

Comparing both methods of Denoising for this case, Fig. 6.20 (A) shows the **original** image before denoising, (B) after **image-space** denoising and (C) after **k-space** denoising which are all quite similar. Residuals and corresponding histograms are shown below in (D) and (E), which are also very similar, with no presence of residuals and their distribution looks Gaussian-like, implicating very signal variance is removed.

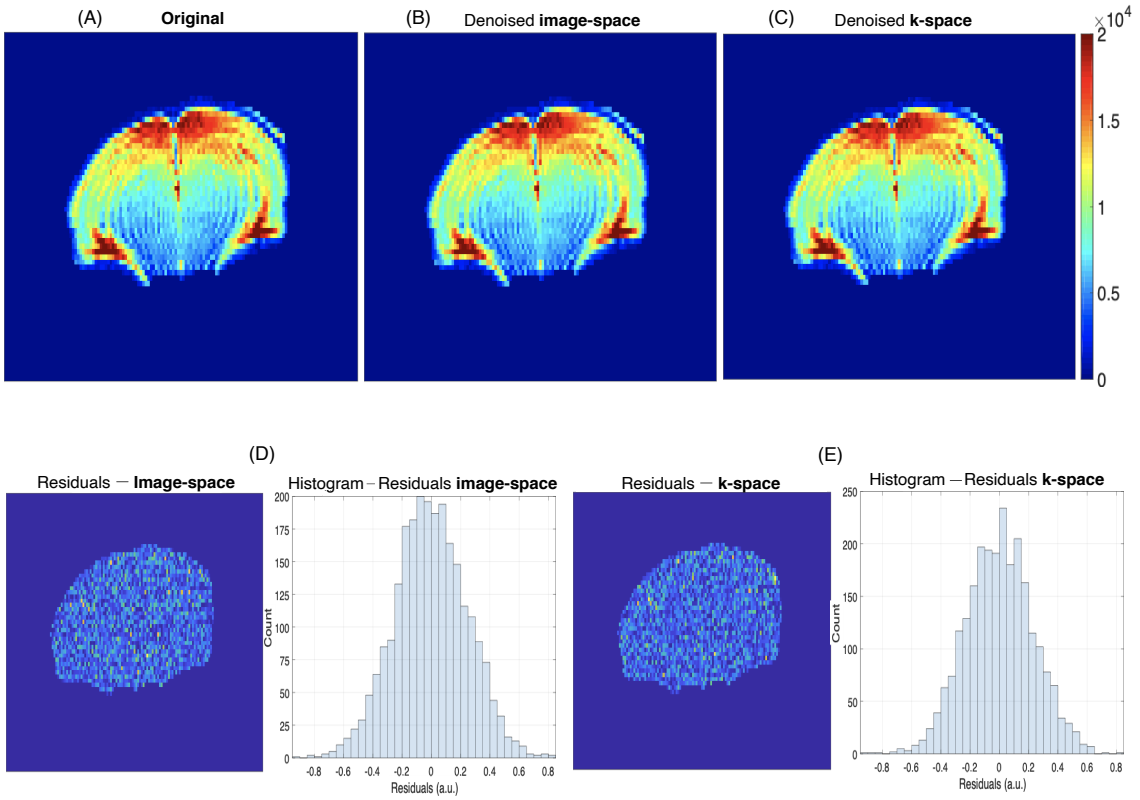

Figure 6.20: (A) Image before denoising, after image-space denoising (B) and after k-space denoising (C). The Residuals from (B) and (C) and histogram distribution are shown in (D) and (E), respectively, all having a Gaussian distribution. The colourmap of (C) is the same for all three pictures. All denoising parameters were identical except the domain in which Denoising was performed.

Figure 6.21 shows the quantitative SNR maps for the 3 cases: **original**, after **image-space** denoising and after **k-space** denoising. The original image has a signal ratio range from 5 to 12, and both image-space and k-space denoising have a predominant SNR range of 12 to 15.

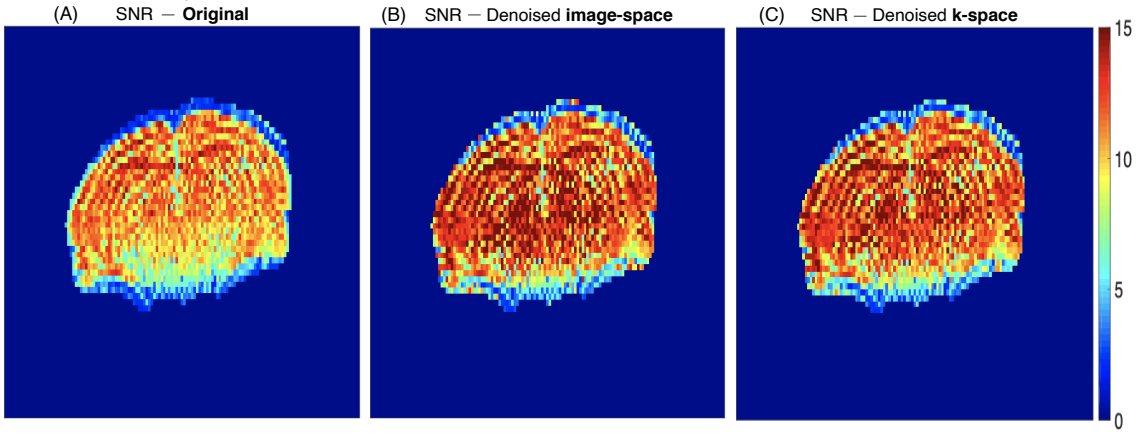

Figure 6.21: SNR quantitative maps for the three cases: (A) Original before denoising, (B) after image-space denoising and (C) after k-space denoising. The colourmap of (C) is the same for all three pictures. All denoising parameters were identical except the domain in which Denoising was performed.

Finally, Fig. 6.22 shows the **SNR histogram with the superposition of all three stipulated cases**, along with each SNR mean: 8.28 for the original image, 9.92 for the denoised image-space and 9.54 for the denoised k-space. In Table 6.4 all results for the k-space and image-space denoising can be observed for an easier analysis.

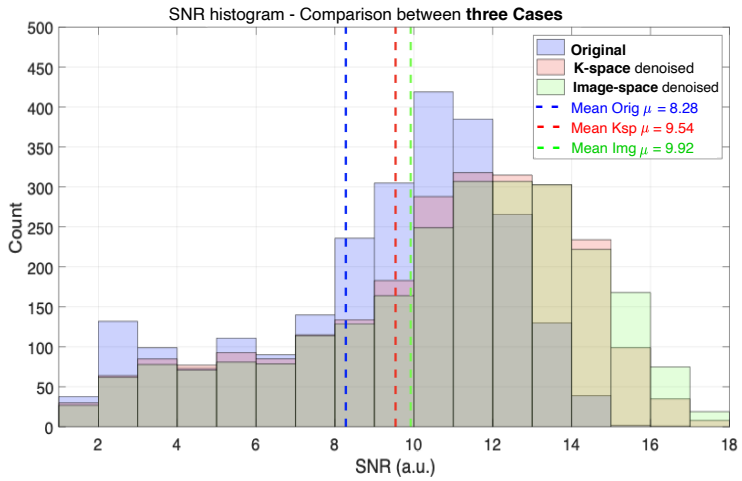

Figure 6.22: SNR Histogram comparison between the three cases: Original (Orig), after Image-space (Img) denoising and after k-space denoising (Ksp) along with their means in colored dashed lines corresponding to each color case. All denoising parameters were identical except the domain in which Denoising was performed.

Table 6.4: Summary Table of the SNR values Comparison of Image-space and k-space with respective Relative Percentual Difference (RPD).

	SNR_{Map} mean			SNR_{SV}	
	SNR μ	**Std σ**	**RPD (%)**	**SNR**	**RPD (%)**
Denoised **image-space**	9.92	0.77	3.83	208.95	25.68
Denoised **k-space**	9.54	0.82		155.29	

6.2.3 Denoising window

Lastly, the denoising Window Size was plotted with the corresponding SNR to check the ideal window size $\sqrt{\text{No. of Repetitions}}$ trustability.

Fig. 6.23 (A) shows the plot of the denoising Window Size with the corresponding SNR map mean at 2 stages in the pipeline: After Denoising (AD) and After Regridding (AR). In Fig. 6.23 (B) it's possible to see the same plot but for the SNR_{SV} version at the same 2 stages. Only the same size images are viable to compare, hence the 2-stage comparison instead of the previous 3-stage case.

Though the ringing effect removal, opposite of what happened in the single case, in (A) it's visible the decrease in SNR_{Map} mean with Regridding, however in (B) the more representative SNR_{SV} parameter increases with this step, which is in line with what was previously discussed.

No two local maximums are reported in multichannel denoising, being the ideal denoising window expressed by [62] approximately well located on the highest SNR in (A), but is a bit overestimated in (B).

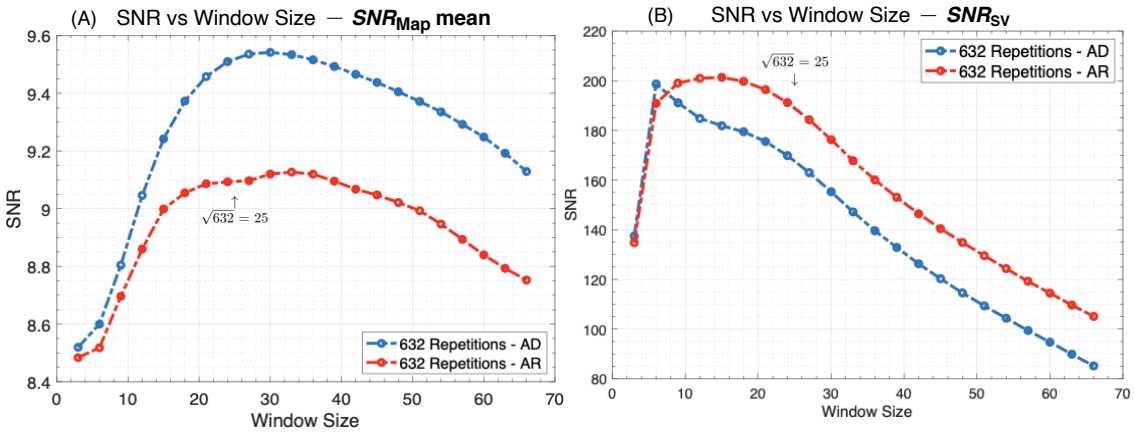

Figure 6.23: Plot of the SNR vs denoising Window Size at 2 different pipeline stages: After Denoising (AD) and After Regridding (AR) with: (A) the parameter SNR_{Map} and (B) SNR_{SV}. All denoising parameters were identical except the Window Size with which Denoising was performed.

7

Discussion

The main focus of this work was to characterise the performance of MP-PCA under different conditions and to develop more optimal ways of denoising data. Below, we discuss the main features found in our work as well as future perspectives.

7.1 Single Channel Reconstruction

7.1.1 Comparison between the vendor image and the denoised image

Although the current dilemma in finding common ground on SNR calculation due to its many variables and different situations, the results obtained for both single and multi-channel allow conclusions to be drawn from the data here presented.

First, it is worth pointing that the PR here developed produced images that were identical or close to identical to the vendor's reconstruction. This suggests that all steps along the pipeline were correctly implemented and executed.

After successfully achieving the same image as the scanner manufacturer's makes available, the MP-PCA Denoising was used to successfully separate noise and signal eigenvalues, which significantly improved image quality, allowing images to be interpreted in a better way while improving overall signal - Fig. 6.2 (A) and (B) - but also significantly increases SNR - Fig. 6.2 (C) and (D). There is still a relative increase of 303.86%., 5.18 to 20.92 number-wise **after denoising**, and 324.71% - 5.18 to 22.00 - **after regridding** for each step. Accordingly, the SNR_{SV} level also keeps improving - 231.83% from 21.05 to 69.85 and 251.78% from 21.05 to 74.05, respectively. Using the real component of the unwrapped image further increases both SNR parameters to 29.81 and 75.79, suggesting that the MP-PCA works best on Gaussian noise, which is in line with its theory being based on independent identically distributed noise transformed to PCA space.

These results indicate that generally, **MP Denoising is an efficient signal preserving method** that is able to efficiently reduce noise, although not completely eliminate it as that is an impossible task, as previously discussed.

7.1.2 Denoising k-space vs image-space

As discussed in section 5.2.4, when Denoising is applied, it is possible to denoise either the image directly or in k-space. Typically, using RMT, MP-PCA is performed in the image matrix directly taking voxels along the redundant dimension by identifying the MP distribution, which allows for noise to be effectively removed. However, a good algorithm performance requires for the patches used to construct the voxel dimension to have as little variation as possible. Failure to comply with this requirement may substantially reduce denoising quality.

Hence, a hypothesis was stated that using other domains may somehow improve denoising performance, namely *image-space* and *k-space*. Here, when using identical conditions for both experiments except the domain Denoising was performed, **k-space denoising** was found to be better visually - Fig. 6.9 (B) and (C) - and SNR wise - Fig. 6.7 (C) and (D). In Fig 6.10 the SNR histogram from the three cases is displayed, where k-space denoising has the highest mean and with the highest bin count, thus proving the quality enhancement. Also, signal seems to remain intact and is not erroneously removed, as evident by the uniform residuals distributions. Therefore, MP-PCA seems to mainly remove noise components in both domains - Fig. 6.8 (D) and (E) - so this simple transformation suggests huge improvements for the MP-PCA performance in this case. Most likely, this enhancement is due to the increased k-space patches similarity when compared with the sharper transitions in image domain - low and high spatial frequency proximity increase noise's covariance matrix, allowing more **pronounced principal components** and **easier noise separation**.

Lastly, k-space may be beneficial for other image processing mechanics, e.g. ghost correction might be more efficient as ghosts are more detailed and less noisy, and using k-space to completely avoid inconvenient phase wraps and ringing due to partial Fourier encoding that appears in image-space is also possible. In addition, when gridding is required - e.g. in EPI data or when other ultrafast non-cartesian k-space trajectories are used - denoising in k-space can improve performance as gridding can become more accurate for these cases.

These results have been observed in multiple datasets and were replicated in simulations - data not shown - suggesting that this denoising improvement is not a particularity of this dataset.

7.1.3 Denoising window

Seeing both plots of the SNR vs Window Size in Fig. 6.11, besides the higher SNR values for both regridding algorithm and the real component of the unwrapped image, it is also possible to observe the existence of two local SNR maximums with the increase of the denoising window, the lower one being located at the ideal denoising window expressed by [62]. This means that by incrementing the window size from 17 to 48 for a redundant dimension of 306, although it will take more time for post-processing to be concluded, an

increase of 18.1 to 21.92, 21.10% is possible to achieve, which might be worth the extra time, especially if it represents the **extra refinement when characterizing tissues**. This also seems to happen when considering the more reliable SNR_{SV}.

In addition, this might indicate that acquisitions with lower repetitions, and lower time, can be achieved as there's an extra achievable definition with smaller data sets that didn't exist beforehand.

These results have been observed with other numbered repetitions - data not shown - suggesting that these two local maximums uniqueness are not a particularity of this dataset.

7.2 Multichannel Reconstruction

7.2.1 Comparison between the vendor image and the denoised image

For the Multichannel Reconstruction, a comparison can only be done when the images have the same matrix size, thus the impossibility to compare the first two images with the vendor like what was executed in the single case. Only at the pipeline end, in Fig. 6.16, a comparison was possible. In (A) and (B), the **final image for Bruker** and the **unwrapped PR** can be seen along with their histograms. The quality improvement is not as pronounced as the single coil version, but the SNR mean improvement does still exist. Considering just the SNR mean map the enhancement is only 53.63% but when considering the more reliable SNR_{SV} the increase will be higher, 122.29%. Of note that although the unawareness of how Bruker obtained their image, further studies are necessary to understand the importance of a scaling factor and if it increases both the SNR values and the benefits of denoising.

In spite of this dilemma, these results do generally indicate **MP denoising** is an **efficient Noise removal method**, but not as effective as the single coil case.

Additionally, as demonstrated in Fig. 6.17 another image of this dataset with a higher b value has a better result with denoising, visually and number-wise, improving from 1.86 to 3.53, 89.79% and from 29.11 to 58.48, 100.89%, proving the fluctuation that SNR measurements may sometimes have, as previously discussed.

7.2.2 Denoising k-space vs image-space

When comparing the case for image-space and k-space denoising in the exact same conditions - Fig. 6.19 (A) and (B) - unlike the single coil case, **image-space denoising** was found to be better. Though Fig. 6.20 the original image (A) seems like the same as the denoised image (B) and k-space denoised (C), when inspecting the SNR map - Fig. 6.21 - a **better image is visible** as the latter two have a higher SNR level. Also, Fig. 6.22 with the histograms superposition may help to explain the closeness between images. In Fig. 6.20 (D) and (E) the residuals imply there was no signal "leakage" also suggesting this is a good signal preserving method.

Possibly there's a difference in results due to the coil combination method involving the magnitude operation to remove the coils, which may impact the original data behaviour, and because it's the multichannel case, noise correlation between coils may take part in the results discrepancy.

7.2.3 Denoising window

Finally, seeing both plots of the SNR vs Window Size in Fig. 6.23, opposite of the single channel case, Regridding decreases SNR level when considering the map mean, but does increase when the more accurate SNR_{SV} is considered.

Also, no two local maximums were found in this case, the $\sqrt{\text{No. of Repetitions}}$ is pretty accurate with the highest SNR when considering SNR map mean but is overestimated in SNR_{SV}.

This scenario might be explained by the reduction of the image size - with single coil the smallest window size is the y-dimension with 120 and in the multichannel case, the smallest is also the y-dimension with 66. The latter is almost half the former, meaning the denoising algorithm is able to improve, but might not have enough repetitions to keep escalating for the second maximum.

7.3 Limitations

Accordingly, these results do need to be generalized, using for e.g. simulations where the ground truth is known, since there are some inconsistencies with the SNR calculation after noise removal and regridding. Also, only k-space and image-space were examined in this work, implicating other useful transformations, as long as they are approximately unitary, such as wavelet and discrete cosine transformations, can have an even better performance when identifying the MP distribution and thus separating noise from signal.

8

Conclusion

This work aims to understand and develop efficient Single and Multichannel denoising strategies, in the context of fMRI, illustrating the high benefits of using a post-processing technique, MP distribution, specifically for image noise removal.

Although efficiency and absolute value increase range due to image and dataset conditions, in all performed experiments, SNR level was successfully increased, meaning overall quality boost is undeniable, visually improving the final result with more defined details and texture, which was the main goal.

Additionally, though both image and k-space domains denoising significantly improve the resultant image, the simple use of one instead of the other, namely the latter in most scenarios, is again able to further increment visual features and SNR. The mentioned k-space denoising may also be favourable to increase other image processing procedures capability, which is always a desired plus.

The study of the SNR variation with denoising window size could be an indication that there might be a better value for the window size than what's proposed in the literature. Also, the size of the image can be a key factor of how denoising performs, as a bigger image tends to have higher SNR.

Denoising appears to be more effective when single coil data is used when compared to multichannel data, however noise correlations weren't studied and may bias the results.

This way, a reliable and trustworthy method is introduced with great reproducibility which may be used not only in several medical imaging techniques but also in every subject that involves signal processing and noise and k-space acquisition, like telecommunications, image processing, data analytics, etc.

The results show that by just applying a post-processing technique, a significant increase in quality can be achieved when compared with the current scanner manufacturer's standard used by a significant number of researchers and clinicians. This opens a realm of possibilities in what can be done in the diagnostic and treatment department - and other topics of interest - as well as considering what was misdiagnosed because there wasn't a clearer image of the patient's targeted area and could have been avoided if the MP-PCA technique was in use.

Future perspectives which weren't possible to be completed include simulation of how much cleaner an image could be by introducing a commensurable amount of noise, or at the other end of the spectrum, how little could it remove, as well as denoising a 3D data set, improving the final model and how a 3D denoising window could affect/enhance MP-PCA.

Bibliography

[1] H. Jadvar and P. M. Colletti. "Competitive advantage of PET/MRI". In: *European Journal of Radiology* 83.1 (Jan. 2014), pp. 84–94. ISSN: 0720-048X. DOI: https://doi.org/10.1016/j.ejrad.2013.05.028. URL: https://www.sciencedirect.com/science/article/pii/S0720048X13002829 (cit. on p. 1).

[2] J. Pekar. "A brief introduction to functional MRI". In: *IEEE Engineering in Medicine and Biology Magazine* 25.2 (Mar. 2006), pp. 24–26. DOI: 10.1109/MEMB.2006.1607665. URL: http://ieeexplore.ieee.org/document/1607665/ (cit. on pp. 1, 2).

[3] S. Huettel, A. Song, and G. McCarthy. *Functional Magnetic Resonance Imaging*. 6th. Sinauer Associates Sunderland, MA, 2009, p. 559. ISBN: 9780878932863 (cit. on pp. 1–3, 5–16, 19, 21, 22, 25, 26, 35).

[4] R. S. of North America (RSNA) and A. C. of Radiology (ACR). *Magnetic Resonance, Functional (fMRI) - Brain*. URL: https://www.radiologyinfo.org/en/info.cfm?pg=fmribrain (visited on 01/17/2021) (cit. on p. 2).

[5] D. Levitin. *The organized mind: Thinking straight in the age of information overload*. Penguin Books, 2014. ISBN: 9780525954187 (cit. on p. 2).

[6] P. Sprawls. *Physical Principles of Medical Imaging*. Aspen Publishers Gaithersburg, 1993, p. 656. ISBN: 083420309X (cit. on p. 2).

[7] *Looking at the brain with MRI — Science Learning Hub*. URL: https://www.sciencelearn.org.nz/resources/987-looking-at-the-brain-with-mri (cit. on pp. 2, 16, 17, 20, 24, 28, 29, 39).

[8] B. Goyal, S. Agrawal, and B. Sohi. "Noise Issues Prevailing in Various Types of Medical Images". In: *Biomedical & Pharmacology Journal* 11.3 (2018), p. 1227 (cit. on pp. 3, 9).

[9] G. Burgess et al. "Evaluation of Denoising Strategies to Address Motion-Correlated Artifacts in Resting-State Functional Magnetic Resonance Imaging Data from the Human Connectome Project". In: *Brain Connectivity* 6 (9 Nov. 2016), pp. 669–680. ISSN: 21580022. DOI: 10.1089/brain.2016.0435. URL: /pmc/articles/PMC51

05353/?report=abstract%20https://www.ncbi.nlm.nih.gov/pmc/articles/PMC5105353/ (cit. on p. 3).

[10] C. Anand and J. Sahambi. "Wavelet domain non-linear filtering for MRI denoising". In: *Magnetic Resonance Imaging* 28 (6 July 2010), pp. 842–861. ISSN: 0730725X. DOI: 10.1016/j.mri.2010.03.013 (cit. on p. 3).

[11] P. Kaur, G. Singh, and P. Kaur. "A Review of Denoising Medical Images Using Machine Learning Approaches". In: *Current Medical Imaging Reviews* 14 (2018), pp. 675–685. ISSN: 1875-6603. DOI: 10.2174/1573405613666170428154156 (cit. on p. 3).

[12] Q. Wang. *Hardware of MRI System*. Apr. 2020. DOI: 10.5772/intechopen.89132. URL: www.intechopen.com (cit. on pp. 5, 12).

[13] Q. Wang et al. "Open MRI magnet with iron rings correcting the Lorentz force and field quality". In: *ieeexplore.ieee.org* 24 (3 2013). DOI: 10.1109/TASC.2013.2290587. URL: https://ieeexplore.ieee.org/abstract/document/6665128/ (cit. on p. 5).

[14] G. Gabrielse and J. Tan. "Self-shielding superconducting solenoid systems". In: *Journal of Applied Physics* 63 (10 May 1988), pp. 5143–5148. DOI: 10.1063/1.340416. URL: http://aip.scitation.org/doi/10.1063/1.340416 (cit. on p. 5).

[15] P. Callaghan. *Principles of nuclear magnetic resonance microscopy*. Oxford University, 1993. ISBN: 9780198539445 (cit. on pp. 6, 13).

[16] D. Plewes and W. Kucharczyk. "Physics of MRI: A primer". In: *Journal of Magnetic Resonance Imaging* 35 (5 May 2012), pp. 1038–1054. DOI: 10.1002/jmri.23642. URL: http://doi.wiley.com/10.1002/jmri.23642 (cit. on pp. 6, 7, 10–15).

[17] *Angular Momentum | Definition, Examples, Unit, & Facts | Britannica*. URL: https://www.britannica.com/science/angular-momentum (visited on 01/23/2021) (cit. on p. 6).

[18] *Precession | physics | Britannica*. URL: https://www.britannica.com/science/precession (visited on 01/23/2021) (cit. on p. 7).

[19] R. Henkelman, G. Stanisz, and S. Graham. "Magnetization transfer in MRI: a review". In: *NMR in Biomedicine* 14 (2 Apr. 2001), pp. 57–64. DOI: 10.1002/nbm.683. URL: http://doi.wiley.com/10.1002/nbm.683 (cit. on p. 8).

[20] J. Polzehl and K. Tabelow. *Magnetic Resonance Brain Imaging*. Springer International Publishing, 2019, pp. 5–14. ISBN: 9783030291822. DOI: 10.1007/978-3-030-29184-6. URL: http://link.springer.com/10.1007/978-3-030-29184-6 (cit. on pp. 8, 10, 11, 15).

[21] D. McRobbie et al. *MRI from picture to proton*. Cambridge University Press, Apr. 2017, pp. 1–383. ISBN: 9781107706958. DOI: 10.2214/ajr.182.3.1820592 (cit. on p. 9).

[22] Y. Gossuin et al. "Physics of magnetic resonance imaging: From spin to pixel". In: *Journal of Physics D Applied Physics* 43 (June 2010), p. 213001. DOI: 10.1088/0022-3727/43/21/213001 (cit. on pp. 10, 11, 13, 15).

[23] F. Schmitt, M. Stehling, and R. Turner. *Echo-planar imaging: theory, technique and application*. Springer Science & Business Media, 2012. ISBN: 9783642804434 (cit. on pp. 10, 16, 17, 24, 25).

[24] J. Ridgway. "Cardiovascular magnetic resonance physics for clinicians: Part I". In: *Journal of cardiovascular magnetic resonance : official journal of the Society for Cardiovascular Magnetic Resonance* 12 (Nov. 2010), p. 71. DOI: 10.1186/1532-429X-12-71 (cit. on p. 11).

[25] D. Schiffer et al. "Spatial Relationships of MR Imaging and Positron Emission Tomography with Phenotype, Genotype and Tumor Stem Cell Generation in Glioblastoma Multiforme". In: June 2014, pp. 63–93. ISBN: 978-953-51-1576-2. DOI: 10.5772/58391 (cit. on p. 14).

[26] R. N. Bracewell and R. N. Bracewell. *The Fourier transform and its applications*. McGraw-Hill New York, 1986. ISBN: 9780073039381 (cit. on p. 15).

[27] M. Bernstein, K. King, and X. Zhou. *Handbook of MRI Pulse Sequence*. Vol. 21. 2004, p. 1041. ISBN: 0120928612. DOI: 10.4314/bcse.v21i3.21211 (cit. on pp. 15, 20, 23–26, 34).

[28] H. H. Kay and C. E. Spritzer. "Magnetic Resonance Imaging in Gynecology". In: *The Global Library of Women's Medicine* (2009). DOI: 10.3843/GLOWM.10067 (cit. on p. 20).

[29] R. Bitar et al. "MR pulse sequences: What every radiologist wants to know but is afraid to ask". In: *Radiographics* 26.2 (Mar. 2006), pp. 513–537. ISSN: 15271323. DOI: 10.1148/RG.262055063 (cit. on pp. 20, 21, 24).

[30] M. Markl and J. Leupold. "Gradient echo imaging". In: *Journal of Magnetic Resonance Imaging* 35.6 (June 2012), pp. 1274–1289. ISSN: 10531807. DOI: 10.1002/jmri.23638. URL: https://onlinelibrary.wiley.com/doi/abs/10.1002/jmri.23638 (cit. on pp. 21, 23).

[31] B. A. Jung and M. Weigel. "Spin echo magnetic resonance imaging". In: *Journal of Magnetic Resonance Imaging* 37.4 (Apr. 2013), pp. 805–817. ISSN: 1522-2586. DOI: 10.1002/JMRI.24068. URL: https://onlinelibrary.wiley.com/doi/full/10.1002/jmri.24068 (cit. on pp. 21, 22).

[32] M. K. Stehling, R. Turner, and P. Mansfield. "Echo-planar imaging: Magnetic resonance imaging in a fraction of a second". In: 254.5028 (Oct. 1991), pp. 43–50. ISSN: 00368075. DOI: 10.1126/science.1925560. URL: https://science.sciencemag.org/content/254/5028/43 (cit. on pp. 22, 25).

[33] D. Calle and T. Navarro. "Basic Pulse Sequences in Magnetic Resonance Imaging". In: *Preclinical MRI: Methods and Protocols*. Ed. by M. L. García Martín and P. López Larrubia. New York, NY: Springer, 2018, pp. 21–37. ISBN: 978-1-4939-7531-0. DOI: 10.1007/978-1-4939-7531-0_2. URL: https://doi.org/10.1007/978-1-4939-7531-0_2 (cit. on p. 26).

[34] A. Pohlmeier et al. "Mri in soils: Determination of water content changes due to root water uptake by means of a multi-slice-multi-echo sequence (MSME)". In: *Open Magnetic Resonance Journal* 3.1 (2010), pp. 69–74. ISSN: 18747698. DOI: 10.2174/1874769801003010069. URL: https://www.academia.edu/download/44004934/MRI_in_Soils_Determination_of_Water_Cont20160322-2241-6f4qjr.pdf (cit. on p. 26).

[35] Bruker Corporation. *Paravision 360 - User Manual*. Version 001. Bruker. 2018. URL: https://cbbi.udel.edu/wp-content/uploads/2019/09/Bruker-Manual-Complete-.pdf (cit. on p. 26).

[36] D. Erdogmus et al. "Measuring the signal-to-noise ratio in magnetic resonance imaging: a caveat". In: *Signal Processing* 84.6 (2004), pp. 1035–1040. ISSN: 0165-1684. DOI: https://doi.org/10.1016/j.sigpro.2004.03.006. URL: https://www.sciencedirect.com/science/article/pii/S0165168404000428 (cit. on p. 27).

[37] R. M. Henkelman. "Measurement of signal intensities in the presence of noise in MR images". In: *Medical physics* 12.2 (1985), pp. 232–233. ISSN: 00942405. DOI: 10.1118/1.595711 (cit. on pp. 27, 28).

[38] E. R. Mcveigh, R. M. Henkelman, and M. J. Bronskill. "Noise and filtration in magnetic resonance imaging". In: *Medical Physics* 12.5 (1985), pp. 586–591. ISSN: 00942405. DOI: 10.1118/1.595679 (cit. on p. 27).

[39] H. Gudbjartsson and S. Patz. "The Rician distribution of noisy MRI data". In: *Magnetic Resonance in Medicine* 34.6 (6 1995), pp. 910–914. DOI: 10.1002/mrm.1910340618. URL: /pmc/articles/PMC2254141/%20/pmc/articles/PMC2254141/?report=abstract%20https://www.ncbi.nlm.nih.gov/pmc/articles/PMC2254141/ (cit. on p. 27).

[40] S. Aja-Fernández and G. Vegas-Sánchez-Ferrero. *Statistical Analysis of Noise in MRI: Modeling, Filtering and Estimation*. Springer International Publishing, Jan. 2016, pp. 1–327. ISBN: 9783319399348. DOI: 10.1007/978-3-319-39934-8. URL: http://link.springer.com/10.1007/978-3-319-39934-8 (cit. on pp. 27–29, 35).

[41] T. Miyati et al. "Novel SNR determination method in parallel MRI". In: *Medical Imaging 2006: Physics of Medical Imaging*. Ed. by M. J. Flynn and J. Hsieh. Vol. 6142. International Society for Optics and Photonics. SPIE, 2006, pp. 1244–1250. ISBN:

0819461857. DOI: 10.1117/12.653482. URL: https://doi.org/10.1117/12.653482 (cit. on p. 28).

[42] H. Hotelling. "Analysis of a complex of statistical variables into principal components". In: *Journal of Educational Psychology* 24.6 (1933), pp. 417–441. ISSN: 00220663. DOI: 10.1037/h0071325. URL: https://psycnet.apa.org/record/1934-00645-001 (cit. on pp. 29, 30).

[43] J. Veraart et al. "Denoising of diffusion MRI using random matrix theory". In: *NeuroImage* 142 (2016), pp. 394–406. ISSN: 10959572. DOI: 10.1016/j.neuroimage.2016.08.016. URL: https://www.sciencedirect.com/science/article/pii/S1053811916303949 (cit. on pp. 29, 30, 37).

[44] Q. Guo et al. "An Efficient SVD-Based Method for Image Denoising". In: *IEEE Transactions on Circuits and Systems for Video Technology* 26.5 (2016), pp. 868–880. ISSN: 10518215. DOI: 10.1109/TCSVT.2015.2416631. URL: https://ieeexplore.ieee.org/abstract/document/7067415/ (cit. on pp. 29, 30).

[45] L. Zhang et al. "Two-stage image denoising by principal component analysis with local pixel grouping". In: *Pattern Recognition* 43.4 (2010), pp. 1531–1549. ISSN: 00313203. DOI: 10.1016/j.patcog.2009.09.023. URL: https://www.sciencedirect.com/science/article/pii/S0031320309003677?casa_token=_QrRP7iolD8AAAAA:JOGRxY_LkQWooriGg-_lWDK7b8AHMcjHi72AKJp_9iCoOsg3981MASIWn0tDfVUGVhuDpF63sQ (cit. on pp. 29, 30).

[46] A. K. Jain, R. P. Duin, and J. Mao. "Statistical pattern recognition: A review". In: *IEEE Transactions on Pattern Analysis and Machine Intelligence* 22.1 (2000), pp. 4–37. ISSN: 01628828. DOI: 10.1109/34.824819. URL: https://ieeexplore.ieee.org/abstract/document/824819/?casa_token=A0YAMBb0050AAAAA:KMfmnglXtAGGA-0kELWWX-yeMW193FE3GVqyU4T0zF55ipRyI7LzT2QEJ584Ced-rQz_-Fr61Q (cit. on p. 30).

[47] Y. M. M. Babu, M. V. Subramanyam, and M. G. Prasad. "PCA based image denoising". In: *Signal & Image Processing : An International Journal* 3.2 (2012), pp. 236–244. ISSN: 22293922. DOI: 10.5121/sipij.2012.3218. URL: https://www.academia.edu/download/38396644/3212sipij18.pdf (cit. on p. 30).

[48] I. Jolliffe. "Principal Component Analysis". In: *Encyclopedia of Statistics in Behavioral Science* (Oct. 2005). DOI: 10.1002/0470013192.BSA501. URL: https://onlinelibrary.wiley.com/doi/10.1002/0470013192.bsa501 (cit. on p. 30).

[49] R. James et al. "Image Denoising Using Adaptive PCA and SVD". In: *Proceedings - 2015 5th International Conference on Advances in Computing and Communications, ICACC 2015*. IEEE. 2016, pp. 383–386. ISBN: 9781467369947. DOI: 10.1109/ICACC.2015.82. URL: https://ieeexplore.ieee.org/abstract/document/7433886/?casa_token=C5QIB6APU4MAAAAA:0Dp3FW4qWyjXIeAACMyX8FaARuJcq7eeqF6ae1Zm6HMdBzRgJ1FZHBj-dsE0LZS6aVw4j2rGcA (cit. on p. 30).

[50] D. D. Muresan and T. W. Parks. "Adaptive principal components and image denoising". In: *Proceedings 2003 International Conference on Image Processing (Cat. No. 03CH37429)*. Vol. 1. IEEE. 2003, pp. 101–104. DOI: 10.1109/icip.2003.1246908. URL: https://ieeexplore.ieee.org/abstract/document/1246908/?casa_token=m08vIVNIHYMAAAAA:fZu6FZ39ukkDEYoBaV6E-AQ1a-2VTvS3WjxWJea6xAgD-k5AgdICD49NT1uRZFy6vaZKN6B-HQ (cit. on p. 30).

[51] M. Bydder and J. Du. "Noise reduction in multiple-echo data sets using singular value decomposition". In: *Magnetic Resonance Imaging* 24.7 (2006), pp. 849–856. ISSN: 0730725X. DOI: 10.1016/j.mri.2006.03.006. URL: https://www.sciencedirect.com/science/article/pii/S0730725X06001317 (cit. on p. 30).

[52] P. Razifar et al. "Performance of Principal Component Analysis and Independent Component Analysis with Respect to Signal Extraction from Noisy Positron Emission Tomography Data - a Study on Computer Simulated Images". In: *The Open Neuroimaging Journal* 3 (2009), pp. 1–16. ISSN: 1874-4400. DOI: 10.2174/1874440000903010001. URL: https://www.ncbi.nlm.nih.gov/pmc/articles/pmc2703833/ (cit. on p. 30).

[53] J. V. Manjón, P. Coupé, and A. Buades. "MRI noise estimation and denoising using non-local PCA". In: *Medical Image Analysis* 22.1 (2015), pp. 35–47. ISSN: 13618423. DOI: 10.1016/j.media.2015.01.004. URL: https://www.sciencedirect.com/science/article/pii/S1361841515000171 (cit. on p. 31).

[54] V. A. Marčenko and L. A. Pastur. "Distribution of Eigenvalues for Some Sets of Random Matrices". In: *Mathematics of the USSR-Sbornik* 1.4 (Apr. 1967), pp. 457–483. ISSN: 0025-5734. DOI: 10.1070/sm1967v001n04abeh001994 (cit. on pp. 31, 32).

[55] J. Veraart, E. Fieremans, and D. S. Novikov. "Diffusion MRI noise mapping using random matrix theory". In: *Magnetic Resonance in Medicine* 76.5 (Nov. 2016), pp. 1582–1593. ISSN: 15222594. DOI: 10.1002/mrm.26059. URL: https://onlinelibrary.wiley.com/doi/abs/10.1002/mrm.26059?casa_token=MRgirfAwQ_EAAAAA:74DVGVj74ziw3Cip3i3wQycWrz8tSPAwFAttqdEa9hWE9rn7N_x5oV_wt_AWLftAHDNj_G4BDP07VTI (cit. on pp. 31, 32).

[56] I. M. Johnstone. "High dimensional statistical inference and random matrices". In: *International Congress of Mathematicians, ICM 2006*. Vol. 1. 2006, pp. 307–333. DOI: 10.4171/022-1/13. arXiv: 0611589 [math]. URL: https://arxiv.org/abs/math/0611589 (cit. on p. 32).

[57] R. L. Ehman and J. P. Felmlee. "Adaptive technique for high-definition MR imaging of moving structures". In: *Radiology* 173.1 (1989), pp. 255–263. DOI: 10.1148/RADIOLOGY.173.1.2781017 (cit. on p. 34).

[58] J. A. McKay et al. "Nyquist ghost correction of breast diffusion weighted imaging using referenceless methods". In: *Magnetic Resonance in Medicine* 81.4 (Apr. 2019). URL: https://onlinelibrary.wiley.com/doi/abs/10.1002/mrm.27563?casa_token=mOdXrBF0RtoAAAAA:pDTK3uXYe-2QKeDFzO23H7pjg61aOHFBFU3g0fhJNn_evx96tMkwvvop5Tjpd2iq_Oq3dPozk2TYHQY, pp. 2624–2631. ISSN: 15222594. DOI: 10.1002/mrm.27563 (cit. on p. 34).

[59] E. Yeh. "Advanced Image Reconstruction in Parallel Magnetic Resonance Imaging: Constraints and Solutions". PhD thesis. Massachusetts Institute of Technology, 2005, pp. 1–180. URL: http://en.scientificcommons.org/13104200 (cit. on p. 35).

[60] M. Bydder, D. Larkman, and J. Hajnal. "Combination of signals from array coils using image-based estimation of coil sensitivity profiles". In: *Magnetic Resonance in Medicine* 47.3 (2002), pp. 539–548. ISSN: 07403194. DOI: https://doi.org/10.1002/mrm.10092. URL: https://onlinelibrary.wiley.com/doi/abs/10.1002/mrm.10092 (cit. on p. 36).

[61] P. B. Roemer et al. "The NMR phased array". In: *Magnetic Resonance in Medicine* 16.2 (1990), pp. 192–225. ISSN: 15222594. DOI: https://doi.org/10.1002/mrm.1910160203. URL: https://onlinelibrary.wiley.com/doi/abs/10.1002/mrm.1910160203 (cit. on p. 36).

[62] M. D. Does et al. "Evaluation of principal component analysis image denoising on multi-exponential MRI relaxometry". In: *Magnetic Resonance in Medicine* 81.6 (June 2019), pp. 3503–3514. ISSN: 15222594. DOI: 10.1002/mrm.27658. URL: https://onlinelibrary.wiley.com/doi/full/10.1002/mrm.27658 (cit. on pp. 37, 56, 69, 72).

[63] R. Grimm. "Reconstruction Techniques for Dynamic Radial MRI". PhD thesis. Jan. 2015, p. 194. URL: https://opus4.kobv.de/opus4-fau/frontdoor/index/index/docId/6684 (cit. on pp. 38–40).

[64] W. N. Brouw. "Aperture Synthesis". In: *Image Processing Techniques in Astronomy*. Ed. by C. De Jager and H. Nieuwenhuijzen. Dordrecht: Springer Netherlands, 1975, pp. 301–307. ISBN: 978-94-010-1881-4 (cit. on p. 38).

[65] J. D. O'Sullivan. "A Fast Sinc Function Gridding Algorithm for Fourier Inversion in Computer Tomography". In: *IEEE Transactions on Medical Imaging* 4.4 (1985), pp. 200–207. ISSN: 02780062. DOI: 10.1109/TMI.1985.4307723. URL: https://ieeexplore.ieee.org/abstract/document/4307723/ (cit. on p. 38).

[66] H. Schomberg and J. Timmer. "The Gridding Method for Image Reconstruction by Fourier Transformation". In: *IEEE Transactions on Medical Imaging* 14.3 (1995), pp. 596–607. ISSN: 1558254X. DOI: 10.1109/42.414625. URL: https://ieeexplore.ieee.org/abstract/document/414625/ (cit. on p. 38).

[67] S. Chavez, Q.-S. Xiang, and L. An. "Understanding phase maps in MRI: a new cutline phase unwrapping method". In: *IEEE Transactions on Medical Imaging* 21.8 (2002), pp. 966–977. ISSN: 02780062. DOI: 10.1109/TMI.2002.803106. URL: https://ieeexplore.ieee.org/abstract/document/1076041/?casa_token=punC0BTJpI0AAAAA:bL4jNA0rNT0gknn0jYUKYZzvdQXpXxitFlTkRXuik8ENj7QOCM0Vrq9eJv22LzksUylUds5a7Q (cit. on p. 41).

[68] S. Witoszynskyj et al. "Phase unwrapping of MR images using ΦUN - A fast and robust region growing algorithm". In: *Medical Image Analysis* 13.2 (2009). Includes Special Section on Functional Imaging and Modelling of the Heart, pp. 257–268. ISSN: 1361-8415. DOI: https://doi.org/10.1016/j.media.2008.10.004. URL: https://www.sciencedirect.com/science/article/pii/S136184150800114X (cit. on p. 41).

[69] P. Jezzard and R. S. Balaban. "Correction for geometric distortion in echo planar images from B_0 field variations". In: *Magnetic Resonance in Medicine* 34.1 (1995), pp. 65–73. ISSN: 15222594. DOI: https://doi.org/10.1002/mrm.1910340111. eprint: https://onlinelibrary.wiley.com/doi/pdf/10.1002/mrm.1910340111. URL: https://onlinelibrary.wiley.com/doi/abs/10.1002/mrm.1910340111 (cit. on p. 41).

[70] C. Eichner et al. "Real diffusion-weighted MRI enabling true signal averaging and increased diffusion contrast". In: *NeuroImage* 122 (2015), pp. 373–384. ISSN: 1053-8119. DOI: https://doi.org/10.1016/j.neuroimage.2015.07.074. URL: https://www.sciencedirect.com/science/article/pii/S1053811915006941 (cit. on p. 41).

[71] M. Pizzolato et al. "Noise floor removal via phase correction of complex diffusion-weighted images: Influence on dti and q-space metrics". In: *Mathematics and Visualization*. Ed. by A. Fuster et al. Springer. Springer International Publishing, 2017, pp. 21–34. ISBN: 9783319541297. DOI: 10.1007/978-3-319-54130-3_2 (cit. on p. 41).

[72] P. M. Robson et al. "Comprehensive quantification of signal-to-noise ratio and g-factor for image-based and k-space-based parallel imaging reconstructions". In: *Magnetic Resonance in Medicine* 60.4 (2008), pp. 895–907. ISSN: 15222594. DOI: https://doi.org/10.1002/mrm.21728. URL: https://onlinelibrary.wiley.com/doi/abs/10.1002/mrm.21728 (cit. on p. 41).

[73] B. S. Spottiswoode et al. "3D myocardial tissue tracking with slice followed cine DENSE MRI". In: *Journal of Magnetic Resonance Imaging* 27.5 (2008), pp. 1019–1027. ISSN: 10531807. DOI: https://doi.org/10.1002/jmri.21317. URL: https://onlinelibrary.wiley.com/doi/abs/10.1002/jmri.21317 (cit. on p. 41).

[74] D. Ghiglia and M. Pritt. *Two-Dimensional Phase Unwrapping: Theory, Algorithms, and Software*. 1998, p. 512. ISBN: 9780471249351 (cit. on p. 41).

Annex 1: Abstract Submission

Marchenko-Pastur PCA denoising performance is enhanced in the k-space domain

Joao Diogo Fernandes[1], Andrada Ianus[1], Jonas L. Olesen[2,3], Rafael Neto Henriques[1], Sune N. Jespersen[2,3], Noam Shemesh[1]

[1]Champalimaud Research, Champalimaud Centre for the Unknown, Lisbon, Portugal
[2]Center for Functionally Integrative Neuroscience, Department of Clinical Medicine, Aarhus, Denmark
[3]Department of Physics and Astronomy, Aarhus University, Denmark

Synopsis (up to 100w)

Marchenko-Pastur PCA MP-PCA denoising is a prominent noise attenuation technique for MRI data with at least one redundant dimension (dMRI, T2 mapping, etc.). Typically, voxels along the redundant dimension are used to construct the matrices for denoising. However, contrast variation across the image may reduce denoising quality. Here, we hypothesized that simple data transformations to other domains may improve denoising performance. We analysed dMRI data acquired at 16.4T, denoising the data with the same window in k-space or in image space. Performance enhancements were observed for k-space denoising, suggesting that simple transformations may dramatically improve performance of MP-PCA.

Summary of main findings (250 characters, 35 words):

Simply using k-space instead of image domain signals improved Marchenko-Pastur denoising performance. Given the increasing need for improved sensitivity, this simple modification is especially effective.

ABSTRACT BODY (up to 850w, excl. ref's)

Introduction

Marchenko-Pastur PCA MP-PCA denoising[1,2] is a gaining increasing attention[3,4] for its effective noise attenuation in MRI data with at least one redundant dimension (dMRI, T2 mapping, fMRI, etc.). The benefits of MP-PCA denoising include the objectivity of the method (does not require manual rank selection) and lack of spatial (or temporal) smoothing in the reconstructed images[1].

Typically, MP-PCA operates in image domain, taking voxels along the redundant dimension and using random matrix theory to construct the MP-PCA distribution, which is then effectively removed. However, good performance requires that the contrast variation in the "patch" typically used to select the voxels across the image to be as uniform as possible. Violation of this requirement may significantly reduce denoising quality.

Here, we hypothesized that simple data transformations to other domains may improve denoising performance. When simply using identical patches in k-space or in image space, we find enhancement for k-space denoising, suggesting that simple transformations may dramatically improve performance of MP-PCA.

Methods

All animal experiments were preapproved by the competent national and international authorities and were carried out according to EU Directive 2010/63.

Sample: A mouse brain was extracted from a healthy adult mouse using standard intracardiac PFA perfusion and preserved in a PBS solution for at least 48h. The brain was then mounted in a 10 mm NMR tube filled with Fluorinert® and scanned at 37°C on a 16.4T scanner equipped with a microimaging probe capable of producing up to 1500 mT/m (isotropic).

MRI Experiments: A dMRI experiment with 20 b=0 images, and 5 b-values {1,2,5,10,20} ms/μm^2, 60 directions per b-value, Δ/δ = 10/5.5 ms were acquired using a SE-EPI sequence (TR/TE = 5000/58 ms) with BW = 400 kHz, in-plane resolution of 85 × 85 μm^2, slice thickness 0.5 mm.

Data Analysis: Pre-processing included MP-PCA denoising[1] in either k-space domain (complex data) or image domain (also complex data) after ghost correction[5]. After denoising, data was phase-unwrapped and the real part of the data was extracted[6], followed by Gibbs unringing[7]. Signal to noise was calculated voxelwise from the mean and variance along the 20 b=0 images as mean(brain_signal)/std(brain_signal).

Results and Discussion

Figure I.1 shows the data before denoising, after k-space denoising, and following the conventional image domain densoising. Note that data quality significantly improves for both denoising strategies, and the residual maps look very similar. The distribution of residuals shows very little – if any – structure, and the distribution of residuals is closely gaussian. This suggests that k-space denoising does not introduce any artifacts to the denoising process.

We then examine quantitative voxelwise signal to noise maps (**Figure I.2**) for the original, k-space denoised, and the conventional image-domain denoised data for one representative slice in the brain. The original image has a typical signal to noise of 5-15, while the k-space denoising typical signal to noise is at around 20-40. The signal to noise of the conventional image domain denoising is clearly in-between these two. **Figure I.3** further quantifies the histogram of signal to noise value in the data for the 3 conditions, clearly revealing that k-space denoising outperforms image-domain denoising in nearly all bins. Likely, the enhancement is gained due to increased similarity in k-space patches compared with the sharper transitions in image domain.

Our results have been observed in other images and were replicated in simulations (data not shown), suggesting that this denoising enhancement is not a peculiarity of the dataset provided in this abstract.

Finally, it is worth mentioning that k-space denoising may also be beneficial for other image processing procedures, for example for ghost correction performance as ghosts may be better defined and less noisy. Furthermore, inconvenient phase wraps or ringing due to partial Fourier encoding in image domain are completely avoided in k-space domain. Thus, this approach may offer significant benefits for other image processing procedures.

Conclusion

Denoising the k-space data using the MP-PCA approach provides significant enhancements in denoising performance.

This study was supported in part by "la Caixa" Foundation (ID 100010434) and European Union's Horizon 2020 research and innovation programme under the Marie Skłodowska-Curie grant agreement No 847648, fellowship code CF/BQ/PI20/11760029.

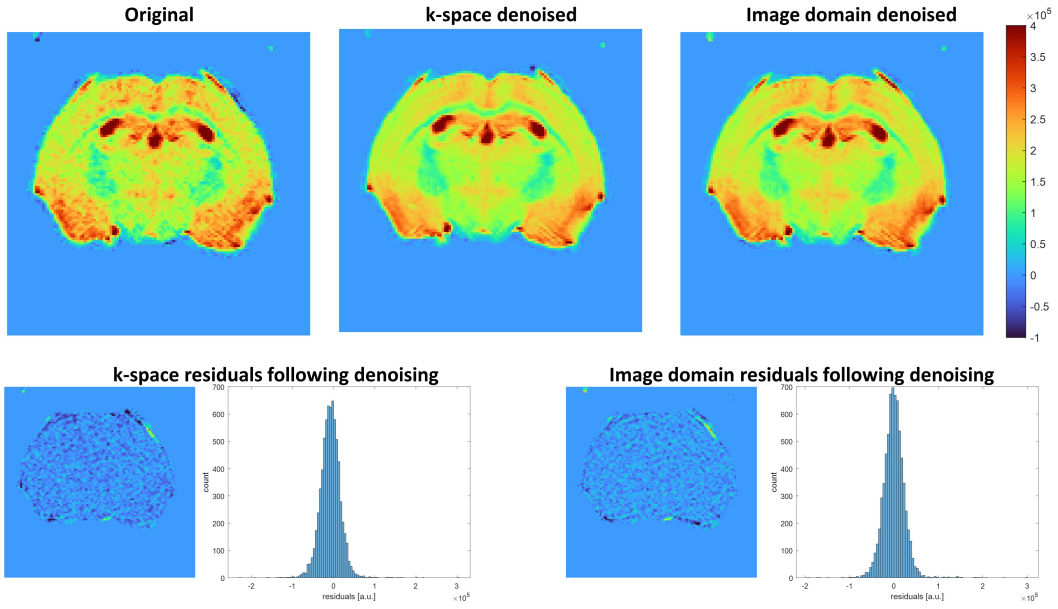

Figure I.1: Data and residuals. Original data, data denoised in the k-space domain, and data denoised more conventionally in the image domain are shown in the top row for a representative slice. The residuals are shown in the bottom row, suggesting that very little signal variance is removed. All denoising parameters were identical except the domain in which they were denoised.

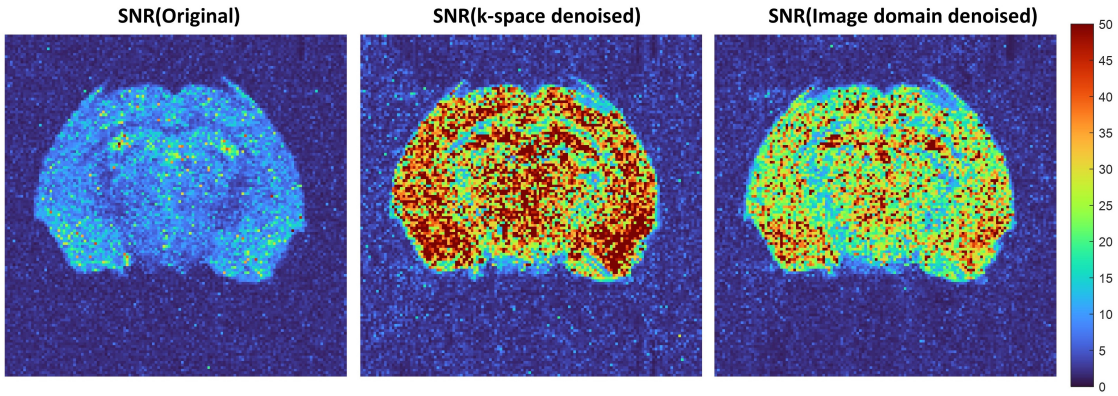

Figure I.2: Quantitative signal to noise calculation for every voxel. These SNR maps, calculated from the repetitions of 20 b=0 images, show that the overall signal to noise is much higher when data is denoised in k-space. All denoising parameters were identical except the domain in which they were denoised.

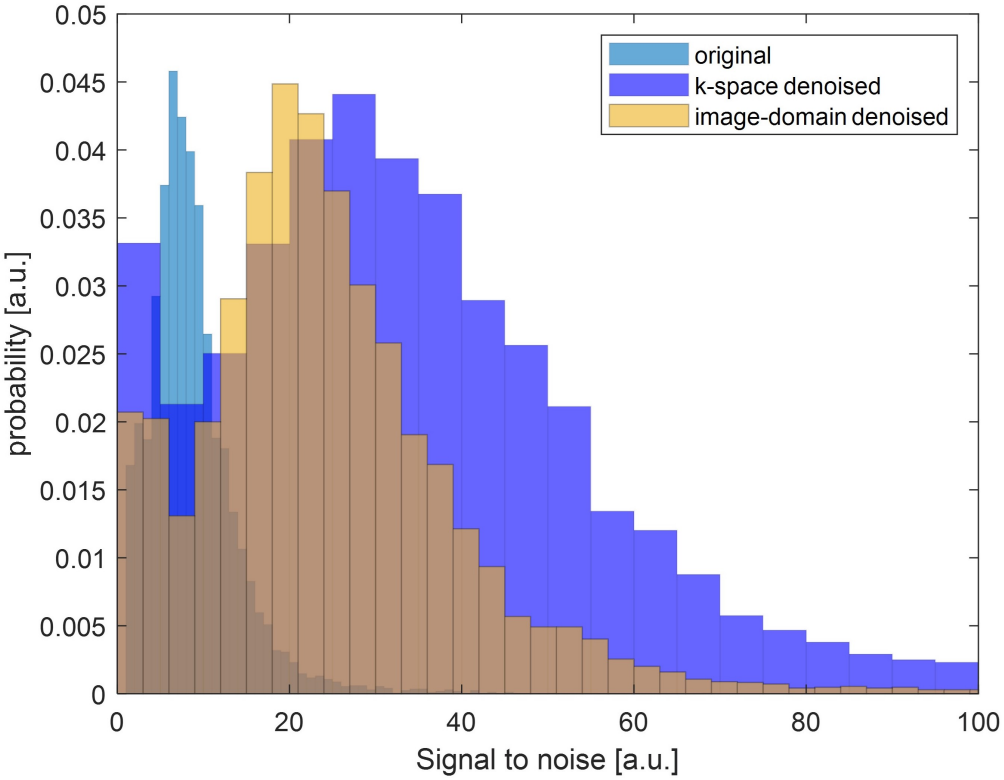

Figure I.3: Signal to noise histograms clearly reveal the improvement in k-space denoising over the conventional image based denoising. All denoising parameters were identical except the domain in which they were denoised.

Bibliography

1. Veraart, J. et al. "Denoising of diffusion MRI using random matrix theory." Neuroimage 142, 394–406 (2016).

2. Veraart, J., Fieremans, E. & Novikov, D. S. "Diffusion MRI noise mapping using random matrix theory." Magn. Reson. Med. 76, 1582–1593 (2016).

3. Does, M. D. et al. "Evaluation of principal component analysis image denoising on multi-exponential MRI relaxometry." Magn. Reson. Med. 1–12 (2019) DOI: https://doi.org/10.1002/mrm.27658.

4. Ades-Aron, B. et al. "Improved task-based functional MRI language mapping in patients with brain tumors through marchenko-pastur principal component analysis denoising." Radiology 298, 365–373 (2020).

5. Hennel, F. "Image-Based Reduction of Artifacts in Multishot Echo-Planar Imaging." J. Magn. Reson. 134, 206–213 (1998).

6. Eichner, C. et al. "Real diffusion-weighted MRI enabling true signal averaging and increased diffusion contrast." Neuroimage 122, 373–384 (2015).

7. Kellner, E., Dhital, B., Kiselev, V. G. & Reisert, M. "Gibbs-ringing artifact removal based on local subvoxel-shifts." Magn. Reson. Med. 76, 1574–1581 (2016).